ATOMIC SCALE PROPERTIES OF EPITAXIAL GRAPHENE GROWN ON SIC(0001)

A Thesis
Presented to
The Academic Faculty

by

Gregory Michael Rutter

In Partial Fulfillment
of the Requirements for the Degree
Doctor of Philosophy in the
School of Physics

Georgia Institute of Technology
December 2008

ATOMIC SCALE PROPERTIES OF EPITAXIAL GRAPHENE GROWN ON SIC(0001)

Approved by:

Dr. Phillip N. First, Advisor
School of Physics
Georgia Institute of Technology

Dr. Edward H. Conrad
School of Physics
Georgia Institute of Technology

Dr. Joseph A. Stroscio
Center for Nanoscale Science and Technology
National Institute of Standards and Technology

Dr. Zhigang Jiang
School of Physics
Georgia Institute of Technology

Dr. Mei-Yin Chou
School of Physics
Georgia Institute of Technology

Date Approved: November 11, 2008

To my wife, Natasha

ACKNOWLEDGEMENTS

Firstly, I would like to thank my Ph. D. advisor at Georgia Tech, Phillip First. Phil was a wonderful advisor in that he would always keep one intellectually honest and on his toes. It was Phil's foresight that gave me the unique opportunity to come to NIST to finish my graduate work. His understanding for interesting and exciting physics allowed me to stay at NIST for over 2 years. In these 2 years the work in this thesis could not have been possible without the help and guidance of Joseph Stroscio, my NIST sponsor. Joe was my day to day advisor during my time at NIST, and I would like to thank him for his infinite wisdom and patience. I would also like to thank my undergraduate advisor at Bradley University, Kevin Kimberlin, who always believed in me, even when I was an immature freshman. It was in his lab where I developed my passion for ultrahigh vacuum and surface science.

Special thanks are deserved for other members of the Georgia Tech physics department who have been intimately involved in the graphene project: Walter de Heer, Ed Conrad, Claire Berger, Alexei Marchenkov, Mei-Yin Chou, and Zhigang Jiang. I appreciate their guidance and assistance through the duration of my thesis work. These individuals have not only helped me, but others involved in the large graphene program at Georgia Tech. Some of these individuals are ones in which I am delighted to have as my lab mates in Phil's group, they include: Lee Miller, Kevin Kubista, Joanna Hass, Nikhil Sharma, Tianbo Li, and Sameh Dardona. Other graduate students and postdocs, outside of Phil's lab, were also influential in my graduate work, these people are: Xiaosong Wu, Mike Sprinkle, Xuebin Li, Rui Feng, Zhimin Song, and Nate Brown, I will always think highly of them for the way they have helped me through my graduate studies.

In addition, I would like to thank my colleagues at NIST: Mark Stiles, Dan Peirce, Jabez McClelland, John Unguris, Steve Blankenship, Allan Band, and Dave Rutter. Their help and guidance will never be forgotten; especially since I am continuing with work at NIST, I will probably ask for it again more than once. In addition, the other members of the STM group at NIST have always been there to guide me, they include: Young Jae Song, Sander Otte, and Young Kuk. Moreover, I would like to recognize two previous members of the STM group, who have helped me greatly; they are Jason Crain and Nathan Guisinger.

I would also like to thank my wonderful parents, grandparents and brothers for their relentless support and admiration on my long journey towards my doctorate. They have always stood alongside me, even when the thought of a Ph.D. was only a dream, and more realistically, when it seemed that I would remain forever a professional student.

Finally, and most importantly, I would like to thank my wife, Natasha, for all she has done for me in the long thesis writing process. She has helped me tremendously on my path towards Ph.D., as well as in personal life. Natasha has been a guiding light through my graduate studies, while also being my best friend and the rock of our family. She is the first person I turn to for love and support, as well as the occasional programming query. Without her, I believe that I would not have made it on this long journey through graduate school.

For all the people that I have mentioned above, and some that I have forgotten, I wish to thank you one last time from the bottom of my heart for everything that you have done for me.

TABLE OF CONTENTS

LIST OF FIGURES

LIST OF ABBREVIATIONS

Abbreviation	Meaning
2DES	two-dimensional electron system
AFM	atomic force microscopy
ARPES	angle resolved photoemission spectroscopy
BZ	Brillouin zone
CMOS	complementary metal–oxide–semiconductor
CNT	carbon nanotube
CNST	Center for Nanoscale Science and Technology
CPU	central processing unit
DFT	density-functional theory
FEM	field emission microscopy
FFT	fast Fourier transform
FIM	field ion microscopy
FTSTS	Fourier transform scanning tunneling spectroscopy
IC	integrated circuits
LDOS	local density of states
LEED	low energy electron diffraction
LHe	liquid helium
LT	low temperature
MBE	molecular beam epitaxiay
MOSFET	metal–oxide–semiconductor field-effect transistor
NIST	National Institute of Standards and Technology
PBN	pyrolytic boron nitride
QHE	quantum Hall effect
RMS	root mean square
RT	room temperature
STM	scanning tunneling microscopy
STS	scanning tunneling spectroscopy
TEM	transmission electron microscopy
UHV	ultra-high vacuum

SUMMARY

Graphene, a honeycomb lattice of sp^2-bonded carbon atoms, has received considerable attention in the scientific community due to its unique mechanical and electronic properties. Distinct symmetries of the graphene wave functions lead to unusual quantum properties, such as a unique half-integer quantum Hall effect and weak antilocalization. As an added consequence of these symmetries, back-scattering in graphene is strongly prohibited leading to long coherence lengths of carriers. These charge carriers at low energy exhibit linear energy-momentum dispersion, much like neutrinos. Thus carriers in graphene can be described as massless Dirac fermions. Graphene grown epitaxially on semiconducting substrates offers the possibility of large-scale production and deterministic patterning of graphene for nanoelectronics.

In this work, epitaxial graphene is created on silicon carbide wafers by annealing in vacuum. Sequential scanning tunneling microscopy (STM) and spectroscopy (STS) are performed in ultrahigh vacuum at a temperature of 4.2 K and 300 K. These atomic-scale studies address the growth, interfacial properties, stacking order, and quasiparticle coherence in epitaxial graphene. STM topographic images show the atomic structure of successive graphene layers on the SiC substrate, as well as the character of defects and adatoms within and below the graphene plane. STS differential conductance (dI/dV) spectra, acquired at each point in a topographic image, provide spatially and energy resolved maps of the local density of states, an important quantity for any electronic material. Such maps clearly show that scattering from atomic defects in graphene gives rise to energy-dependent standing wave patterns. We derive the carrier energy dispersion of epitaxial graphene from these data sets by quantifying the dominant wave vectors of the standing waves for each tunneling bias.

CHAPTER 1

INTRODUCTION

"Carbon has this genius of making a chemically stable two-dimensional, one-atom-thick membrane in a three-dimensional world. And that, I believe, is going to be very important in the future of chemistry and technology in general."

-Richard E. Smalley, Nobel Prize address[1]

1.1 The Big Picture

A key benchmark of the modern computer industry's performance is the empirical "Moore's law", formulated by Gordon Moore in 1965.[2] Moore predicted that the number of transistors inexpensively placed on a central processing unit (CPU), the brain of today's computers, would increase exponentially every year.[3] This trend is most readily seen in the transistor count of Intel Corporation CPUs from the last 30 years (Fig. 1.1A).[4] In essence, the accuracy of Moore's law is fueled by the miniaturization in size of transistor components. Figure 1.1B shows that the minimum feature size of transistor elements and interconnects has experienced an exponential decrease over the past 30 years.[4] However, it is widely felt that the current miniaturization cannot continue forever.[5,6] At some point the discreteness of matter itself will force a halt to Moore's law.[7]

In the near future, the small distances between transistors will result in parasitic resistances and capacitances that will be detrimental to the performance of any CPU.[8] This inevitable failure of Moore's law has prompted the semiconductor industry to investigate alternative non-silicon based materials for transistors and interconnects.[9] The limitations of modern-day semiconductor technology stem from a sole dependence of computational variables based on electron charge, which is intimately connected to the parasitic effects mentioned above.[8] Research advancements in new materials with novel quantum properties has been driving the field of nanotechnology.[10,11] Recently, inherent

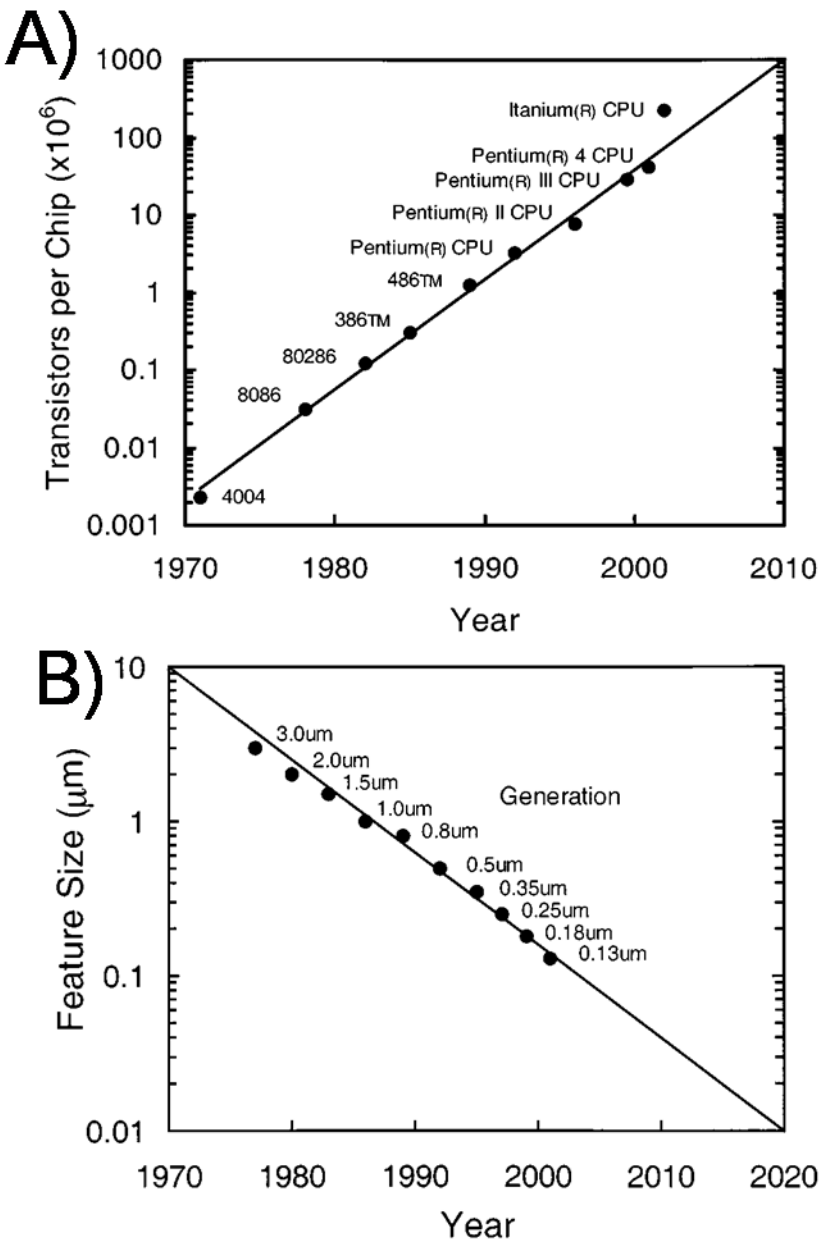

Figure 1.1

Production trends from Intel corporation with respect to the number of transistors per CPU (A) and minimum feature size of transistor components (B). These trends were predicted by Intel cofounder Gordon Moore in 1965. Moore's law, as it has been coined, has persisted for over 40 years. Many scientists and engineers agree that Moore's law will not continue forever. Therefore, alternative materials for transistors that display novel quantum properties are of increasing interest in today's research. These materials will be geared to replace the aging silicon technology. (Figure from Ref. 4)

quantum properties of electrons have been used as additional computational variables in novel scientific research. One such quantum property is the electron's spin, which has given rise to the growing field of "spintronics".[12] Another promising candidate for device applications is a material based on graphitic carbon. Graphitic carbon, such as carbon nanotubes and graphene, have similar transport properties to silicon-based devices, but also have many unique quantum properties.[13] This may prove to be advantageous for future nanoelectronic devices and allow for potential substitution of carbon for silicon in modern-day electronics.

1.2 Interest in Graphitic Systems

In current scientific research, graphitic systems amass a tremendous amount of attention.[14] At the turn of the last century, the main three graphitic systems of interest were bulk graphite, carbon fullerenes, and carbon nanotubes (but many more existed).[15] The basic building block of all these forms is a two dimensional layer of sp^2-bonded carbon atoms, commonly known as graphene (Fig. 1.2).[16] Though three dimensional in physical structure, these four graphitic materials span all the possible electronic dimensions, from the zero dimensional fullerenes to 3D graphite.[16] Although carbon fullerenes, carbon nanotubes, and graphite have been characterized for decades, the isolation and study of graphene has proved more challenging and elusive.[17] It was only in 2004 that for the first time graphene was experimentally isolated on an insulating substrate.[18] In this chapter, I will highlight some of properties of these graphitic systems. This will lay the ground work to help explain the present interest of graphene.

1.2.1 Graphite

Graphite (stacked graphene layers) is the most stable form of carbon, and creates the stiffest known material.[14] Carbon has four valence electron orbitals, 2s, $2p_x$, $2p_y$ and $2p_z$. In sp^2-bonding, the 2s, $2p_x$, and $2p_y$ form in-plane hybridized orbitals, while the

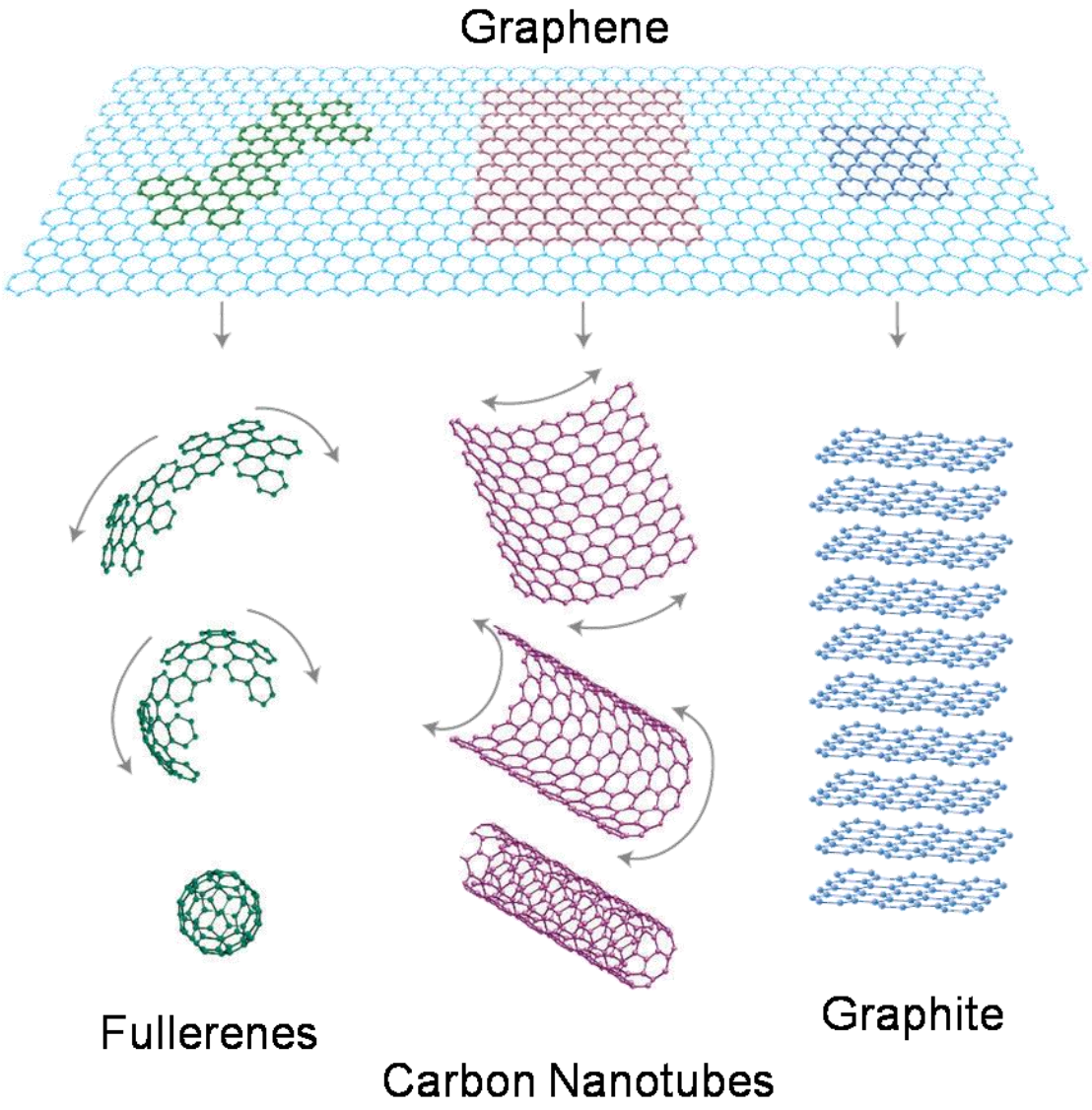

Figure 1.2
Graphene has been coined the "Mother of all Graphitic Forms".[16] Made up of a honeycomb lattice of sp^2-bonded carbon atoms, graphene forms the basic building block of many technologically interesting graphitic forms. Graphene can be rolled into a ball (fullerenes) or into a cylinder (carbon nanotubes); or graphene layers can be stacked (graphite). Electronically all these graphitic forms span the possible dimensions; fullerenes (0D), nanotubes (1D), graphene (2D), and graphite (3D). (Figure from Ref. 16)

$2p_z$ orbital points out-of plane and is not hybridized.[19] The extreme stiffness of graphite (in-plane) is related to absence of structural defects and the sp^2-hybridization of the valence electrons.[20] On the other hand, the out-of-plane coupling between carbon atoms

is considerably weaker than in-plane coupling. This manifests in graphite being a particularly effective lubricant and writing material.[21] The electronic properties of graphite are mediated by the weakly bound $2p_z$ orbital electrons, which gives rise to some of the excitement about these graphitic systems (elaborated more below).[1] These electronic properties of graphite are transferred into the low-dimensional structural configurations of graphite.[14] The most technologically relevant graphitic configurations are carbon fullerenes, carbon nanotubes, and graphene.

1.2.2 Carbon Fullerenes

A carbon fullerene (short for a buckminsterfullerene) is a caged, spheroidal molecule comprised entirely of carbon atoms.[22] The most common form of carbon fullerene is made of 60 carbon atoms (C_{60}) forming a truncated icosahedron (closely resembling a soccer ball) with 20 hexagonal faces and 12 pentagonal faces.[23] The initial production of C_{60} involved irradiating graphite with a focused pulsed laser under high-pressure helium flow.[23] To measure many of the chemical and physical properties of C_{60}, high-yield production methods were developed based on producing graphite soot from high voltage arcing of graphite rods (a process later used to discover carbon nanotubes).[24]

The structure and stability of the C_{60} was postulated well before its initial scientific discovery.[25] However, the real achievement of the experimental discovery of C_{60} was the realization that carbon self-assembles into stable clusters, such as enclosed cages and tubes.[1] Due to the scientific impact of this achievement, the 1996 Nobel prize in chemistry was awarded to the fathers of the C_{60} molecule: Smalley, Kroto, and Curl. Despite the Nobel Prize, device applications in science and industry based on fullerenes have been lacking due to difficulties in processing C_{60}.[26] However, one cousin of fullerenes, carbon nanotubes, offers a possible path for device applications based on graphitic carbon.[27]

1.2.3 Carbon Nanotubes

A carbon nanotube (CNT) is essentially a graphene sheet rolled up into a cylinder. CNT can sometimes contain one graphene sheet (single-walled CNT) or more than one graphene sheet (multiwalled CNT).[19] CNTs were initially discovered using a similar method used in the production fullerene (arcing of graphite rods).[28,29] A more common approach for making CNT involves using metal impurities (such as Ni or Co) in the fullerene growth process.[30,31] While a single sheet of graphene is characterized as a zero band gap semiconductor, the electronic properties of CNT are strongly dependent on the helicity (how the tubes are wrapped).[32-35] The helicity determines whether a CNT is metallic (no energy gap) or semiconducting (varying sizes of energy band gaps).[36,37] Each type of CNT has their own unique role for device applications.[27]

Metallic nanotubes have been regarded as exceptional quantum wires,[38] with measured current densities far larger than other metallic or superconducting wires.[39] In addition, they behave as ballistic conductors, where charge carriers experience little heat dissipation due to lack of scattering.[39,40] In contrast to metallic nanotubes, the semiconducting CNT are poor electrical wires due to non-ohmic electrical response. However, these tubes can be used as effective transistors at room temperature, similar to silicon devices in the semiconductor industry.[41,42] Connected three terminal semiconducting CNT transistors have been successfully fabricated, and have performed basic logical functions.[43,44] It has been proposed that the ultimate device would be comprised entirely of CNTs, where semiconducting CNT transistors would have metallic CNT interconnects.[45] The major problem with using CNTs for mass production circuitry involves the difficulty to accurately place a desired CNT in a specific location. This equates to making large-scale device production very difficult, if not impossible, which has stalled the use of CNTs in large scale nanoscale device applications.[46]

1.2.4 Graphene

Recently, the isolation and characterization of single sheets of graphene has opened a new door for the future carbon-based nanoelectronics.[13,47] Graphene shares many of the same novel electronic properties of CNTs. Theory shows that graphene sheets have electrical behavior (either metallic or semiconducting) that depends on how the edges of the sheet are terminated.[48,49] This property is very similar to the dependence of CNT on the helicity. It is proposed that a single graphene sheet can make a series of nanoscale devices just by lithographically cutting the edges.[16] However, this level of control over the graphene edges has not been experimentally tested.

In addition, graphene flakes produced via mechanical[50] or chemical[51] exfoliation encounter the same placement problem that has plagued CNT devices. Single graphene flakes have to be found with a Hunt-and-Peck method via an optical microscopy. In contrast, graphene grown on a substrate (epitaxial graphene) offers a viable solution for integrating graphene on wafer length scales.[52] However, many questions have been raised about the microscopic properties of epitaxial graphene. In particular, the correlation between macroscopic transport characteristics and microscopic structural and electronic properties has yet to be addressed in literature; this will be the main theme of this thesis.

1.3 Structure of this Work

In this work, scanning tunneling microscopy (STM) and scanning tunneling spectroscopy (STS) are used to investigate microscopic properties of graphene grown on SiC(0001) substrate, known as epitaxial graphene, and how these properties relate to macroscopic transport phenomena. Experimental procedures will be addressed in Chapter 2. A casual reader not interested in the experimental details of the sequential experiments performed in this work can omit this chapter for a quicker reading. For those of us not faint at heart, I start by introducing STM and STS with a brief historical

review. I describe different types of STM measurement processes and how they are performed, as well as the two STM apparatuses that I have used for this work. Finally, I discuss how we prepared our STM probe tips and graphene samples.

A detailed introduction to graphene will be given in Chapter 3. I will review some of the many pioneering works performed on the graphene system, which sparked the interest graphene has received in the scientific community. In later sections, I explain the electronic and structural properties of graphene and multilayer graphene and introduce graphene grown on a SiC substrate.

Discussion will then turn to the initial stages of graphene growth on SiC in Chapter 4. In particular, I show how graphene films grow by nucleating at step edges and forming graphene islands. In addition, I will illustrate how epitaxial graphene prefers armchair edges and follows the directions of the SiC reconstruction. I investigate the difference in the spectroscopy between the graphene terraces, graphene islands, and the SiC reconstruction. The composition of the 6H-SiC(0001)-$6\sqrt{3}$ x $6\sqrt{3}$R30° reconstruction is also discussed due to this structure's importance for the morphology and electronic properties of epitaxial graphene.

In Chapter 5, I introduce why hydrogen annealing of devices is a useful processing step in the semiconductor industry. The role hydrogen plays in passivating the dangling bonds of the 6H-SiC(0001)-$6\sqrt{3}$ x $6\sqrt{3}$R30°reconstruction is very important for our work. The reason why hydrogen does not passivate the dangling bonds between the graphene and the SiC is investigated. In addition, hydrogen adsorption on single-layer epitaxial graphene and its electronic effect on the graphene are addressed.

LTSTM characteristics of single-layer graphene, graphene/SiC interfacial region and bilayer epitaxial graphene will be discussed in Chapter 6. We have found that the first layer of graphene becomes transparent to tunneling electrons at bias voltages larger than 1 V. The interface structure is observed underneath thin graphene layers at high bias voltages and its relation to the substrate reconstruction. Following these experimental

observations, I describe electronic structure calculations that provide additional insight into the phenomena giving rise to our STM images. I will also discuss spectroscopic measurements performed on regions of graphene with interface states, in particular the large localized states observed in the spectrum over these regions. Spectra taken from regions with graphene and SiC reconstruction are then compared, and interpretations of the differences are offered.

The remaining parts of the chapter will discuss the structure and electronic properties of bilayer epitaxial graphene. In this section I show how multilayer epitaxial graphene follows the contours of the surface, in particular atomic steps separating adjoining terraces. Bias-dependent STM images of bilayer graphene are consistent with Bernal ABAB stacking, as found in the most common form of graphite. Using a simple model combining the bilayer density of states and a STM tunneling model, I calculate height differences between the two different carbon sublattices.

Chapter 7 deals with the role defects play on the electronic properties of epitaxial graphene. I describe the different types of defects that commonly appear on the surface and show how lattice defects, as opposed to interfacial defects, cause increased scattering of charge carriers in graphene. I find via high resolution differential conductance maps that the lattice defects induce electron standing wave patterns. Using Fourier transform analysis I extract an $E(\kappa)$ dispersion from the standing wave patterns for both single and bilayer epitaxial graphene. I conclude with a discussion of how the standing wave patterns are related to localization. The final chapter (Chapter 8) recapitulates the thesis with specific conclusions based on the findings from previous chapters.

CHAPTER 2

EXPERIMENTAL PROCEDURES

2.1 Introduction to STM

Since the early 1980's, scanning tunneling microscopy (STM) has been used as a powerful technique in the field of surface science.[53] STM is able to explore the electronic characteristics of atoms on surfaces with ultimate mechanical precision (on the scale of picometers).[54] In 1986, the Nobel prize in physics was awarded to the inventors of the STM (Gerd Binnig and Heinrich Rohrer), cementing its importance in the field of scientific research.[54] The invention of the STM has opened the door for many other scanning probe techniques, such as atomic force microscopy (AFM), magnetic force microscopy, and others.[55] STM is used extensively today, unearthing novel structural and electronic properties on the atomic scale.

STM works by bringing a sharp metal probe with a small radius (≈ 100 Å) close to a conducting surface (≈ 10 Å) that one wishes to characterize (Fig. 2.1).[56] When a voltage difference is applied between the tip and the sample, electrons can quantum mechanically tunnel through vacuum barrier from the STM probe tip into the sample (shown schematically as a resistor of Fig. 2.1). The tunneling process can be reversed when the polarity of the bias is inverted and electrons can tunnel from the sample into the tip. The tunneling mechanism is well covered in undergraduate textbooks on quantum mechanics and will not be discussed here.[57] A more general approach (more relevant for STM research) to vacuum tunneling from two electrodes was proposed by Bardeen.[58] Even though the STM probe tip has a large radius, the ability to image individual atoms is possible.[56] The STM tunneling current, the amount of electrons flowing across the tunneling barrier, is strongly dependent on the separation between probe tip and the surface.[59] For every 0.1 nm of distance the probe tip is away from the sample, the tunneling current decreases approximately by an order of magnitude.[59] Therefore, the

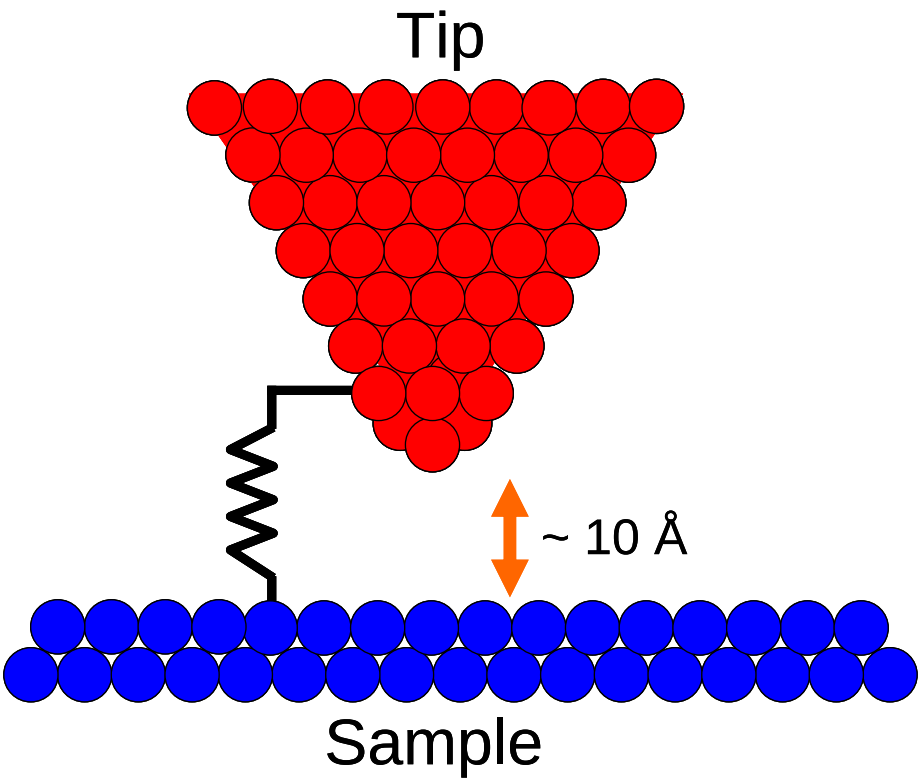

Figure 2.1

Schematic drawing of a STM probe (red circles) close to a surface (blue circles). When the probe/surface separation approaches ≈ 10 Å, electrons can quantum mechanically tunnel from the probe to the surface. This effectively forms a tunnel junction resistor in the vacuum region, where the impedance (V/I) of the junction is dependent only on the probe/surface separation. By varying the applied bias (V) or desired current (I), the impedance will change and so will the probe/surface separation. Surface topography is conducted by holding the impedance fixed and rastering the probe laterally in the plane of the surface. The measured probe height will yield information about the structural and electronic characteristics of the sample. Spectroscopy is performed by holding the probe at a particular impedance (out of feedback), then measuring the current as the voltage is ramped. Differential conductance curves, dI/dV vs. V, are obtained by lock-in detection of a small AC voltage modulation on top of the DC voltage bias. This yields spectra of the differential conductance proportional to the local density of states of the sample.

tunneling path has the highest probability to transverse through the atom at the very apex of the tip that is closest to the sample.[60] All atoms beyond the tip apex atom contribute little to the overall tunneling current. This is the reason for relatively blunt tips resolving surfaces with atomic resolution.[54]

The dependence of the tunneling current with respect to the tip/sample separation, *z*, is seen in I vs. z measurements.[61] In general, performing this measurement yields other important electronic information about a system. According to a simple quantum tunneling model, the tunneling current can be written as $I \propto \exp(-2\kappa z)$, where z is the tip/sample separation and κ is the tunneling decay constant.[56] The decay constant is strongly dependent on the average tunneling barrier height in a triangular barrier approximation.[62,63] The barrier height gives information about the relative work functions of tip and sample.[62] In addition, κ is also dependent on the parallel momentum of the electronic states.[64] To extract quantitatively the barrier height, an I vs. z measurement is performed by controllably pulling the STM probe tip away from the surface.[61] The tunneling current is measured at each incremental change of the tip/sample separation. By plotting $ln(I)$ vs. z, the slope of the curve gives κ. Measuring $I(z)$ at different tunneling biases will give a plot of values for $\kappa(V)$, which has been shown to yield important information about the system of study.[64]

Due to the large influence of the tip/sample separation on the tunneling current, most STM engineering is centered around keeping any deviation from the desired tip/sample height to a minimum.[59] To achieve this stability, many stages of vibration isolation are required in an STM experiment, as described later in this chapter. In addition to isolation systems, sophisticated electronics are utilized to constantly measure the small tunneling current (typically $\approx$ 1 nA), adjust the tip/sample separation, and perform a 3D raster of the probe tip.[65] The central part of the electronic system is known as a feedback or servo loop, which keeps the tunneling current constant. When changing tunneling conditions (i.e. impedance level), the servo loop adjusts the tip/sample distance accordingly. In addition, to the feedback loop, another part of the STM electronics allows for the rastering of the tip in the plane of sample. This rastering of the tip results

in a STM topographic image, which yields both structural and electronic information about the surface.[65]

One of the first times the STM topograph was used to extract structural information happened when the Binnig and coworkers at IBM-Zurich used it to image the complicated reconstruction of the Si(111)-7 x 7 surface (7 x 7 hereafter).[66] These STM images allowed for a unique determination of the exact atomic configuration of the 7 x 7 surface reconstruction, which was contested by many conflicting theories prior to this discovery.[67] Interpretation of the STM data gave rise to the dimer-adatom-stacking theory proposed by Takayanagi; now a well accepted theory for the atomic configuration of the 7 x 7 Si surface.[68] Since then, STM experiments have been used to complement other surface science techniques, such as diffraction and photoelectron spectroscopy.[54] In contrast to STM, these other techniques have the inherent flaw of macroscopically averaging over all the microscopic details of the sample; details that STM can sometimes clearly resolve.[69] It is this reason that STM has found its niche in the field of surface science.

2.2 Theory of STM

There are many theories describing how an STM works depending on the level of approximation. The most notable is the model by Tersoff and Hamann of Bell Labs, who came up with a theory that was both simple and applicable.[70] The researchers found that the STM tunneling current was proportional to the local density of states of the sample at the Fermi energy for tunneling at low bias. We find later that this is an over simplification, but a valid zeroth order approximation. They used their simple theory to simulate STM line traces of Binnig et al.[71] The scientists also came up with an expression for the lateral resolution Δx,

$$\Delta x = \sqrt{2\text{Å} \cdot (\text{r} + \text{d})} \qquad (2.1)$$

where r is the radius of the tip and d is the tip/sample distance.[70] Therefore, with a typical tip radius of around 100 Å and a tip/sample separation around 10 Å, $\Delta x \approx 15\,\text{Å}$. Since feature sizes around 1 Å are sometimes clearly resolved with the STM, this expression for Δx (Eq. 2.1) gives only an upper limit to the lateral resolution. As it turns out, the lateral resolution of STM exhibits a higher dependence on the atomic orbitals at the tip apex (which can be quite small) than on the overall curvature of the tip.[53]

The Tersoff -Hamann model does not take into account finite bias effects of the tunneling current on the STM images. More generally the STM current (at zero temperature) should be regarded as an integral over the local density of states of both the tip ($\rho^T[E]$) and the sample ($\rho^S[E]$) from the applied voltage bias (V) to the Fermi energy (E_F):[62,63]

$$I[E,z] = \int_{E_F}^{eV} dE \rho^S[E] \rho^T[E] \exp(-2\kappa[E]z). \qquad (2.2)$$

Now the term $\exp(-2\kappa z)$ (otherwise known as the tunneling probability) appears inside the integral of Eq. 2.2, because the decay constant κ depends on E.[62] It is clear from Eq. 2.2 that the electronic structure of the tip can contribute as much information to the tunneling current as the electronic structure of the sample. One main challenge of STM measurements is deconvoluting the contribution of the probe tip in the tunneling current. For this reason, experiments are performed with different probe tips and samples to rule out abnormalities in the STM data.

The quantity of interest in Eq. 2.2 is the density of states of the sample. Two approximations can be made to simplify Eq. 2.2. First, probe tip materials are chosen (W, Pt, Ir) that have constant density of states near the Fermi energy. Secondly, the inverse decay length κ is assumed not to have any energy dependence. Typically, the tip density of states and the tunneling probability expressions can be taken out of the integral of Eq. 2.2, which than simplifies to:

$$I[E] \propto \int_{E_F}^{eV} dE \rho^S[E] \tag{2.3}$$

where the integral now is just the sample charge density right underneath the probe tip. From Eq. 2.3 it is clear that constant current STM topographies will involve the averaging of states away from Fermi energy, proving the Tersoff-Hamann model is overly simplified.[72]

2.3 Measurement Techniques

STM incorporates many different measurement techniques. In this next section, I will discuss four of them: STM topography, spectroscopy, dI/dV mapping, and atomic manipulation.

2.3.1 Topography

One of the advantages of STM is the ability to image the surface topography. Essentially, a topography is made up of densely packed line traces from a raster of the STM probe tip.[65] The raster is performed by two piezo drives, one dedicated to the x motion and the other to the y motion, both moving with respect to the plane of the sample. The raster is conducted at slow speeds (≈ 100Å/s) to allow servo electronics on the z piezo to keep the tunneling current constant during the raster.[59] Figure 2.2A shows a STM topography of structure induced features of graphene. It is naive to assume that the STM images are only a structural map of atomic configuration.[62] More generally the STM image is a complicated mix of electronic and structural characteristics.[73,74] Figure 2.2B shows the STM image dominated by electronic effects due to scattering from defects (red arrows). Deconvoluting the structural from the electronic contributions in such topographies proves to be challenging.

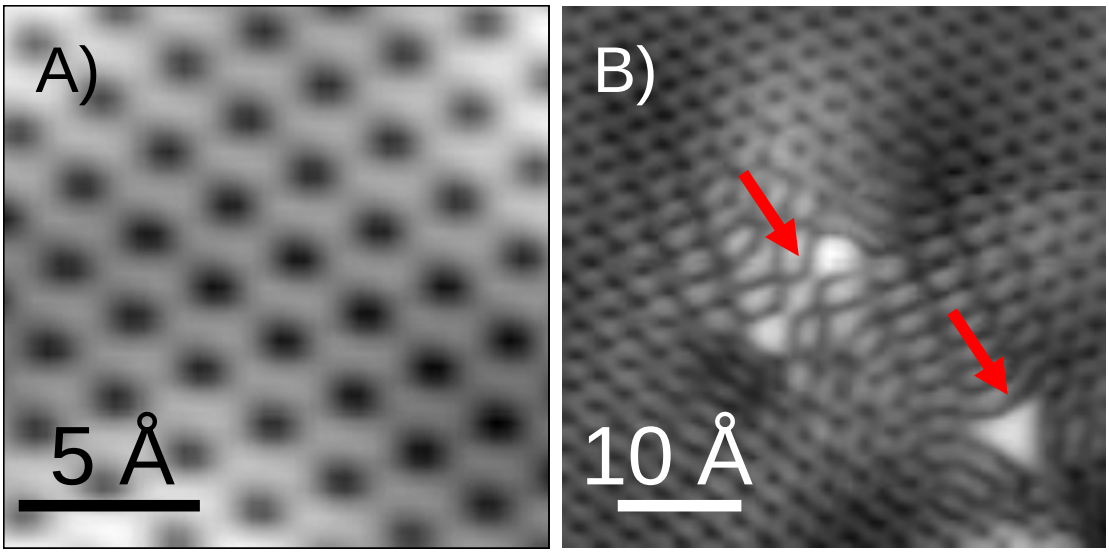

Figure 2.2

STM topographies yield both structural and electronic information about the sample. (A) STM image (15 Å x 15 Å) showing the normal and expected atomic structure of graphene. Away from abnormalities on the surface, most of the time the local charge density is centered on atoms at the surface (tunneling conditions are 0.4 V and 0.1 nA). (B) STM image (43 Å x 43 Å) showing the contributions to the topography from electronic origins (tunneling conditions are 0.3 V and 0.1 nA). Single point defects (red arrows) cause scattering (see chapter 7) which give rise to electronic disturbances in the STM topographies on the order of 20 Å.

2.3.2 Spectroscopy

To gather information about the local density of states of the sample, generally the tunneling current is differentiated. Differentiating Eq. 2.3 and setting $eV = E$ yields

$$\frac{dI}{dV}[V] \propto \rho^{S}[V]. \qquad (2.4)$$

I(V) or dI/dV measurements are commonly referred to as scanning tunneling spectroscopy (STS), but in this work STS will only mean dI/dV. Experimental measurement of the dI/dV vs. V (dI/dV hereafter) can be achieved by a simple numerical differentiation of the tunneling current with respect to voltage, I(V).[64,75] To achieve better resolution and higher signal to noise, the dI/dV is obtained via application of a

small AC voltage (modulated at high frequency) to the existing DC voltage bias, and measuring the AC current on a lock-in amplifier.[59]

Point STS is performed by positioning the STM probe tip over the area of the surface where the I(V) or dI/dV measurement is to take place. The next step involves opening the servo loop and holding the probe tip in position.[64,75] Inherent drift in the piezo drives has to be carefully taken into account as it causes the probe-tip/sample separation to change. The voltage is then ramped from one setpoint (setpoint A) to another (setpoint B), stopping at designated step increments to record the current. If an I(V) curve is desired, the STS curves can be taken very quickly (a few seconds).

To perform a dI/dV measurement (with lock-in detection), at each voltage step there are significant time delays inherent in the lock-in detection method. These delay times are strongly dependent on the time constant of the lock-in amplifier. The length of the time constant determines the amount of data averaging, with a longer time constant resulting in a better signal-to-noise ratio. Time constants are dependent on the AC voltage modulation frequency and noise conditions in the tunneling current. To average over multiple cycles of the modulation, a frequency of 500 Hz would generally require a time constant of 10 or 30 ms, depending on the strength of the signal. At each voltage increment of the dI/dV measurement, there is a delay of up to 10 time constants before data is recorded. Depending on the application, these delays can be optimized with the time of a single dI/dV measurement varying from 5 sec to 5 minutes. As a common practice, the STS measurement is limited to less than 5 minutes to prevent the probe tip from drifting. Therefore, a compromise has to be made between allowed time and a reasonable signal-to-noise ratio for a particular dI/dV measurement.

Figure 2.3 illustrates the different STM measurement techniques. Figure 2.3A shows a standard STM topography measuring 125 Å x 125 Å. The image is of 48 carbon monoxide molecules moved to form a regular square lattice array on a copper substrate with one carbon monoxide missing in the center. The carbon monoxide molecules appear

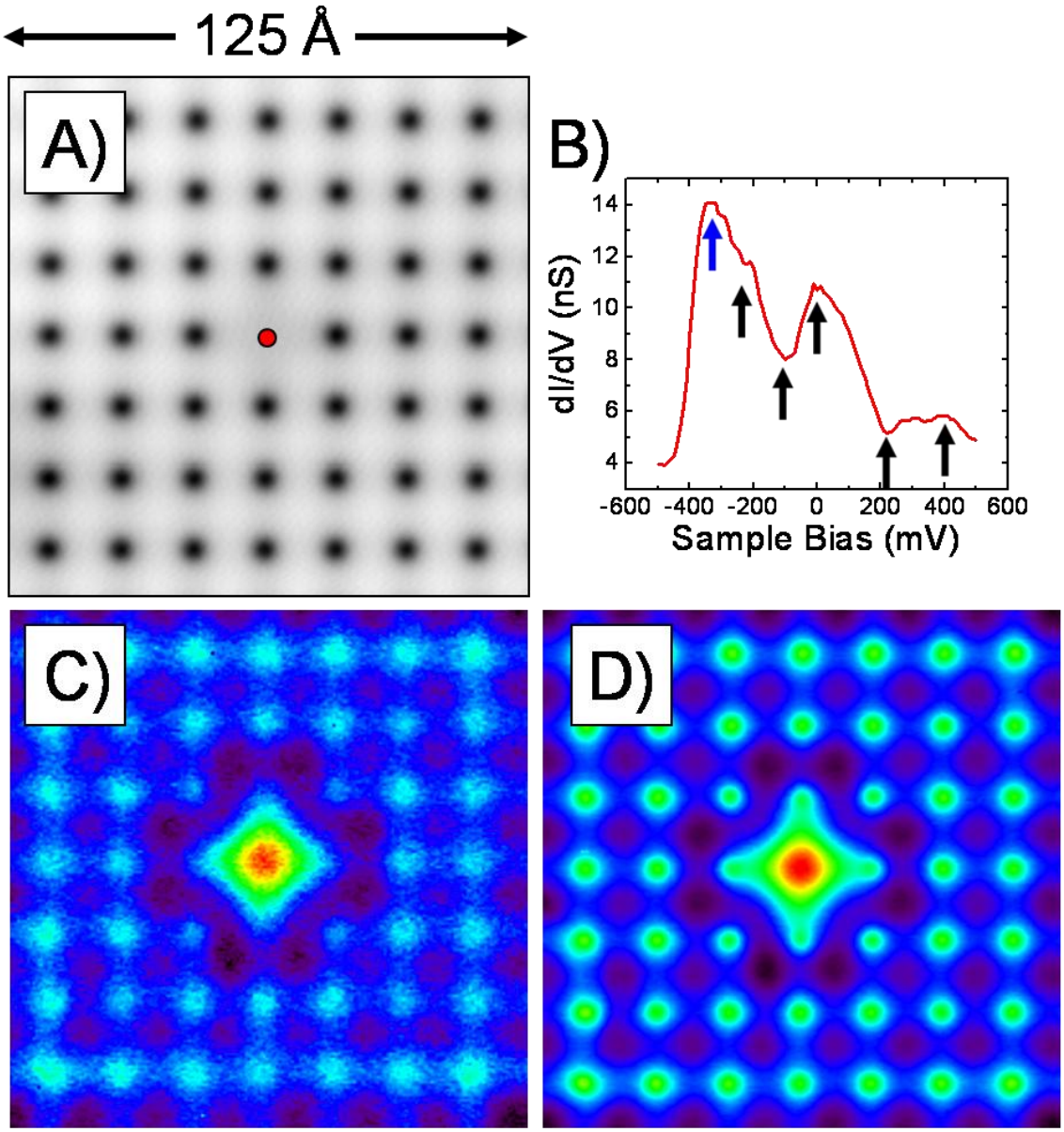

Figure 2.3

Different STM and STS measurement techniques. (A) STM topography (125 Å x 125 Å) of 48 carbon monoxide molecules manipulated by the STM to form a square grid on a Cu(111) substrate (tunneling conditions are -330 mV and 5 nA). (B) Single STS (dI/dV vs. V) performed at the center of the CO grid, labeled with a red dot in A. Tunneling conditions before STS are -0.5 V and 5 nA. (C) dI/dV map (125 Å x 125 Å) at -330 mV in open loop mode along with 5 other energies (marked by arrows in B). Lock-in amplifier time constant of the open loop map is 10 ms and was performed over 12 hrs. (D) dI/dV map (125 Å x 125 Å) at -330 mV in closed loop mode, energy labeled with blue arrow in B. The closed loop map was performed in 2 hr. This image has less noise than the open loop map of C due to the longer lock-in amplifier time constant of 30 ms and lower tunneling impedance.

dark in the topography, because they have low electron density near the Fermi energy. Therefore, the tip has to push in over a carbon monoxide to achieve the desired current.[76] In contrast, the atomic corrugation is not seen on the copper surface, because the electron density corrugation is very small.[77,78] Therefore, STM topographic images of copper only display the standing wave patterns of the electrons near Fermi energy.[77,78] Figure 2.3B shows a single dI/dV spectrum in the center of the CO grid. There is a large peak at -330 mV as well as other peaks, which arise from localized states due to scattering from the boundary conditions of the CO grid.

2.3.3 dI/dV mapping

Binnig et al. showed that two dimensional images of the dI/dV displayed features that are not evident in the STM topography.[59] The researchers imaged the surface states of Si(111)-7 x 7, with the first spatially-resolved dI/dV maps.[59] dI/dV maps are energy and spatially resolved maps of the local density of states (LDOS). In this work, I will use the terms dI/dV maps and LDOS maps interchangeably. There are two types of dI/dV maps: open servo loop and closed servo loop.[72] Open loop maps are widely used to achieve large amounts of information at many different energies.[72] A closed loop is a "quick and dirty" dI/dV map, used mainly when the time required for a full open loop map is unavailable. In my research, I found that both types of maps are complementary when used together.

Open loop dI/dV mapping involves performing a dI/dV measurement while the tip is in a hold position (open servo loop) at every point of a simultaneously acquired STM topography.[79] At every spatial point, the servo adjusts the tip/sample separation as for a normal STM topography. Next, the tip is put into a hold position, and the voltage is ramped while the I(V) and dI/dV(V) are recorded. Before moving to the next spatial point, the tip is taken out of the hold position, and the servo once again adjusts the

tip/sample separation. The open servo loop dI/dV map is very informative and it gives an accurate picture of the LDOS in two dimensions.[62]

There is one drawback to open loop dI/dV maps. The maps usually take a very long time to complete. It is tempting to take a large area map with high spatial resolution and each dI/dV curve having high energy resolution. More than likely this kind of desired map would take longer than the time capabilities of a typical instrument (for the NIST-LTSTM the time is limited to < 80 hr due to helium cryostat refills). Therefore, compromises have to be made both in spatial and energy resolution. However, the open loop mapping at a single energy is an excellent choice if one has the time (overnight or over a weekend) to take a scan or if one is trying to gather information about the system.

Figure 2.3C shows LDOS map at -330 mV (indicated by the blue arrow in Fig. 2.3B) from an open loop dI/dV data set. There were 5 other maps extracted at the same time, with energies marked by the black arrows of Fig. 2.3B. This set of data was performed over a 12 hr period. As one can see, at the vacancy site in the center of the CO grid there is a central maximum indicating large density of states (Fig. 2.3C). It is interesting to note that this large maximum is absent from the STM topography (Fig. 2.3A).

The closed loop dI/dV map is a quick alternative to a long open loop dI/dV map, but results in a map at only one energy value. This type of map involves performing a STM topography with an AC voltage modulation turned on for the entire time of the scan.[59] As the tip is rastered across the surface, a dI/dV signal is recorded (via lock-in amplifier) at the STM topography voltage bias setpoint. At every spatial point the servo is continuously measuring and adjusting the tip/sample separation. Therefore, the tip is never in a hold position and the voltage is not ramped, which is very different than the open loop dI/dV map. Therefore, this type of map can suffer from topographic feedthrough effects due to the very dI/dV signal one is trying to measure. However, this type of map can also be informative; the map is only performed at the energy of the

sample bias of the STM topography and, therefore, the spatial resolution and area in a closed loop map can be quite large.

Figure 2.3D shows a closed loop dI/dV map taken at the same energy and area as Fig. 2.3C. Despite showing the same features, the noise level of the closed loop map is quite lower than the open loop map at the same energy due to the longer time constant and higher signal from lower tunneling impedance. There are still time delays associated with the closed loop dI/dV map. A delay of a certain number of time constants is required, because the dI/dV signal is still being measured with the lock-in amplifier. The closed loop map of Fig. 2.3D was performed in 2 hours. There is one drawback to a closed loop dI/dV map, this being that the map can display some unwanted topographic features, since the servo loop is always closed at the setpoint of the topographic image.[72]

In addition to looking for individual features in a dI/dV map, Fourier transform analysis can yield information about periodic structures that maybe hidden or not obvious in the map.[80-82] By breaking the dI/dV map down into its Fourier components and displaying them as a two dimensional picture, one can extract the different periodicities in a particular dI/dV map. These periodicities can arise from many sources; one of interest is elastic scattering. From the power spectrum the scattering wave vectors can be extracted. Combining with the fact that the dI/dV map is energy resolved, the scattering wave vectors from a series of dI/dV maps can be plotted versus energy, which will result in an $E(\kappa)$ dispersion, or the electronic band structure. Therefore, STS mapping can give a unique determination of the band structure on the nanometer scale. Chapter 7 will explain in detail the use of Fourier transform analysis with regard to dI/dV maps of graphene, to determine an E(**k**) dispersion.

2.3.4 Atomic Manipulation

All the processes that I have described so far use STM as a characterization technique. However, the STM can be used to make nanoscale structures via moving

atoms or molecules into exact atom configurations.[83] Essentially, this is the ultimate bottom-up fabrication method. Atomic manipulation was pioneered at the IBM-Almaden laboratory, where it was shown that an STM tip can form a trapping potential for surface adatoms when the tunneling impedance is lowered.[84] As the tip is moved across the surface the adatom follows the trapping potential. When the adatom is in its final location, the tunneling impedance is raised allowing for the adatom to be released from the potential.[84] This process needs to be conducted at low temperatures, where the atoms on the surface have low surface mobility. The CO grid of Fig. 2.3A was made using atom manipulation techniques described in this section.

2.4 Description of STM Apparatuses

STM measurements can be conducted at a wide range of temperatures from 20 mK to 300 K and higher.[85] In my work, I will focus on two of these temperatures: 4.2 K and 300 K. There are clear advantages and disadvantages in operating at either of these temperatures. One particular advantage of low temperature STM and STS measurements is seen in the experimental broadening of dI/dV features due to the thermal smearing of the tip and sample density of states. The energy resolution in STS measurements taking into account thermal and experimental broadening is given by:

$$\Delta E = \sqrt{(3.3 \cdot k_B \cdot T)^2 + (2.5 \cdot V_{\text{mod}})^2} \tag{2.5}$$

where T is temperature, k_B is the Boltzmann constant and V_{mod} is the root mean square (RMS) of the AC modulation voltage.[86] From Eq. 2.5 it is clear that the temperature broadening ($V_{\text{mod}} = 0$) is considerably smaller at 4.2 K ($\Delta E = 1.2\ meV$) than at 300 K ($\Delta E = 85\ meV$). In addition, at low temperature the drift from the piezo electric actuators is significantly lower than at room temperature. Another advantage is that at

low temperature the sample stays free of containments for a longer period of time due to the enhanced cryopumping of the cryogenic environment. The key disadvantage of low temperature is that samples and tips cannot be exchanged as easily and frequently as room temperature measurement systems. For a room temperature STM (RTSTM) system multiple samples and tips can be studied in one day. RTSTM systems are generally smaller, less expensive, and do not require periodic filling of cryogenic liquids.

To utilize the advantages of both temperature ranges, my thesis will incorporate data from two different microscopes. The instrument in which a majority of my thesis work was performed on was the 4.2 K STM (LTSTM) located in the Center for Nanoscale Science and Technology (CNST) at the National Institute of Standards and Technology (NIST) in Gaithersburg, MD. Some of the other STM measurements were performed in a room temperature microscope also at NIST. In the rest of this section, I will give a brief introduction to the LTSTM and RTSTM at NIST.

The LTSTM system at NIST is made up of seven independent ultrahigh vacuum (UHV) chambers. Each individual chamber can be valved off from the other chambers and UHV can be maintained by individual pumping. This allows for the ability to vent each chamber independently to fix problems and install upgrades. The seven chambers (shown in Fig. 2.4) are made up of two molecular beam epitaxiay (MBE) growth chambers, a load lock chamber, sample and tip storage chamber, a field ion microscopy (FIM) chamber, a rotary transfer chamber, and a STM chamber. The system has a 100 liter helium (LHe) cryostat, equipped with two superconducting magnets: one is a 10 T vertical solenoid magnet (parallel to sample normal) and the other is a 1.5 T split pair solenoid magnet (perpendicular to sample normal). The combined magnets can rotate a field of 1.5 T in a 2D plane

To perform STM measurements with sub-picometer stability, there needs to be put in place many different overlapping layers of vibration isolation, which will decouple harmful fluctuations of the environment. In the LTSTM described above, the zeroth

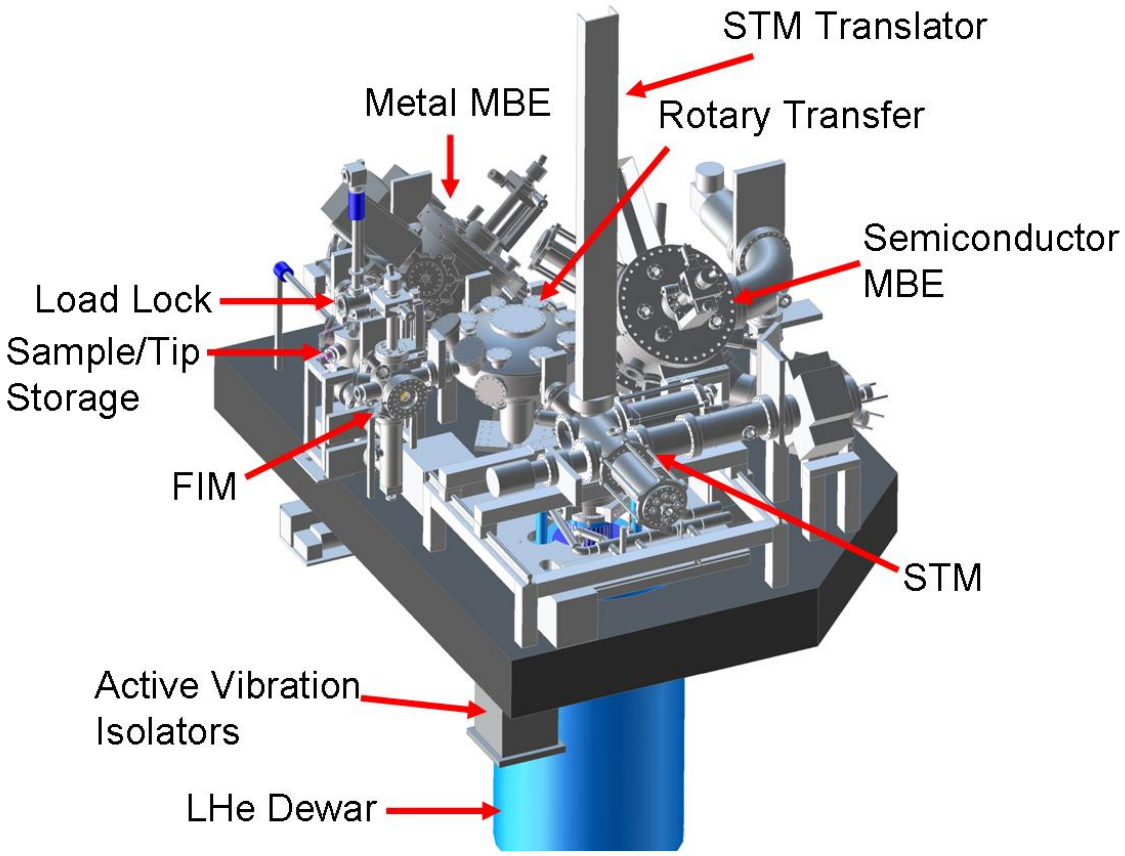

Figure 2.4

3D-computer-aided drawing of the NIST-LTSTM apparatus. The drawing illustrates all the large external components of the LTSTM system, including the UHV chambers, the active vibration system, and the liquid He Dewar. All of the different components are described in detail in the text.

order stage of isolation is enclosing the system with an acoustic enclosure, which damps out acoustic sound waves. The enclosure also shields the STM from outside radio frequency noise. All the controls for the STM originate from outside the shielded enclosure in an external control room.

The large enclosure only shields noise sources in the air, but offers little protection from vibrations that originate from the floor. To damp these floor vibrations, we stack three different stages of isolation. The first stage is an active vibration isolation stage that holds the table above the floor (Fig. 2.4). Each leg of the table (three total) has a piezo driven mechanism and a 3 axes geophone system that simultaneously measures

and cancels the floor vibrations. The second stage involves isolating the helium cryostat from any extra unwanted vibration. The actual cryostat is lifted off the table with passive damping air legs. The third stage of vibration isolation involves similar air legs on the UHV insert, which fits inside the He cryostat. The air springs on the UHV insert have individual RC damping elements made using needle valves and expansion tanks. These can be tuned to reduce the positive gain at resonance yielding a critically damped isolator.

Next, I will discuss the details of the STM module. A cross sectional picture of the STM module is shown in Fig. 2.5. The entire STM module is translated from the top of the STM chamber all the way down into the LHe cryostat for operation. When the module is positioned in the top part of the STM chamber, samples and probe tips can be introduced into the STM module. In the STM module we apply the tunneling voltage from the sample to the tip. The tunneling current is measured from the tip lead. The sample sits on a special stage with its normal pointing up. Underneath the sample are two piezo tube scanners: one for the x-y motion and one for the z-motion. The x-y scanner is used for the STM topography raster and the z-piezo acts as the mechanism to servo the tip-sample separation. The relative height of the z-piezo during a measurement is seen as the height variations in the STM topography. Coarse motion of the sample is performed by Z-piezo walker, which works in a stick-slip motion.[87]

The tip is positioned in a separate 2D stage that is above the sample, with the tip apex is pointing down. Since during an STM topography the tip is held fixed, there are no capabilities of any fine control of the tip position. However, there are two independent coarse motions that can move the tip in-plane. The tip stage has isolated X- and Y-piezo walkers, very similar to what was described for the Z-piezo walker on the sample stage. The tip coarse positioning system can move the tip ± 3 mm in-plane on a square. We use the coarse positioning of the tip in two ways: first, for overall lateral alignment of the tip/sample, and second for moving the tip off the sample for

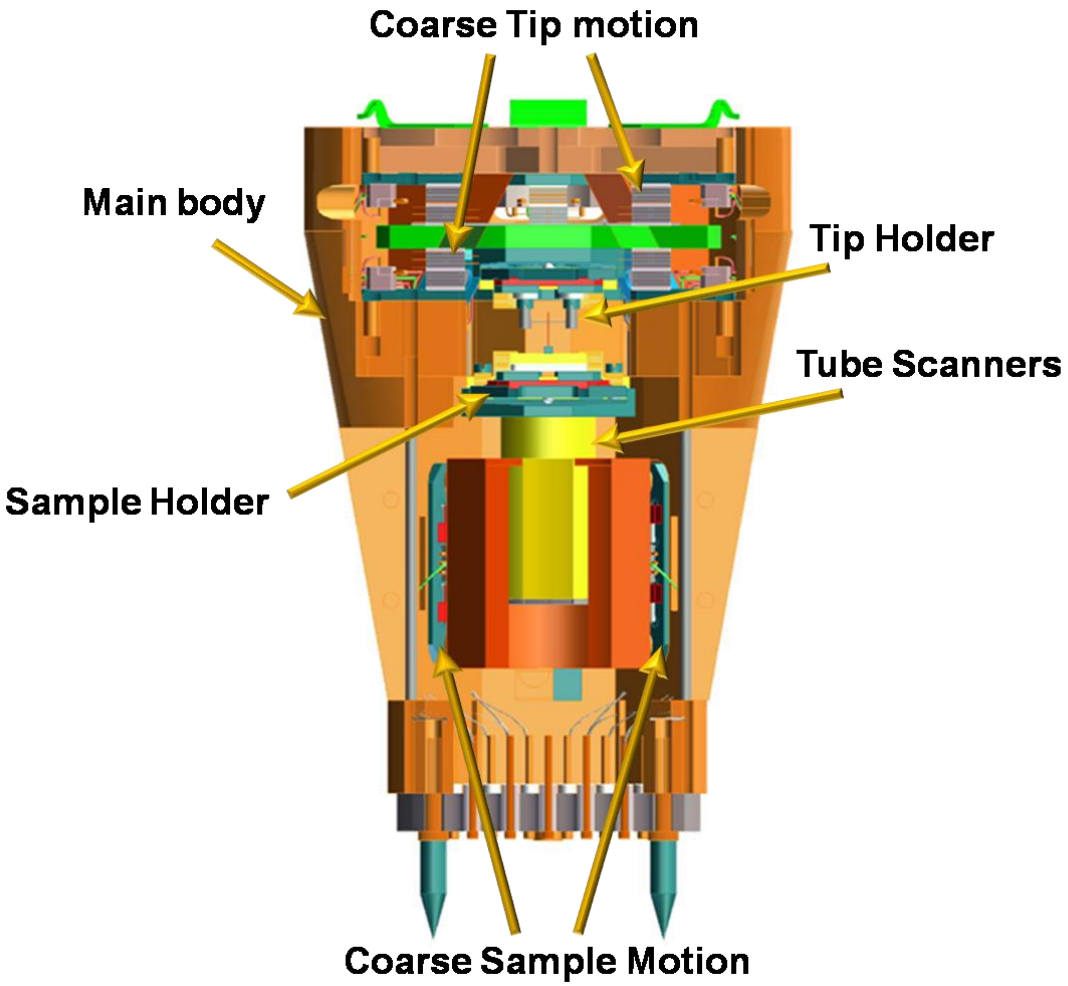

Figure 2.5

3D-computer-aided cross sectional view of the LTSTM module. The entire module can be lifted (via the STM translator) from a LHe environment to a room temperature environment. Inside module is housed the tip and sample stage, which allows for full operation of the STM in the LHe cryostat. Electrical contact is made in the cryostat by Cu spring loaded pins at the bottom of the module. All of the different components of the module are described in detail in the text.

metal/molecule deposition onto the cooled sample. The tip holder has a hole through the base to allow for evaporation of metals/molecules onto the sample surface from the upper part of the STM vacuum system.

The RTSTM system at NIST has been described elsewhere,[88] a similar system is located in the physics department of the Georgia Institute of Technology. However, I will give a brief description of the RTSTM in this section. The STM and sample

preparation techniques are located in the same UHV chamber. The system is equipped with a load lock chamber for fast entry of samples and tips. The STM stage is designed with a double spring vibration isolation system along with eddy current damping. Coarse positioning of the sample is conducted by two inchworm piezo electric drives (both on the sample stage). A high powered telescope is utilized to observe the tip/sample separation, while manually coarse positioning the sample using the inchworms. Using this optical setup, the separation can be as close as 10 μm. To get the sample into tunneling range, the rest of the coarse approach is performed by a computer. Using this method of a fast coarse approach allows for high throughput of samples and tips. During STM operation, the sample is held fixed and the tip is rastered via a XYZ scanner. In addition, the tunneling current now is measured on the sample electrode.

2.5 Tip preparation

One of the main challenges of STM is making reliable probe tips. In this section, I will describe the procedure of electrochemical polishing probe tips. We make our tips out of 0.01" iridium (Ir) wire. Before introducing the tip into UHV, we perform an electrochemical etch to sharpen the tip to a radius of 100 Å. When the tip is in UHV, cleaning of the tip is performed to get the probe tip ready for a STM measurement. The cleaning involves outgassing the tip at elevated temperatures and performing field evaporation using field ion microscopy (FIM).

Before we introduce the tips into UHV, we electrochemically etch the Ir to a microscopically fine point. The first step, called a coarse etch, involves shaping the apex of the tip into a conical point. This coarse etch is conducted by dipping the STM probe in and out of the etching solution with a large bias ($\approx 35\ V_{RMS}$) applied to it. The bias is applied to the solution through a graphite rod that is placed into the solution. The etching solution is made from anhydrous CaCl salt dissolved in deionized water, until it saturates the water. This saturated solution is then diluted once more for the final solution with

proportions: 1/3 of the saturated solution and 2/3 deionized water. The coarse etching only takes about 5 to 10 minutes. After the coarse etch, we perform a much finer etching or polishing under a high power optical microscope. This time the electrical connection is made via a small platinum loop that has been dipped in the etching solution. The solution on the loop will form a film that will serve as our etching mechanism. The tip is held fixed in the microscope and the position of the loop can be changed via a fine translation stage. A smaller AC voltage ($\approx 5\ V_{RMS}$) is applied between the loop and the tip as the loop is rastered back and forth on the tip apex. Eventually the tip apex will become polished to a point that cannot be seen with the microscope. After this step the tip is cleaned with solvents and deionized water to remove the etching solution, and can be introduced in UHV.

The first stage in the UHV cleaning of an STM probe tip is to outgas the probe via high voltage electron bombardment. This involves bringing the STM tip close (1/4") to a hot tungsten (W) filament with ≈ 5 amps running through it. By applying a large voltage (≈ 1200 V) between the filament and tip, high energy electrons passing through the W filament emit straight to the apex of the tip. We can monitor the cleaning process by measuring the emission current of these electrons. We try to keep the emission current at around 2 mA, since larger values of emission current will result in a duller tip. Annealing of this type causes considerable outgassing of the tip, and requires a large turbomolecular pump to keep the pressure in the chamber from degrading.

After outgassing, we position the tip in front of a channel plate/phosphor screen flange to perform field emission microscopy (FEM) and field ion microscopy. Firstly, FEM is used to achieve proper tip alignment in front of the screen, and also to estimate the tip's radius. FEM involves applying a negative bias (around 0.1 to 1 kV) to the tip. Electrons from the tip are accelerated from the apex and focused via a channel plate toward the imaging screen. When the electrons hit the phosphor screen, it illuminates showing an image of where the electrons originated. By noting the voltage threshold of

the FEM pattern, an estimate of the radius of the tip can be obtained. The low voltages of the FEM process does not allow for any cleaning of the tip. Therefore, we only use FEM for a measure of the tip radius and alignment for the final cleaning step.

As a final step of cleaning, we perform field evaporation by using field ion microscopy on the tip. Firstly, the entire chamber is back filled with helium gas to the pressure of 3×10^{-5} Torr. Next, we apply a very large positive bias (1-10 kV) to the tip. The helium atoms near the tip apex are ionized by the large voltage, and repelled from the tip. The ions generate an electron cascade in the channel plates and then are imaged on the phosphor screen. Containments and the outer layers of the tip are evaporated as the voltage is increased, which can be observed on the screen in real time. We use the FIM image as an indicator of how sharp, clean, and well ordered the STM probe tip is. The tip preparation procedure is similar for both the RTSTM and the LTSTM at NIST. The only difference is that the field evaporation procedure in the RTSTM is not conducted with a helium imaging gas.

2.6 Sample Preparation

The sample preparation of the epitaxial graphene on SiC(0001) will now be explained in detail. The starting SiC wafers were purchased from Cree Inc. and diced into small pieces. Before graphitization, samples were etched for 30 min under a flow of molecular hydrogen near atmospheric pressure at a temperature of 1550 ˚C. This process has been shown to remove polishing scratches that appear as nanometer deep gouges in atomic force microscopy (AFM) images.[89] The etching leaves an ordered SiC step array, with terraces for nominally on-axis SiC samples typically 0.4 μm in size and separated by 1 nm steps (the height of a 4H-SiC unit cell).[89] Terrace size is determined by the miscut angle of the wafer. It is clear the etching increases the initial quality of the SiC substrate substantially for the graphene growth with regard to domain size[90] and defect concentration.[91]

For LTSTM studies the epitaxial graphene was grown on the silicon-terminated face of 4H-SiC(0001) in a graphitization process involving the thermal desorption of silicon at high annealing temperatures. After hydrogen etching, samples (3 mm x 4 mm). were graphitized by annealing to above 1200 ˚C in UHV using electron bombardment heating in a procedure described elsewhere.[92] The base pressure of the system was 1 x 10^{-10} Torr with a maximum pressure of 3.5 x 10^{-8} Torr during graphitization. The thickness of the graphene films was determined by analyzing the ratio of silicon to carbon intensities obtained from in-situ Auger electron spectroscopy measurements.[52] The overall quality of the epitaxial graphene was evaluated in-situ by low energy electron diffraction (LEED). Epitaxial graphene samples were grown at the Georgia Institute of Technology and then transferred to the NIST for low-temperature STM measurements.

After introduction into the LTSTM system at NIST, samples were annealed at 800 ˚C for 5 min, monitored with an optical pyrometer. The base pressure of the system was 1 x 10^{-10} Torr and 1 x 10^{-9} Torr during annealing. Sample heating is achieved through a small pyrolytic boron nitride (PBN) heater directly beneath the sample. Essentially, the heater is a ceramic-isolated filament that is touching the graphene sample through a metal support. By passing a current through the filament, the heater will raise the temperature of the sample though direct heat conduction. PBN heaters are an accurate and effective way to anneal a sample in UHV.

Before the start of the experiment, graphene samples and iridium probe tips were loaded into the cryogenic STM system, described earlier in this chapter. STM measurements were performed at constant tunneling currents after cooling to 4.2 K. Differential conductance, dI/dV, was measured with a lock-in amplifier, using a small voltage modulation, typically 0.4 mV_{RMS} to 1 mV_{RMS}, at a frequency of ≈ 500 Hz.

In chapters 4 and 5, I will show results from a low coverage in-situ grown epitaxial graphene sample (3.3 mm x 8.7 mm) studied by RTSTM. The sample was highly doped to allow heating via direct current flow. The sample holder is made of

molybdenum (Mo), which is sliced in two pieces to allow for direct heating. Two Mo pieces are held together with a Mo screw with electrical isolation via alumina washers. The sample was fixed with Mo clips (0.005" thick foil) that pinch the sample edges. The clips are spot welded to each side of the holder base. After introduction of the holder into the RTSTM, the sample was annealed for 12 hours at 600 ºC under UHV conditions. The temperature was measured by an optical pyrometer, accurately calibrated to the melting temperature of Au. This initial outgas is necessary to remove any hydrocarbons and contamination from the sample and its holder.

To achieve a very small coverage of graphene, we annealed the sample to 1200 ºC very quickly (≈ 30 sec ramp) and held it at this temperature for 30 sec. This temperature has been shown to be on the cusp of graphene formation in LEED patterns.[89,93] During annealing, the pressure in the chamber increased from its base pressure of 1×10^{-11} Torr to 1×10^{-8} Torr. This process was repeated five times to induce more growth on the surface. Before STM operation, graphene samples and iridium probe tips were loaded into the RTSTM system. STM measurements were performed at constant tunneling currents at 300 K. Differential conductance, dI/dV, was measured with a lock-in amplifier, using a voltage modulation, typically 20 mV_{RMS}, at a frequency of ≈ 1.4 kHz.

CHAPTER 3

GRAPHENE: A NEW MATERIAL FOR NANOELECTRONICS

3.1 Introduction

The study of graphene is a significant step towards a future with carbon-based nanoelectronics. However, many experimental graphene studies are still in their infancy, due to the many challenges in graphene synthesis. Therefore, electronic integration of graphene will have to take hold of what was learned in the characterization of carbon nanotubes and other graphitic forms, introduced in Chapter 1. This chapter will expand upon what was discussed in Chapter 1, where graphene was only briefly introduced. In the sequential sections, I will give a general review of graphene from both a historical and technological point of view. In addition, I will spend a considerable amount of time deriving the electronic structure of both single-layer and bilayer graphene. These derivations will be the ground work for the rest of this thesis, which I attempt to elucidate atomic scale electronic properties of graphene.

3.1.1 Historical Review

Since the early part of last century, it was widely accepted that free-standing perfect 2D structures like graphene were both chemically and physically unstable.[94-96] This idea was put into question when single sheets of graphene were successfully isolated from bulk graphite.[50,97] In 2005, the isolation and electrical transport of graphene was performed independently by two groups; one at the University of Manchester,[18,98] and the other at Columbia University.[99] The exfoliation technique these groups used to isolate graphene is now well known and has been described in detail elsewhere.[18] To summarize, what the researchers did was use common adhesive tape, found at any office supply store, to peel off the top layers of a bulk graphite crystal. Although a crude technique of crystal growth, the peeling of graphite to produce graphene is truly on art

form that takes many hours of practice (a perfect job for a graduate student). The quality and size of the graphene flakes is dependent on the type of starting graphite: whether the starting material is natural graphite, highly ordered pyrolytic graphite (HOPG), or Kish graphite. In addition, the type of adhesive type is also a contributing factor in the quality of the graphene. It appears that from my colleague's experience the best quality of graphene flakes are produced with high-purity HOPG or natural graphite peeled with Nupro brand adhesive tape.

After exfoliation from the bulk graphite crystal, the tape is rubbed against a degenerately doped Si wafer with a 300 nm SiO_2 overlayer. The SiO_2 serves as a gate dielectric between the Si substrate and graphene. The 300 nm oxide thickness is extremely important, since it allows for the locating of graphene flakes with optical microscopy due to optical interference from the underlying silicon wafer and graphene layers.[18] The rubbing of the tape onto the SiO_2 results in a random assortment of graphitic flakes of various thicknesses plus tape residue, and other objects of unknown origin. Hunting for a single-layer of graphene in a sea of debris is a tedious task, but can be achieved with many hours of searching with the optical microscope. However, single-layer graphene and thicker flakes cannot be distinguished with 100% confidence via optical microscopy alone. Ferrari and coworkers showed that Raman spectroscopy can accurately determine the thickness of the flakes.[100] Using this technique, single-layers can be distinguished from bilayer, trilayer and thicker graphene layers by analyzing the carbon 2D Raman spectra peak.[101]

Although the successful isolation of a two dimensional crystal is remarkable, the truly amazing thing about single-layer graphene is the macroscopic electronic transport characteristics. Once a single-layer of graphene is successfully isolated, several electrical contacts can be fabricated using conventional microelectronics techniques adapted from the semiconductor industry.[18] One of the first electronic transport measurements of single-layer graphene flakes showed evidence of a new form of the integer Hall effect.

As a review, the classical Hall effect is used mainly in research as an accurate way to determine the density and type of charge carriers.[102] The four probe electrical transport technique (two parallel and two antiparallel to current flow) in an perpendicular magnetic field was developed by Edwin Hall more than 100 years. Closely related to the classical version, the quantum Hall effect (QHE) is only witnessed in pure and quasi-pure two-dimensional electron systems (2DES). The hallmarks of the QHE are plateaus in the Hall conductivity (measurement of current across antiparallel probes), which is in essence linear for the classical Hall.[103,104] More details of quantum Hall effect are extensively discussed elsewhere.[105] The plateaus of the QHE occur when the electrons (from the classical Lorentz force) form quantized circular orbits.[106,107] Under a large magnetic field, the once dense sea of electrons in the 2D system are condensed into highly degenerate levels, commonly known as Landau levels[102]. Two types of QHE exist, which are the integer- and fractional-Hall effect. The discoveries and interpretations of both types of QHE have resulted in Nobel prizes.[105,108-110] For the sequential sections, the integer QHE will only discussed. So far the fractional QHE has not been observed in graphene.

It was found experimentally that the graphene QHE has Hall conductivity plateaus located at different places than the plateaus from 2DES based on semiconductors. For a conventional 2DES the Hall plateaus and Landau level spacing (Figs. 3.1A &C) would occur at:[107]

$$\sigma_{xy} = \pm N \cdot (e^2 / h) \text{ , for } N = 0, 1, 2, ... \tag{3.1}$$

$$E_n = \pm \frac{\hbar e}{m^*} B(n + 1/2) \text{ , for } n = 0, 1, ... \tag{3.2}$$

where e is the electron charge, m^* is the effective mass of the electron, B is the magnetic field, and h is plank's constant with $h = 2\pi\hbar$. For single-layer graphene the plateaus Landau level spacing (Figs. 3.1B &D) were found to occur at:[16]

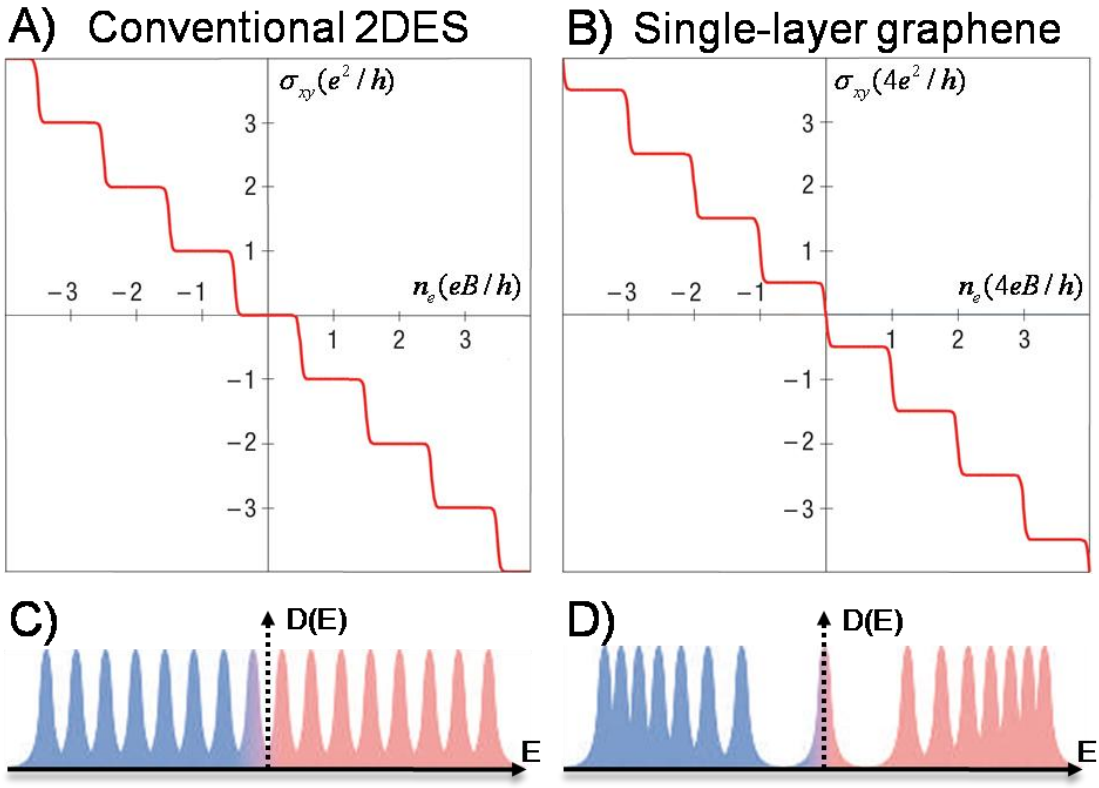

Figure 3.1

Two different types of integer quantum Hall effect. (A) Schematic plot of the Hall conductivity vs. carrier density. Conventional 2DES (with no spin degeneracy) has plateaus in the Hall conductivity that correspond to integer values of e^2/h centered at a carrier density equal to integer values of the Landau level degeneracy, eB/h. (B) Single-layer graphene has plateaus in the Hall conductivity that correspond to half integer multiplies of $4e^2/h$, with the center shifted by one half of the Landau level degeneracy, $4eB/h$. This new quantum Hall behavior is solely unique to single-layer graphene and is related to its novel electronic structure. Figures A & B are adapted from Ref. 111. (C) Schematic plot of the density of states versus energy for a 2DES, where the peak positions indicate Landau level location. Landau levels for a conventional 2DES are equally displaced by values of $\hbar eB/m^*$. Color indicates whether the Landau level is populated by electrons (blue) or holes (red). (D) Landau level spacing for single-layer graphene has a characteristic spacing that is proportional to $\sqrt{nB}$. In addition, at zero energy there is a Landau level that is equally populated by both electrons and holes. Figures C & D are adapted from Ref. 16.

$$\sigma_{xy} = \pm\ N + 1/2\ \ (4e^2/h), \text{ for } N = 0, 1, 2, \ldots \tag{3.3}$$

$$E_n = \mathrm{sgn}(n)\sqrt{2e\hbar v_F{}^2 |n| B}, \text{ for } n = 0, \pm 1, \ldots . \tag{3.4}$$

where v_F is the Fermi velocity. The "half-integer" Hall effect, as it is often called, is solely unique to single-layer graphene.[98,99] The reason for the difference in the Hall plateaus and Landau level spacing can be traced back to the unique electronic structure of graphene, as described later in this chapter. It is interesting to note that the graphene bilayer (two slightly coupled graphene sheets) also has a unique QHE, discussed later is this chapter.[111] Remarkably, of the three types of integer QHE, two are related to graphene systems.[16]

In addition to having a brand new QHE, the carrier mobility in the electron transport in graphene can be quite large.[98,99] Carrier mobility, typically extracted from the slope of the magnetoresistance (resistance over parallel contacts), can give information about carrier lifetimes, or how long before the charge carrier experiences an elastic scattering event.[112] The low temperature mobilities of single-layer graphene (on a substrate) can reach up to 2 x 10^4 cm^2/Vs,[98,113,114] still much lower than the state of the art strained Si/SiGe devices (5 x 10^5 cm^2/Vs)[115] or AlGaAs/GaAs heterostructures (1 x 10^7 cm^2/Vs).[116] Recently, suspended graphene (dangling above a substrate) has shown mobilities approaching 2 x 10^5 cm^2/Vs.[117,118] This is clear evidence that the substrate is actually one of the limiting factors in the transport properties of graphene.

In contrast to many semiconductor devices, both the QHE and the high mobilities of graphene are persistent at low carrier densities and room temperature.[119] This offers a clear advantage of graphene over conventional semiconductors, since most mainstream electronic devices will operate under these conditions. These exciting room temperature electronic transport results have raised interest from the technology and computer industry for device applications based on graphene.[13] However, the clear disadvantage of the graphene exfoliation technique is that the sample size is limited to around 10 μm x 10 μm.[16] This is quite small when considering that modern day Si transistors are fabricated

on an 8" wafers or larger.[120] To scale up to meet the demands for the computer industry, graphene grown epitaxially over an entire substrate offers one viable avenue.[16]

Epitaxial graphene on SiC offers a possible path for device applications and integration with mainstream electronics based on graphene.[16,47] Since the epitaxial graphene project was proposed in a 2001 (a National Science Foundation proposal later rejected), my colleagues at the Georgia Institute of Technology have developed techniques to grow unparalleled high quality epitaxial graphene films. Graphene of this type is grown in registry with the SiC substrate and electronic devices can be patterned with well-established lithographic procedures.[47,121] Electronic transport results from the Georgia Tech group and others have shown that the epitaxial graphene films on SiC retain most of the novel properties of isolated single-layer graphene flakes.[52] Very recent far infrared transmission measurements indicate that the epitaxial graphene might be of better quality than the exfoliated graphene with lower defect density and higher mobilities.[122] From these observations it is clear that the exfoliation technique has a role as a test of graphene's novel properties, but epitaxial graphene is better suited to solve the problem of electronic device miniaturization in the modern computer industry. However, both types of graphene have been used for devices for technical applications. In the next section, I will give a brief review of proposed and tested devices that have been designed for graphene.

3.1.2 Technological Interest

The first graphene-based devices were electrostatic-gate controlled conducting channels and simple Hall bars.[98,99] Making graphene into a device that can effectively switch on and off a source-drain current (essentially a transistor) was the first goal of researchers trying to make graphene nanoelectronics. However, with a similar electronic structure to metallic carbon nanotubes, large graphene sheets cannot make effective transistors due to the lack of an inherent band gap.[1] Some research efforts have been

focused on making graphene semiconducting for the purpose of fabricating transistors. The most promising avenue is band gap engineering based on confinement of the graphene, first demonstrated via electron beam lithography.[123] However, electron beam lithography is plagued with limitations to the lateral size of a ribbon. When the width of the ribbon (≈ 20 nm) becomes comparable to the line roughness of the lithography technique, the ribbon effectively becomes a graphene quantum dot.[124] Chemically derived graphene nanoribbons show potential for improved lateral confinement with smoother more well defined edges, resulting in an energy band gap around 0.4 eV.[51] Field effect transistors based on these graphene nanoribbon have shown promising performance, with a room temperature on-off ratio of around 10^6,[125] comparable to CNT and Si transistors.[10] The on-off current ratio is used as a benchmark of the performance of a transistor.[10]

The next step for graphene device formation was to fabricate bipolar transistors. Bipolar Si transistor were the choice for integrated circuits (IC) in the semiconductor industry until 1970 before the switch was made to the superior complementary metal–oxide–semiconductor (CMOS) technology.[126] Bipolar transistors are a three terminal device, where two P-N junctions (diodes) are connected with either the P or the N electrode shared, making a PNP or a NPN junction.[127] These types of devices can be made on the graphene with strategically placed top-mounted gate electrodes.[128-130] However, figuring out a recipe for an effective top-gate dielectric that could stick to the graphene has proved difficult for some groups.[131] However, due to the lack of a band gap in graphene, the current on-off ratio of these graphene bipolar transistors were poor, the best value reported was only a ratio of 6.[132] Chemically alternating the graphene to open up a bandgap before putting down a top-gate electrode has improved performance of the bipolar graphene transistor tremendously. One study has shown, perhaps due to water adsorption to the graphene, chemically altered graphene bipolar-transistors have a current on-off ratio of around 10^6, similar to what was achieved via lateral confinement

alone.[133] This type of device has the advantage of using only top-down fabrication methods without relying on chemically derived graphene flakes, which has the same fabrication problems of carbon nanotubes.[133] Similar to exfoliated graphene, a band gap can even be formed in epitaxial graphene by lateral confinement[121] and chemical alteration such as oxidation.[134] In contrast to single transistors on exfoliated graphene, it has been shown that hundreds of transistors can be fabricated from epitaxial graphene on a single wafer.[135]

Graphene has many uses for nanoelectronics that are not geared for mainstream transistors. Some research efforts have centered around using graphene for devices that act as a molecular sensors.[136] Since the purity of graphene is so high, with very little structural and lattice defects, added molecular adsorbates drastically change the electronic properties of the graphene.[132,137] Graphene has even been used as a transparent conductor for liquid crystal displays, opening the door for the use of graphene for optoelectronics. Sheets of graphene are also an effective grid material for transmission electron microscopy (TEM) measurements.[97] This line of research has allowed the study of such properties as the dynamics of adsorbed hydrogen,[138] and given a novel method to determine the fine structure constant.[139]

Many more graphene electronic devices have been theoretically proposed, however, the majority of them rely on the ability to accurately cut the graphene edges, which has proved challenging experimentally. It is clear that to fully unleash the potential of graphene for device applications, there has to be a more detailed understanding of the microscopic properties of graphene and how these properties relate to the macroscopic transport. This will be the foundation of the rest of this thesis. But first, I will talk about the actual physical and electronic properties of single-layer and bilayer graphene that have made all this excitement possible.

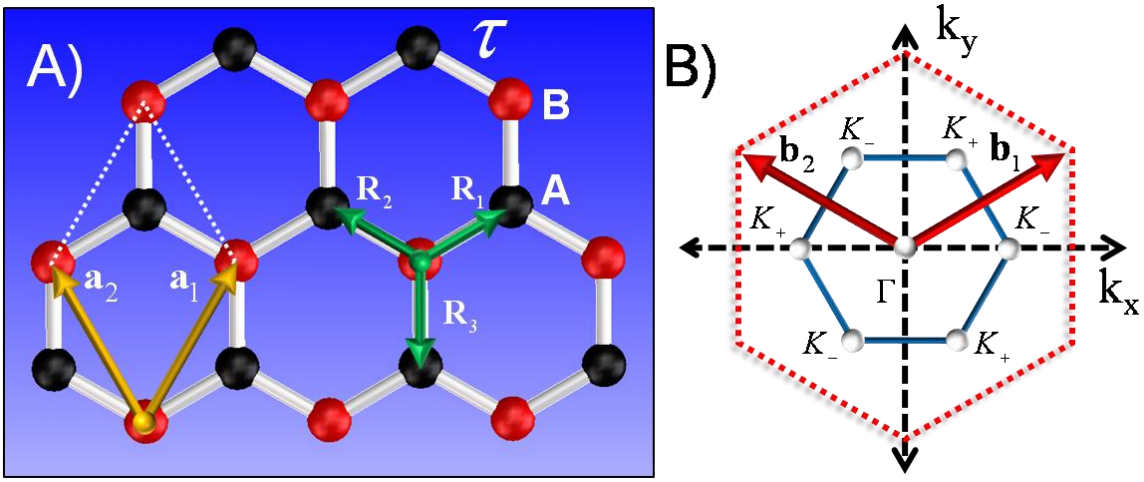

Figure 3.2

Real and reciprocal space geometry of single-layer graphene. (A) The lattice structure of ideal single layer graphene is made up of two sublattices, **A** and **B**. The unit cell (white diamond), enclosing these two atoms, is comprised of two hexagonal vectors $\mathbf{a}_1$ and $\mathbf{a}_2$ (gold arrows), with length 2.46 Å. Nearest neighbor atoms are defined by three translation vectors $\mathbf{R}_j$ (green arrows), with length 1.42 Å. (B) Reciprocal lattice of single-layer graphene, defined by the vectors $\mathbf{b}_1$ and $\mathbf{b}_2$ (red arrows). Blue hexagon outlines the first Brillouin zone of graphene, where the points of high symmetry are $\mathbf{\Gamma}$, $\mathbf{K}_+$, and $\mathbf{K}_-$.

3.2 Single-Layer Graphene

In this section, I will discuss the properties of ideal-single layer graphene. In particular, I will define the real and reciprocal space geometry of single-layer graphene. Next, I will give a derivation of the electronic band structure via the tight-binding model. I will then show how this model can be approximated to describe carriers in graphene as Dirac Fermions. In this approximation, the matter of the pseudospin will be addressed. Finally, I will discuss the role of ribbon width and edge termination on the graphene.

3.2.1 Geometry

As it turns out, many of the structural and electronic properties of graphene arise directly from the lattice structure.[19,34,35,140-142] The basic lattice structure of graphene (Fig. 3.2A) is made up of two interpenetrating hexagonal carbon sublattices, labeled **A**

(black spheres) and **B** (red spheres), forming a honeycomb pattern. The unit cell (white dotted diamond) contains two atoms, and is defined by the lattice vectors $\mathbf{a}_1$ and $\mathbf{a}_2$ (gold arrows) where

$$\mathbf{a}_1 = \frac{a}{2}\ 1, \sqrt{3} \tag{3.5}$$

$$\mathbf{a}_2 = \frac{a}{2}\ -1, \sqrt{3} \tag{3.6}$$

with the distance between honeycombs, $a = |\mathbf{a}_1| = |\mathbf{a}_2| = 2.46$ Å . Nearest-neighborhood carbon atoms are defined by translation vectors $\mathbf{R}_j$ (green arrows) where $j = 1, 2, 3$.

$\mathbf{R}_j$ can be written for the **B** atoms as:

$$\mathbf{R}_1 = \frac{a}{2}\left(1, \frac{\sqrt{3}}{3}\right) \tag{3.7}$$

$$\mathbf{R}_2 = \frac{a}{2}\left(-1, \frac{\sqrt{3}}{3}\right) \tag{3.8}$$

$$\mathbf{R}_3 = a\left(0, \frac{-\sqrt{3}}{3}\right) \tag{3.9}$$

with the distance between **A** and **B** atoms equal to 1.42 Å.[19] The bonds between the **A** and **B** carbon atoms have a strong interatomic coupling, $\tau \approx -3.0 eV$. The large value of τ is the reason for the strength and robustness of the in-plane sp^2-hybridized bonds.[14] Since the **A** and **B** atoms are identical carbon atoms, the graphene lattice has what is called sublattice symmetry. This sublattice symmetry influences the electronic structure of the graphene greatly. For example, it is well known that the crystal structure of boron nitride has a similar honeycomb lattice to graphene. However, since there are two

different atoms in the lattice (no sublattice symmetry), the electronic properties are very different from that of graphene.[143]

The 2D hexagonal real space lattice of graphene gives rise to a 2D hexagonal reciprocal space lattice, shown schematically as a red dotted hexagon in Fig. 3.2B. The reciprocal space lattice of graphene is defined by the vectors $\mathbf{b}_1$ and $\mathbf{b}_2$, red arrows of Fig. 3.2B, as

$$\mathbf{b}_1 = \frac{2\pi}{a}\left(1, \frac{\sqrt{3}}{3}\right) \tag{3.10}$$

$$\mathbf{b}_2 = \frac{2\pi}{a}\left(-1, \frac{\sqrt{3}}{3}\right). \tag{3.11}$$

The first Brillouin zone (BZ), defined as the area enclosed by the perpendicular bisectors of these vectors, is shown as a blue hexagon in Fig. 3.2B. In the graphene reciprocal lattice, there exist a few points of high symmetry. The first high symmetry point is the center of the BZ (labeled $\mathbf{\Gamma}$ in Fig 3.2B), where $\mathbf{k} = 0$. The other symmetry points are the six corners of the BZ (labeled $\mathbf{K_i}$, where i is + or - in Fig 3.2B). However, of the six total points there exist only two inequivalent points, $\mathbf{K}_+$ or $\mathbf{K}_-$, since a translation by a reciprocal lattice vector renders four of the points redundant. These points are defined as:

$$\mathbf{K}_+ = \frac{4\pi}{3a}(-1, 0) \tag{3.12}$$

$$\mathbf{K}_- = \frac{4\pi}{3a}(1, 0) \tag{3.13}$$

The electronic structure, discussed in a later section, will be localized around these six points in reciprocal space.

3.2.2 Electronic Structure of Graphene

As pointed out in Chapter 1, the electronic properties of all graphitic materials are mediated by the p_z-orbitals arising from the sp^2-bonding of the graphene lattice. Using only the p_z-orbitals contribution, the electronic structure of graphene was first calculated by Wallace in 1947 (≈ 60 years ago) to simplify the more complicated structure of graphite.[140] It was found that a simple tight binding formalism can be used to approximate the low energy electronic structure of an infinite graphene lattice.[19] To get information about the electronic structure or the energy vs. wavevector dispersion, $E(\mathbf{k})$, we first have to solve the Schrödinger equation:

$$\mathbf{H}\Psi = E(\mathbf{k})\Psi, \tag{3.14}$$

where $\mathbf{H}$ is the Hamiltonian matrix and Ψ are the wavefunctions. For the tight binding formalism, it is assumed that Ψ is a linear combination of Bloch functions Φ, where [19]

$$\Phi = \frac{1}{N}\sum_{\mathbf{R}}^{N} e^{i\mathbf{k}\cdot\mathbf{r}}\varphi_j(\mathbf{r}-\mathbf{R}), \quad (j = 1, \cdots, n), \tag{3.15}$$

where $\varphi_j(\mathbf{r}-\mathbf{R})$ denotes the actual atomic wavefunction in atomic orbital j (with total n), $\mathbf{R}$ is the atomic locations and N is the number of unit cells. In the tight bind model, it is assumed that the wavefunction, Eq. 3.15, is centered around or tightly bound to lattice sites.[102] To use any localized wavefunction for an infinite periodic lattice, the wavefunction would have to satisfy Bloch's theorem, which with a little algebra Eq. 3.15 clearly does.[19] The next step to achieve $E(\mathbf{k})$ is to solve the secular equation:

$$\det[\mathbf{H} - E(\mathbf{k})\mathbf{S}] = 0, \tag{3.16}$$

here **S** is the overlap integral matrix with elements defined as $S_{i,j} = \boldsymbol{\Psi}_i^* \boldsymbol{\Psi}_j$, where i, j = lattice sites **A** and **B**.[140] At this point the Slater-Koster scheme is typically used, where **S** is replaced with **I**, the identify matrix. In this scheme it is assumed that the wavefunctions are properly normalized ($\boldsymbol{\Psi}_i^* \boldsymbol{\Psi}_i = 1$), and the wavefunction do not overlap on the two lattice sites ($\boldsymbol{\Psi}_i^* \boldsymbol{\Psi}_j = 0$).[19] In determining the Hamiltonian, we assume that only p_z-orbitals contribute to the low energy electronic structure, resulting in 2 energy bands (each spin degenerate), reducing the Hamiltonian to a 2 x 2 matrix:[19]

$$\mathbf{H} = \begin{pmatrix} \mathrm{H}_{AA} & \mathrm{H}_{AB} \\ \mathrm{H}_{BA} & \mathrm{H}_{BB} \end{pmatrix}. \tag{3.17}$$

where $\mathrm{H}_{i,j} = \boldsymbol{\Psi}_i \mathbf{H} \boldsymbol{\Psi}_j$. The terms H_{AA} and H_{BB} turn out to be just the p_z-orbital energy (ε), but for simplicity we can define $\varepsilon = 0$ as an energy reference.[144] Since **H** is a Hermitian matrix, we can set $\mathrm{H}_{BA} = \mathrm{H}_{AB}^*$, where H_{AB}^* is the complex conjugate of H_{AB}.[19] The off-diagonal terms are calculated by assuming the Bloch wavefunctions, Eq. 3.15, in the product $\boldsymbol{\Psi}_A \mathbf{H} \boldsymbol{\Psi}_B$, described in detail elsewhere.[19] Therefore, this term becomes

$$\mathrm{H}_{AB} = \tau(\exp[i\mathbf{k} \cdot \mathbf{R}_1] + \exp[i\mathbf{k} \cdot \mathbf{R}_2] + \exp[i\mathbf{k} \cdot \mathbf{R}_3]) = \tau f(\mathbf{k}) \tag{3.18}$$

where the terms $\mathbf{R}_j$ are defined as the three translation vectors between nearest neighbor carbon atoms (Fig. 3.2A) ,and τ is the interlayer coupling constant.[19] Plugging in the vectors $\mathbf{R}_j$ (Eq. 3.7 - 3.9) into $f(\mathbf{k})$ yields:[19]

$$f(\mathbf{k}) = \exp\left[\frac{ik_y a}{\sqrt{3}}\right] + 2\exp\left[\frac{-ik_y a}{2\sqrt{3}}\right]\cos\left(\frac{k_x a}{2}\right). \tag{3.19}$$

Incorporating all this information yields a new form of **H**:

$$\mathbf{H} = \begin{pmatrix} 0 & \tau f(\mathbf{k}) \\ \tau f(\mathbf{k})^* & 0 \end{pmatrix}. \tag{3.20}$$

Next step is to solve the secular equation (Eq. 3.16), which yields the desired energy dispersion:

$$E(\mathbf{k}) = \pm\tau\sqrt{1 + 4\cos(\frac{\sqrt{3}k_y a}{2})\cos(\frac{k_x a}{2}) + 4\cos^2(\frac{k_x a}{2})} \tag{3.21}$$

where the "+" denotes bonding states and "$-$" denotes antibonding states.[19] Equation (3.21) is plotted three dimensionally in Fig. 3.3A. The band structure of graphene at low energy (Fig. 3.3A) consists of upright and inverted cones that meet at the charge-neutrality point [19,34,35] This particular energy position is commonly referred to as the Dirac point (E_D), for reasons explained below.[145] The conical hourglass structure is repeated at each of the six corners of the hexagonal BZ (hexagon of Fig. 3.3A), which includes the two inequivalent points labeled $\mathbf{K}_+$ or $\mathbf{K}_-$. The cones on these two points are also referred to as the valleys of graphene. [16]

A conical dispersion, similar to what was predicted from the tight binding dispersion model (Eq. 3.21), has been observed in single-layer graphene on SiC(0001) by angle resolved photoemission spectroscopy (ARPES).[146] However, the nature of the electronic structure near the Dirac point is still a matter of debate. There are two

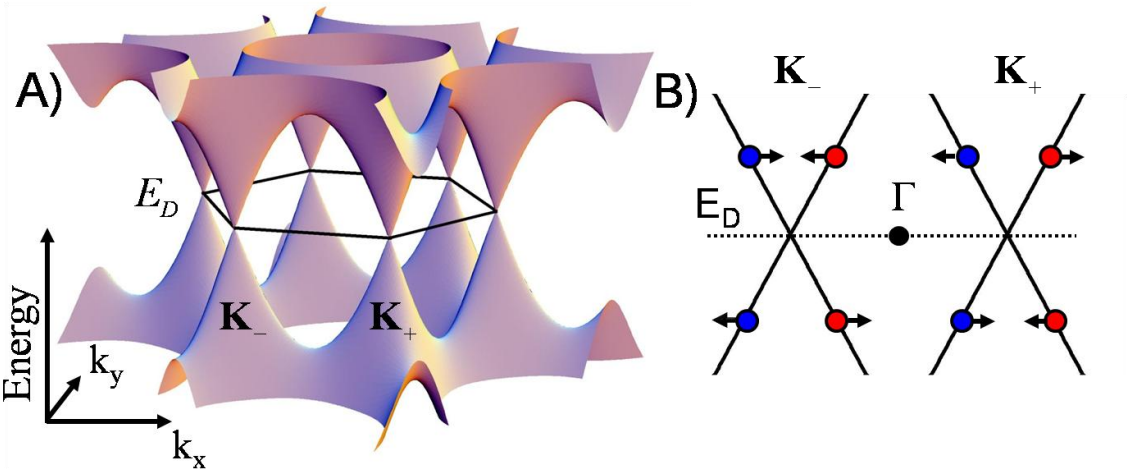

Figure 3.3

Electronic structure of single-layer graphene. (A) Electron energy versus wavevector dispersion for an infinite graphene sheet, derived from the tight-binding formalism discussed in the text. The plot shows the conical nature of graphene's electronic bands close to the Dirac point (E_D), where the electron and hole states meet. Seen in the plot are the two inequivalent points, $\mathbf{K}_+$ and $\mathbf{K}_-$, at the corners of the Brillouin zone (black hexagon). The other four corners are equivalent to either $\mathbf{K}_+$ or $\mathbf{K}_-$. (B) Slice of the energy dispersion for an infinite graphene sheet along $\mathbf{K}_- - \mathbf{\Gamma} - \mathbf{K}_+$. The pseudospin (arrow) points either parallel or anti-parallel to right moving (red circle) or left moving (blue circle) particles. The pseudospin depends on whether the particle is in the electron band (below E_D) or in the hole band (above E_D) and whether the particle is in the $\mathbf{K}_+$ or $\mathbf{K}_-$ valley.

conflicting theories (by two different groups) that have attempted to describe the dispersion near the Dirac point. It is clear that both groups agree that the dispersion at low energy is not a simple linear relation. One of the models suggests that the deviation from a linear dispersion is due to the opening of a band gap near the Dirac point.[147] It is felt that a substrate interaction between the graphene and the SiC substrate would lift the sublattice symmetry of graphene, essentially making the diagonal terms of the Hamiltonian (Eq. 3.20) non-zero. Similarly, due to the lack of sublattice symmetry in boron-nitride, a large energy gap exists.[143] The ARPES measurements have indicated that the lifting of the sublattice symmetry in graphene results in small energy band gap (roughly 0.4 eV).[147] Another theory postulates that the lack of a linear dispersion of epitaxial graphene on SiC(0001) at the Dirac point is related to electron-phonon

scattering.[148] The dispersion plots from this group show a kink in the dispersion near the Dirac point, which they explicitly say is not due to an energy gap. Each group, on occasion, have had the opportunity to refute the arguments of the other.[149,150] At the time of writing this review, the issue (kink vs. gap) of the energy dispersion near the Dirac point is still an open question and more measurements are needed to solve this debate.

Despite having wide appeal the simple tight binding model described above has a few shortcomings. Some studies have suggested that the above model does not reproduce the correct higher energy characteristics determined from lengthy first principles calculations.[151] To get a better agreement with these calculations, it was proposed that up to third-order lattice interactions and contributions from the overlap matrix $\mathbf{S}$ are necessary additions to the simple tight binding formalism.[151] However, for describing the low energy electronic structure, the simple tight binding method accurately models the graphene system. Moreover, other theoretical studies, only interested in the low energy properties of graphene, have simplified the full tight binding Hamiltonian further, outlined in the next section. This approximation is commonly used to extract many of the novel properties of graphene and carbon nanotubes.[152]

3.2.3 Dirac Fermions in Graphene

Since the low energy the electronic bands of graphene are linear in wavevector, the tight-binding Hamiltonian can be expanded to only include these terms. In addition, we can expand Eq. 3.18 around one of the corners of the BZ by making the transformation $\mathbf{k} = \mathbf{K}_+ + \boldsymbol{\kappa}$, where $\boldsymbol{\kappa}$ is a vector with origin at $\mathbf{K}_+$. A similar procedure is used to describe the $\mathbf{K}_-$ valley. To simplify Eq. 3.18, we use the fact that from Fig. 3.2A:[153]

$$\mathbf{R}_1 = \mathbf{R}_3 + \mathbf{a}_1 \tag{3.22}$$

$$\mathbf{R}_2 = \mathbf{R}_3 + \mathbf{a}_2 \tag{3.23}$$

$$\mathbf{R}_3 = \mathbf{R}_3, \tag{3.24}$$

combined with the mathematical result that

$$\exp[i\mathbf{K}_+ \cdot \mathbf{a}_1] = \exp[-i\frac{2\pi}{3}] \tag{3.25}$$

$$\exp[i\mathbf{K}_+ \cdot \mathbf{a}_2] = \exp[i\frac{2\pi}{3}] \tag{3.26}$$

$$\exp[i\mathbf{K}_+ \cdot \mathbf{R}_3] = 1. \tag{3.27}$$

Eq. 3.18 can then be rewritten

$$\mathrm{H}_{AB} = \tau \exp[i\boldsymbol{\kappa} \cdot \mathbf{R}_3] * (1 + C^* \exp[i\boldsymbol{\kappa} \cdot \mathbf{a}_1] + C \exp[i\boldsymbol{\kappa} \cdot \mathbf{a}_2]) \tag{3.28}$$

where $C = \exp[i\frac{2\pi}{3}]$. Now H_{AB} can be expanded using the approximation:

$$\exp[x] \approx 1 + x. \tag{3.29}$$

then Eq. 3.28 becomes:

$$\mathrm{H}_{AB} \approx \tau(1 + i\boldsymbol{\kappa} \cdot \mathbf{R}_3) * (1 + C^*(1 + i\boldsymbol{\kappa} \cdot \mathbf{a}_1) + C(1 + i\boldsymbol{\kappa} \cdot \mathbf{a}_2)). \tag{3.30}$$

Using the fact that

$$1 + C^* + C = 0 \tag{3.31}$$

and removing higher than linear order terms, Eq. 3.30 becomes:

$$\mathrm{H}_{AB} \approx i(C^{*}\boldsymbol{\kappa}\cdot\mathbf{a}_1 + C\boldsymbol{\kappa}\cdot\mathbf{a}_2))\tau + O(\boldsymbol{\kappa}^2)\,. \tag{3.32}$$

By plugging in $\mathbf{a}_1$ and $\mathbf{a}_2$ (Eq. 3.5 and 3.6), this equation transforms into:

$$\mathrm{H}_{AB} \approx \frac{\sqrt{3}\tau a}{2}(\kappa_x - i\kappa_y)\,. \tag{3.33}$$

The new form of the Hamiltonian for single-layer graphene is:

$$\mathbf{H} = \frac{\sqrt{3}\tau a}{2}\begin{pmatrix} 0 & \kappa_x - i\kappa_y \\ \kappa_x + i\kappa_y & 0 \end{pmatrix}. \tag{3.34}$$

The next step is to define the Fermi velocity:

$$v_F = \frac{\sqrt{3}\tau a}{2\hbar} \tag{3.35}$$

as well as remember the x and y Pauli matrices are:[57]

$$\sigma_x = \begin{pmatrix} 0 & 1 \\ 1 & 0 \end{pmatrix} \tag{3.36}$$

$$\sigma_y = \begin{pmatrix} 0 & -i \\ i & 0 \end{pmatrix}. \tag{3.37}$$

The Hamiltonian can now be simply written:

$$\mathbf{H} = \hbar v_F (\kappa_x \sigma_x + \kappa_y \sigma_y) = \hbar v_F \boldsymbol{\kappa} \cdot \boldsymbol{\sigma} . \tag{3.38}$$

For the $\mathbf{K}_-$ valley the Hamiltonian is similar except $\boldsymbol{\sigma}$ is replaced by $-\boldsymbol{\sigma}^*$, the complex conjugate of $\boldsymbol{\sigma}$.[153] Eq. 3.38 closely resembles a Dirac Hamiltonian for relativistic particles, but replacing the speed of light by v_F, where $v_F \approx \frac{c}{300} \approx 1 \times 10^6 \frac{m}{s}$.[16] It is also clear from the Hamiltonian that the mass of the carriers is irrelevant in the electronic properties of graphene. It is for these reasons why carriers in graphene are referred to as massless Dirac fermions, and why the charge neutrality point in the dispersion is called the Dirac point. Many theoretical studies have used the relativistic properties of neutrinos (uncharged Dirac-Weyl fermions) as an analogy to help describe the electrons in graphene.[152] One such property is pseudospin, which specifies the wavefunction amplitude on each of the two equivalent carbon sublattices, analogous to the two-component spinor describing electron spin.[154-156]

3.2.4 Pseudospin

Similarly to what is observed in neutrino physics, where a neutrino can have chirality that is either right-handed or left-handed, electrons in graphene have a similar sense of chirality, known as pseudospin. Chirality refers to the projection of $\boldsymbol{\sigma}$ on the direction of motion $\boldsymbol{\kappa}$ in Eq. 3.38.[154-156] The pseudospin is most readily seen in the wavefunctions that solve the graphene Dirac Hamiltonian. If we make the transformation:

$$\kappa_x + i\kappa_y = \kappa e^{i\varphi} \tag{3.39}$$

where $\tan\varphi = \frac{\kappa_y}{\kappa_x}$, to Eq. 3.34, then

$$\mathbf{H} = \hbar v_F \begin{pmatrix} 0 & \kappa e^{-i\varphi} \\ \kappa e^{i\varphi} & 0 \end{pmatrix}. \tag{3.40}$$

Next, we solve the secular equation to find the eigenenergies:

$$E(k) = \pm \hbar v_F \kappa . \tag{3.41}$$

We assume wavefunctions are of the Bloch form:

$$\mathbf{\Psi} \propto e^{i\boldsymbol{\kappa}\cdot\mathbf{r}} \begin{pmatrix} \alpha \\ \beta \end{pmatrix}. \tag{3.42}$$

Solving for the two wavefunctions yields

$$\mathbf{\Psi}_{K_\pm} = \frac{1}{\sqrt{2A}} e^{i\boldsymbol{\kappa}\cdot\mathbf{r}} \begin{pmatrix} s \\ e^{\pm i\varphi} \end{pmatrix} \tag{3.43}$$

where the $s = +1$ is for unfilled electron states, $s = -1$ represents electron filled states, and A is the area of the system.[152,153] The two component spinor associated with the wavefuntion is the pseudospin, which is closely related to the momentum vector $\boldsymbol{\kappa}$. Figure 3.3B pictorially describes the pseudospin component in the wavefunction of single-layer graphene. As the Fermi level moves through E_D due to doping or an applied electric field, the Fermi surface becomes circular with radius κ centered at $\mathbf{K}_\pm$. Seen in Fig. 3.3B is a vertical slice through the two Dirac cones. The chirality of electron states

around $\mathbf{K}_+$ is right-handed, where the pseudospin (arrow) is parallel to $\boldsymbol{\kappa}$. In the Fig. 3.3B, right moving states are colored red and left moving states are colored blue. Electron states around $\mathbf{K}_-$ are left-handed, where the pseudospin (arrow) is antiparallel to $\boldsymbol{\kappa}$. For hole states, the sense of chirality is reversed for both valleys. The pseudospin plays an important role in the macroscopic transport of graphene. When the electrons in graphene undergo a circular orbit (from say an applied magnetic field), the rotation of the pseudospin by 360° results in an additional phase of wavefunction of π; this quantum effect is known as a Berry's phase.[154] The combination of the linear dispersion of graphene and the Berry's phase of π gives rise to the half integer quantum Hall effect, described in earlier sections.

3.2.5 Ribbon Width and Edge Configuration

Some of the electronic properties of graphene are strongly dependent on the width of a graphene sample (ribbon) and how the edges are cut.[157] A finite size graphene ribbon, due to quantum confinement in the ribbon, has energy levels that are quantized into discrete values (indicated by orange arrows of Fig. 3.4A). The energy levels have a separation that is inversely proportional to the ribbon width (Fig. 3.4A).[49,158] This is similar to the quantum mechanical problem of a "particle in a box", where the energy levels are also quantized and the spacing is dependent on the spatial box size.[57] Recent transport measurements on graphene ribbons have shown that the gap between valence and conduction states varies inversely with the graphene width, but some complications in defining the "exact" width of the ribbon remain.[51,123]

A graphene ribbon has two low-energy configurations for the edges, labeled in Fig. 3.4B as armchair and zigzag. For the case of a zigzag edge, a single low-energy electronic band appears near the Fermi energy (Fig. 3.4A).[48] This energy level is only represented by one pseudospin with the same pseudospin characteristics as $\mathbf{K}_+$ or

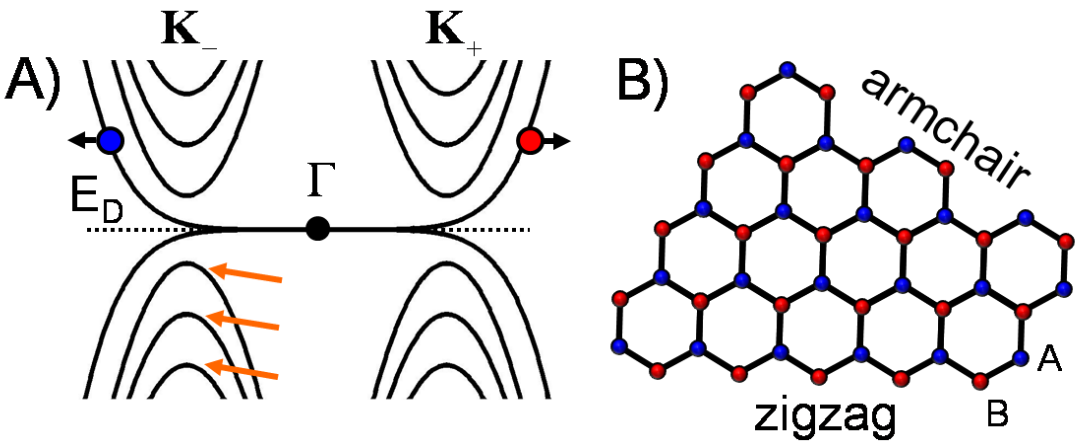

Figure 3.4
Dependence of ribbon width and edge configuration on the electronic structure of graphene. (A) Slice of the energy dispersion for a confined graphene ribbon with zigzag edges. The confined geometry yields discrete energy levels for the valleys, indicated by orange arrows. The pseudospins for the valleys are the same as the case for an infinite graphene ribbon. Due to the zigzag edge configuration, there appears a single band near the Dirac point that has only one pseudospin represented. (B) A graphene ribbon can have two different edge terminations, armchair or zigzag, where each configuration has profound effects on the electronic structure.

K_ valley.[159] In contrast, for an armchair edge the lowest energy levels would be represented by both pseudospins, similar to an infinite graphene ribbon (Fig. 3.3A).[48] This single energy level of a zigzag edge arises from more dangling bonds on one sublattice as compared to the other sublattice (Fig. 3.3 B). In the case of an armchair edge, Fig. 3.4B, there is the same number of broken edge-bonds for each sublattice. Recently, it has been shown experimentally that a zigzag edge yields a localized state in the density of states near the Dirac point, where an armchair edge does not.[160] A zigzag edge nanoribbon has even been proposed to filter out the pseudospin component of the graphene wavefunction all together.[159] A potential device could use this inherent degree of freedom of graphene as a computational variable for future electronic devices.[159]

3.3 Bilayer Graphene

In this section, I will discuss the properties of bilayer graphene, and how they relate to those of single-layer graphene. First, I will discuss the lattice structure of bilayer

graphene and multilayer graphene. Second, I will discuss the electronic structure of bilayer graphene. Finally, I will discuss the differences between single-layer graphene and bilayer graphene with respect to the local density of states.

3.3.1 Geometry

When a second graphene layer is added to form bilayer graphene, the sublattice symmetry can be broken, resulting in variations of the electronic properties that depend on the stacking.[111,161,162] Figure 3.5 shows the lattice structure of bilayer graphene, illustrated in a Bernal stacking configuration, the most common form of graphite.[21] The bilayer is comprised of two graphene planes vertically offset by 3.35 Å.[19] The second plane of graphene is rotated 180º so as to line up the **A** atoms (black atoms) in the top layer (labeled **A**´) and the **A** atoms in the bottom layer. In this stacking configuration, the **B**´ and **B** carbon sublattices (red atoms) are located in the hollow sites of the bottom and top graphene layer, respectively. This stacking configuration results in a weak coupling between only the **A** atoms of the two layers, and is described by the inter-layer coupling constant $\tau_{\perp}$, where $\tau_{\perp} \approx 0.4eV$. [163,164]

Depending on the layer orientation, graphene stacks with two or more layers are either described as ultrathin graphite or multilayer graphene. For the ultrathin graphite variety, the stacking can continue the Bernal stacking trend, where the next layer would be aligned with the first graphene layer, so ABA stacking. However, there are other types of stacking that can also occur. The third layer can have different position as compared to the A and B layers, which is called rhombohedral stacking or ABC stacking. In rhombohedral stacking, the third layer of graphene couples only with the **B** atoms of the second layer, leaving the **A** atoms of the second layer over hollow sites.[21]

For the samples that are characterized as multilayer graphene, the relative layers are believed to be uncoupled. The decoupling between the layers is proposed to isolate the layers, so each layer can be thought of as a single-layer of graphene. Graphene layers

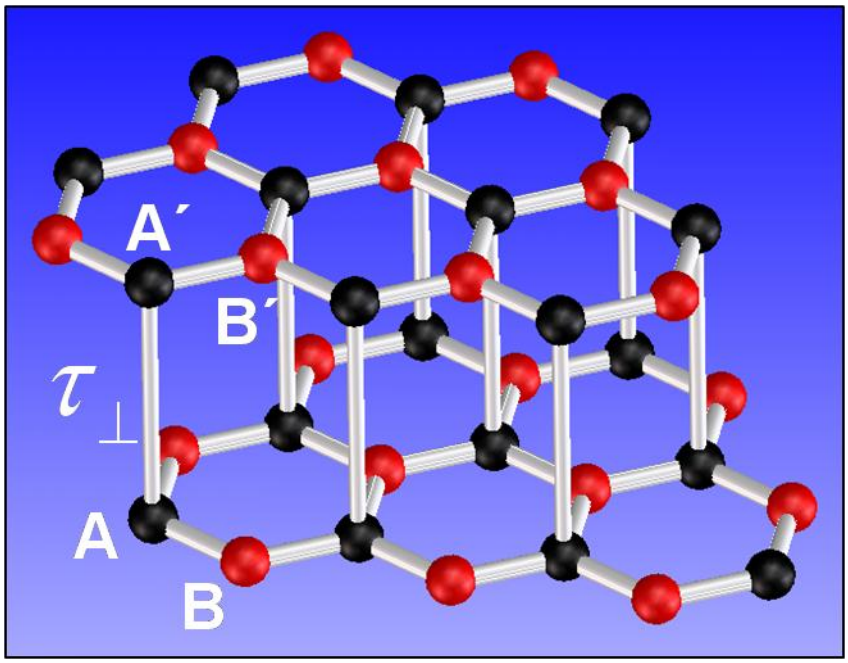

Figure 3.5

3D rendering of the lattice structure of bilayer graphene in a side view. Bilayer graphene is made up of two graphene planes stacked one on top of another. The most common form of bilayer, Bernal stacking, involves the top-most graphene plane being rotated 180˚ with respect to the first. This aligns the **A** atoms of the bottom layer with **A´** atoms in the top layer. In this configuration, there is a weak inter-layer coupling ($\tau_\perp \approx$ 0.4 eV) between the two graphene layers.[163,164] This weak coupling breaks the sublattice symmetry of ideal graphene.

that are rotated with respect to one another have been calculated to conserve single-layer graphene properties.[165-167] This rotational layer orientation is seen in turbostratic graphite, where the layers are randomly rotated.[14] Of particular interest to epitaxial graphene studies is that the stacking sequence of graphene layers does not necessarily have to be well defined. The stacking of multilayer graphene on the carbon rich face of the SiC grows in a similar turbostratic-like configuration, where the interleaved layers are rotationally offset from one another with lateral domains are far larger than turbostratic graphite.[166] It has been proposed that this rotation is what essentially makes multilayer graphene on carbon faced-SiC have single-layer graphene properties, discussed elsewhere.[166] For the silicon rich face of the SiC, the graphene bilayers grow in a Bernal

stacking configuration. In the next section, the effect of Bernal stacking on the electronic properties of bilayer graphene will be addressed.

3.3.2 Electronic Structure of Bilayer Graphene

Bilayer graphene (with Bernal stacking seen in Fig. 3.5) has a different electronic structure as compared to the ideal single-layer graphene. The stacking of the second graphene layer causes hybridization of the bonding orbital between the **A** and **A´** atoms, which essentially adds two more energy bands (each spin degenerate).[168] This means for bilayer graphene we expect four low energy bands total, in contrast to the two seen in single-layer graphene. The tight binding Hamiltonian is determined by the different electron coupling paths between the layers.[168] For example, an electron can hop from the lattice sites **B→A→A´→B´,** this coupling path goes directly through the bond between **A** and **A´** atom. A more general calculation would take into account the direct coupling **B→B´**, but this is neglected in the derivation that follows.[161] To determine the energy dispersion, first we need to define the Hamiltonian for bilayer graphene. The approximated tight-binding Hamiltonian expanded around a $\mathbf{K}_{\pm}$ point can be written:[168]

$$\mathbf{H} = \xi \begin{pmatrix} \frac{-\Delta}{2} & 0 & 0 & v_F\pi^* \\ 0 & \frac{\Delta}{2} & v_F\pi & 0 \\ 0 & v_F\pi^* & \frac{\Delta}{2} & \xi\tau_\perp \\ v_F\pi & 0 & \xi\tau_\perp & \frac{-\Delta}{2} \end{pmatrix} \tag{3.44}$$

where Δ is the induced asymmetry between the layers (described below), v_F is the in-plane velocity defined in Eq. 3.35., $\xi = \pm 1$ for $\mathbf{K}_{\pm}$, and $\pi = \hbar(\kappa_x + i\kappa_y)$. Solving the secular equation (Eq. 3.16) gives four solutions, one for each of the energy bands in

bilayer graphene. Determining $E_{\pm}^{\alpha}(k)$ (with $\alpha = 1,2$, and $\pm$ for the unfilled and filled electron states, respectively) yields an expression:[168]

$$E_{\pm}^{\alpha}(k) = \pm\left(\frac{\tau_{\perp}^{2}}{2} + \frac{\Delta^{2}}{4} + (v\hbar\kappa)^{2} + (-1)^{\alpha}\sqrt{\frac{\tau_{\perp}^{4}}{4} + (v\hbar\kappa)^{2}(\tau_{\perp}^{2} + \Delta^{2})}\right)^{1/2} \qquad (3.45)$$

Results from Eq. 3.45 for an isolated graphene bilayer ($\Delta = 0$) are plotted in Fig. 3.6A. The plot takes into account typical values for $\tau_{\perp}$ and v_F, described in previous sections. From the plot in Fig. 3.6A, it is clear that the energy vs. wavevector dispersion is very different from that of a single-layer of graphene. In particular, the dispersion is hyperbolic near the Fermi energy, while the single-layer remains linear. In addition, the separation between the two hyperbolic bands on either side of the Fermi energy is the interlayer coupling, $\tau_{\perp}$.[169] Another interesting aspect of Bernal stacked bilayer graphene electronic structure is that a controllable energy gap can be induced by an electric field perpendicular to the layers.[170] Figure 3.6B shows a plot of the dispersion with a large value of asymmetry between the layers, with $\Delta = \tau_{\perp}$. The size of the energy gap is essentially determined by the potential difference between the layers. This property, as well as other inherent characteristics, make bilayer graphene also enticing for potential device applications.[16,17,171]

ARPES measurements of bilayer graphene on SiC have verified the predicted bands of the energy dispersion.[147,172] In addition, a gap is also observed that is similar to what is predicted for a biased bilayer graphene.[173] In epitaxial graphene, the graphene layer closest to the substrate will be doped due to charge transfer from the interfacial reconstruction, where the top layer is essentially neutral. This equates to a potential difference between the two graphene layers, and a gap opens up in the dispersion. In addition, the adsorption of charged metal atoms on the top most graphene layer will

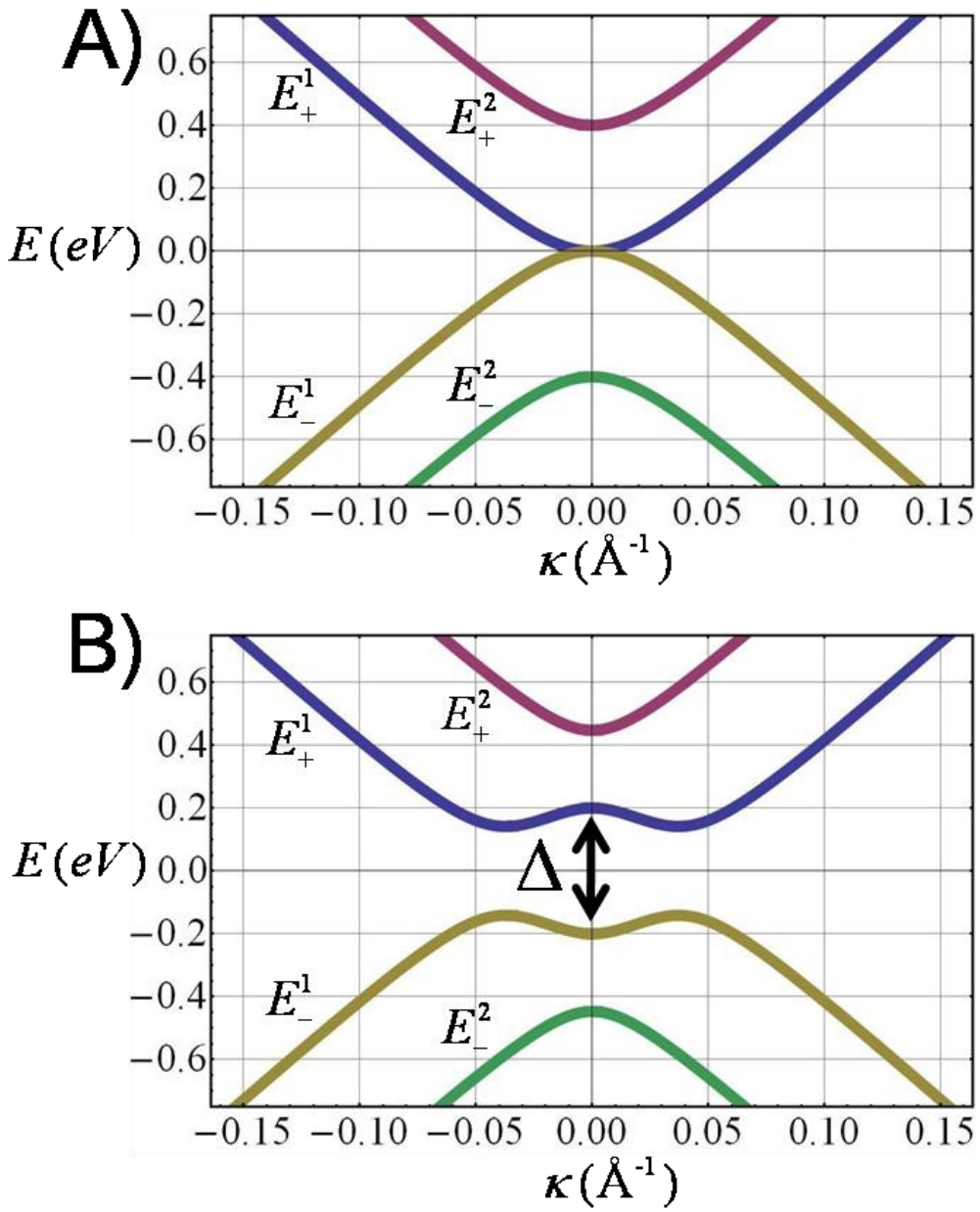

Figure 3.6
Electronic structure of bilayer graphene. (A) Energy vs. wavevector dispersion for Bernal stacked bilayer graphene with interlayer interaction $\tau_\perp \approx 0.4eV$. The dispersion was derived from a simplified tight-binding formalism described in the text. At low energy the bilayer bands (a total of four levels) are hyperbolic, while the single-layer remains linear. (B) Electronic dispersion for bilayer graphene when a potential difference (Δ) is introduced between the layers. Plotted here is the dispersion with $\Delta \approx 0.4eV$. This type of dispersion as been observed on bilayer epitaxial graphene, where charge transfer from the underneath substrate induces the potential difference between the layers.

reduced the potential difference and closes the gap. This is what was seen on bilayer epitaxial graphene with different amounts of adsorbed potassium atoms on the surface.[173]

From an electronic transport point of view the Hamiltonian of bilayer graphene can be simplified back to a 2 x 2 matrix with the form:

$$\mathbf{H} = \frac{-1}{2m}\begin{pmatrix} 0 & (\pi^2)^* \\ \pi^2 & 0 \end{pmatrix} \tag{3.46}$$

where $m = \tau_\perp / 2v_F^2$.[161] The Hamiltonian for bilayer graphene somewhat resembles the usual form for conventional free electrons, $\mathbf{H} = \frac{(\hbar\kappa)^2}{2m}$. However, the fact the Eq. 3.46 still has an analogous matrix single-layer form suggests that the carriers in bilayer graphene are still quasiparticles, and they are commonly referred to as massive Dirac fermions. To make the analogy between single-layer and bilayer graphene complete, both of the Hamiltonians can be written in the form:

$$\mathbf{H}_j = E(\kappa)\boldsymbol{\sigma}\cdot\boldsymbol{\eta}(\varphi) \tag{3.47}$$

with

$$\boldsymbol{\eta}(\varphi) = -(\cos J\varphi, \sin J\varphi) \tag{3.48}$$

where $\boldsymbol{\eta}(\varphi)$ is the pseudospin vector with $\tan\varphi = \kappa_y / \kappa_x$, and $J = 1$ for single-layer graphene and $J = 2$ for bilayer graphene.[111] Therefore, the quasiparticles in bilayer graphene are still considered chiral, but now the wavefunction acquires a Berry's phase of 2π upon a closed orbit.[111] It is this new Berry's phase that gives rise to the novel bilayer graphene integer QHE, introduced earlier in this chapter. In this case, for

electronic transport (where the higher energy bands are irrelevant) the Hall plateaus and Landau levels are:[161]

$$\sigma_{xy} = \pm N \cdot (4e^2 / h) \text{ , where } N = 1, 2, ... \tag{3.49}$$

$$E_n = \pm \frac{\hbar eB}{m^*} \sqrt{n(n-1)} \text{ , where } n \geq 2 \tag{3.50}$$

There are two degenerate Landau levels at $E = 0$, which correspond to the $n = 0,1$. The values of Eq. 3.49 are similar to those for a conventional semiconductor except the Hall plateau at zero energy is missing due the filling of a doubly degenerate Landau level (made up from $n = 0,1$).[111] A more general approach considering higher energy bands would lead to a Landau level spacing:

$$E_n = \frac{\text{sgn}(n)}{\sqrt{2}} \left[(2|n|+1)\beta^2 + \tau_\perp^2 - \sqrt{\tau_\perp^4 + 2(2|n|+1)\beta^2\tau_\perp^2 + \beta^4} \right]^{1/2} \tag{3.51}$$

where $n = \pm 1, \pm 2, ...$ and $\beta = \sqrt{2eBv_F^2\hbar}$.[169,174]

There are other key differences that arise between the single-layer graphene and bilayer graphene, one in particular is seen in the local density of states (LDOS).[163,164] For a single-layer of graphene when both the **A** and **B** carbon atoms are indistinguishable, the LDOS for the **A** and **B** atom are:

$$LDOS_A(E) = LDOS_B(E) = \frac{A|E|}{\pi(\hbar v_F)^2}, \tag{3.52}$$

where A is the area of the graphene unit cell, $A = \frac{3\sqrt{3}a^2}{2}$.[157] The LDOS for single-layer graphene, identical for both carbon atoms, is linear with respect to energy and goes to

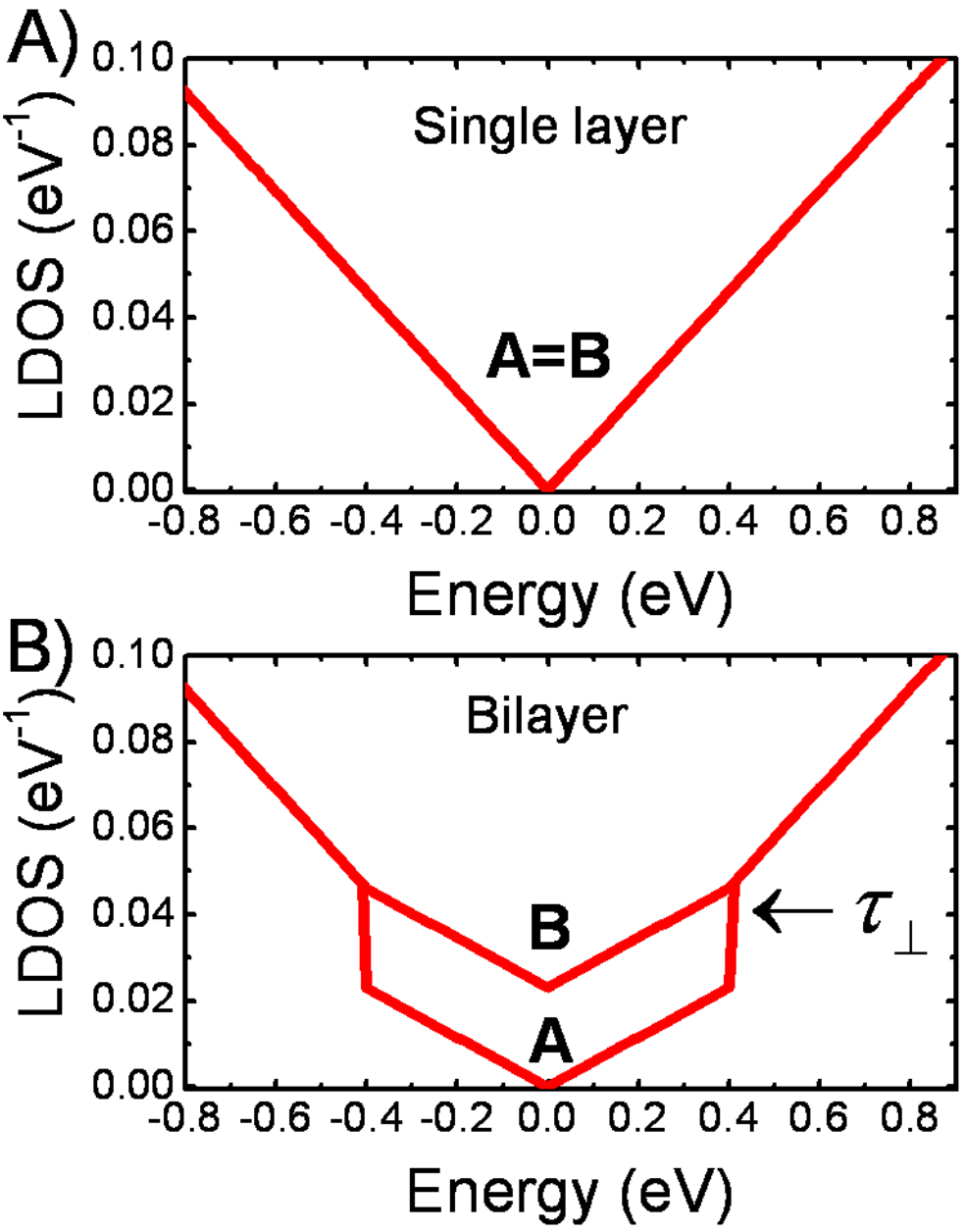

Figure 3.7
Sublattice dependent LDOS for single-layer (A) and bilayer (B) graphene. For the single-layer case, when the sublattice symmetry is intact, the LDOS is the same at all energies for the **A** and **B** sublattices. For the bilayer case, when the sublattice symmetry is broken, there is a reduction in the LDOS of the **A** sublattice as compared to the **B** sublattice. This reduction arises from the interlayer coupling between the two layers, but only over the interval $\pm\tau_\perp$. At energies above $\tau_\perp$ the sublattice symmetry is once again recovered.

zero at the Dirac point, E= 0 (Fig. 3.7A).[164] Due to a weak coupling between the layers of strength $\tau_\perp$, bilayer graphene has a remarkably different LDOS as compared to the monolayer. For bilayer graphene the LDOS for the **A** and **B** atom are given by the expressions:[164]

$$LDOS_A(E) = \begin{cases} \dfrac{A|E|}{\pi(\hbar v_F)^2} \; for \; |E| > \tau_\perp \\ \dfrac{A|E|}{2\pi(\hbar v_F)^2} \; for \; |E| < \tau_\perp \end{cases} \tag{3.53}$$

$$LDOS_B(E) = \begin{cases} \dfrac{A|E|}{\pi(\hbar v_F)^2} \; for \; |E| > \tau_\perp \\ \dfrac{A(|E| + \tau_\perp)}{2\pi(\hbar v_F)^2} \; for \; |E| < \tau_\perp . \end{cases} \tag{3.54}$$

The LDOS for isolated bilayer graphene is plotted in Fig. 3.7B. The coupling between the layers results in a reduction of the LDOS for the **A** atoms as compared to the **B** atoms over the interval $\pm\tau_\perp$. We propose that since the STM can probe the local density of states of the sample, we should be able to accurately measure the differences in the LDOS for bilayer graphene (discussed in Chapter 6). This concludes our derivation of the electrical properties of single-layer and bilayer graphene. Next, we will move to a discussion of the scattering properties of graphene.

3.4 Scattering in Graphene

Understanding the role that defect scattering plays in the transport properties is pivotal for any system used for electronic devices; this is no different for the case of graphene. Defect scattering is a process where an electron experiences a change in momentum after interacting with disorder. There are two main two types of defect scattering: elastic and inelastic scattering. Inelastic scattering involves the loss of energy in addition to the change in momentum; for simplicity this type will not be discussed

further. We will only concern ourselves with elastic scattering, where the energy of the electron doesn't change. To illustrate elastic scattering in graphene, we use two-dimensional constant energy contours in reciprocal space (Fig. 3.8). For graphene the constant energy contours near E_F cut through the electron and hole conical dispersions resulting in small circles of radius κ, centered at the wavevectors $\mathbf{K}_+$ and $\mathbf{K}_-$. The scattering wavevectors $\mathbf{q}$ connect different points on the constant energy contours (Fig. 3.8). Two dominant families of scattering vectors, labeled $\mathbf{q_1}$ and $\mathbf{q_2}$, are allowed in graphene. Wavevectors $\mathbf{q_1}$ connect points on a single constant-energy circle (intravalley scattering) while wavevectors $\mathbf{q_2}$ connect constant-energy circles at adjacent $\mathbf{K}_+$ and $\mathbf{K}_-$ points (intervalley scattering).

Since graphene shares many of the transport characteristics of carbon nanotubes (CNTs), we can use the extensive theoretical work for scattering in CNTs and relate that to graphene. In particular, elastic intravalley scattering of CNTs has been studied extensively.[154,155,175] These studies predict that for metallic CNTs, elastic scattering is greatly reduced for surface potential variations that are large compared to the atomic scale. Disorder of this type can arise from structural ripples in CNT or coulomb potentials from distant charged impurities. When an electron experiences disorder in the sample, an extra potential (2 x 2 matrix) is added to the existing Hamiltonian. This potential energy matrix only has diagonal elements that can be written:

$$\left|\Psi_{\kappa_2} V(\mathbf{r}) \Psi_{\kappa_1}\right|^2 = \left|V(\kappa_1 - \kappa_2)\right|^2 \cos^2\left[\frac{\theta}{2}\right] \tag{3.55}$$

where $V(\mathbf{r})$ is the potential energy from the disorder , κ_1 is the initial state wavevector, κ_2 is the final wavevector after the scattering event, and θ is the angle

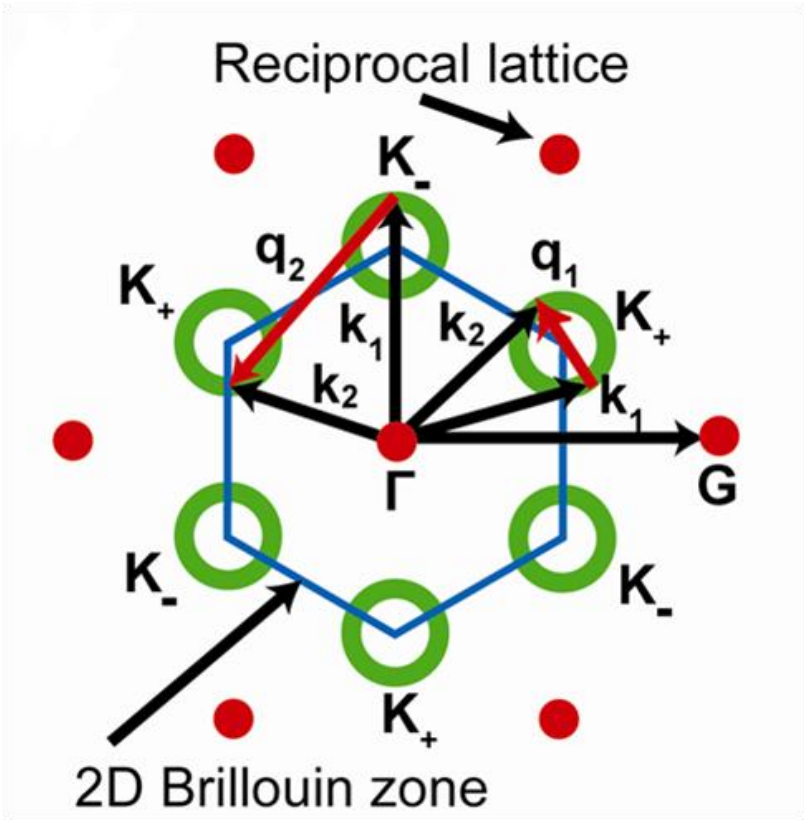

Figure 3.8
Schematic of the 2D Brillouin zone (blue), constant energy contours (green) at the $\mathbf{K}_{\pm}$ points, and the two dominant classes of scattering vectors that create interference patterns in graphene. Scattering wavevectors $\mathbf{q_1}$ (red) are seen to connect points on a single constant-energy circle, and $\mathbf{q_2}$ (red) connects points on constant-energy circles between adjacent $\mathbf{K}_+$ and $\mathbf{K}_-$ points.

between κ_1 and κ_2.[155] For metallic CNT the dispersion is identical to what is plotted in Fig. 3.3B.[155] The Fermi surface, made up of only two points, has κ_1 as a right moving electron and κ_2 as a left moving electron, where $\theta = \pi$. This angle between the scattering vectors will result in a vanishing matrix element (Eq. 3.55), resulting in suppressed intravalley scattering. This suppressed scattering is a consequence once again of the pseudospin and π-Berry's phase. For a semiconducting CNT (non-linear dispersion), even though the Fermi surface is still comprised of two points, $\theta < \pi$. Therefore, the scattering in semiconducting CNT is not strongly suppressed.[155] It is

interesting to note that scattering due to disorder with size on the order or smaller than the unit cell will not be suppressed for any type of CNT. This disorder will lead to off-diagonal matrix elements to the Hamiltonian. Disorder of this type is represented by point defects and vacancies that occur in or under the lattice.

For single-layer graphene, like CNT, it is predicted that weak potentials will not allow intravalley scattering events, while short range scatters will result in such scattering. This result has been noted in many theoretical studies.[156,176-178] Many of the transport properties in graphene are affected by the conservation of chirality and pseudospin in long-wavelength scattering processes. In particular, for monolayer graphene the reduction in backscattering can even lead to weak antilocalization.[156,179] High mobilities and long-coherence lengths in graphene and carbon nanotubes can then be traced to the conservation of pseudospin and lack of intervalley and intravalley scattering. [154]

The matter of testing intervalley and intravalley scattering can be done with the help of Fourier transform scanning tunneling spectroscopy (FTSTS), which is discussed in the last chapter of this thesis.[180,181] Fourier transforms of dI/dV maps are essentially $\mathbf{q}$-space images of the allowed scattering vectors in graphene. It has been proposed that reduced intravalley scattering of monolayer graphene is seen as a reduction in the intensity close to $\mathbf{q}=0$, where normally $\mathbf{q_1}$ scattering would exist.[182,183] Even though $\mathbf{q_1}$ scattering is suppressed, intervalley scattering ($\mathbf{q_2}$) will always appear as features centered at the $\mathbf{K}_+$ and $\mathbf{K}_-$. Chapter 7 will talk more about the scattering measurement of epitaxial graphene with FTSTS.

3.5 Epitaxial Graphene on SiC

Epitaxial graphene offers the first potential avenue for the use of graphene with mainstream electronic applications. The fact that thin graphite films form on the surface SiC has been known for 30 years.[184] SiC is a bilayer crystal that forms into over a

hundred different polytypes, distinguished only by the stacking of the SiC bilayers.[185] The most common polytopes for graphene growth are 4H-SiC and 6H-SiC.[185] Under vacuum conditions it has been shown that when annealed to sample temperatures in excess of 1200 ºC, graphitization occurs at the surface of SiC.[93] Epitaxial graphene can be studied by a variety of surface science techniques, such as STM, STS, LEED, Auger electron spectroscopy, x-ray diffraction, among many others.

It is interesting to note that SiC has two polar faces, corresponding to a Si terminated face (0001) or a C terminated face $(000\bar{1})$. The graphene growth mechanism is quite different on either face. The growth on the carbon-rich face is far less understood, the films are thicker (10 to 100 ML of graphene) and they also have interleaved rotational stacking faults.[186] Si-face graphene can be grown thinner and with a higher degree of control.[186] Si-face epitaxial graphene grows in perfect registry with the underlying substrate, and multiple layers are Bernal stacked. It has been shown that the electronic transport properties are different on either polar face.[52] The carbon face films usually have higher mobility and longer mean free paths as compared to the Si-face type.[52] For the rest of my work, I will focus on the atomic scale properties of epitaxial graphene grown on the silicon face, to study the growth and electronic properties of very thin graphene films. To unearth these properties, I employ scanning tunneling microscopy (STM) and scanning tunneling spectroscopy (STS) at room temperature (300K) and low temperature (4.2 K).

CHAPTER 4

INITIAL STAGES OF EPITAXIAL GRAPHENE GROWTH

4.1 Introduction

To fully characterize the electronic properties of epitaxial graphene, a clear understanding of the growth mechanisms is vital. The properties of initial epitaxial graphene formation will be characterized by RTSTM and RTSTS measurements. From our studies, we have found that graphene on SiC(0001) mimics the growth processes of metallic thin films. Metal thin films have been studied extensively using STM and other surface science techniques. From these studies it was found that metallic films grow from deposited adatoms through nucleation on step edges or islands.[187] The nucleation process depends on many factors such as the number of surface step edges, the metal atom flux, the surface diffusion coefficients, as well as others.[188]

In epitaxial graphene growth, instead of a flux of atoms like in metal deposition, carbon is introduced by desorbing Si atoms from the surface at temperatures well over 1000 ºC.[189] The desorption of silicon results in a carbon rich environment, where mass transport of carbon can occur. The combination of high temperatures (large diffusion coefficient) and high step density equates to a heighten nucleation of a film on a step edge instead in the form of islands.[190] In this chapter, I will show that this type of growth is prevalent for the case of epitaxial graphene on $SiC(000\bar{1})$. However, we have found evidence of graphene island formation, though less frequent than terrace growth. To my knowledge, this is the first study that characterizes the properties of epitaxial graphene islands. In a later section of this chapter, I will discuss the composition of the SiC reconstruction, and discuss how it contributes to the growth of the epitaxial graphene.

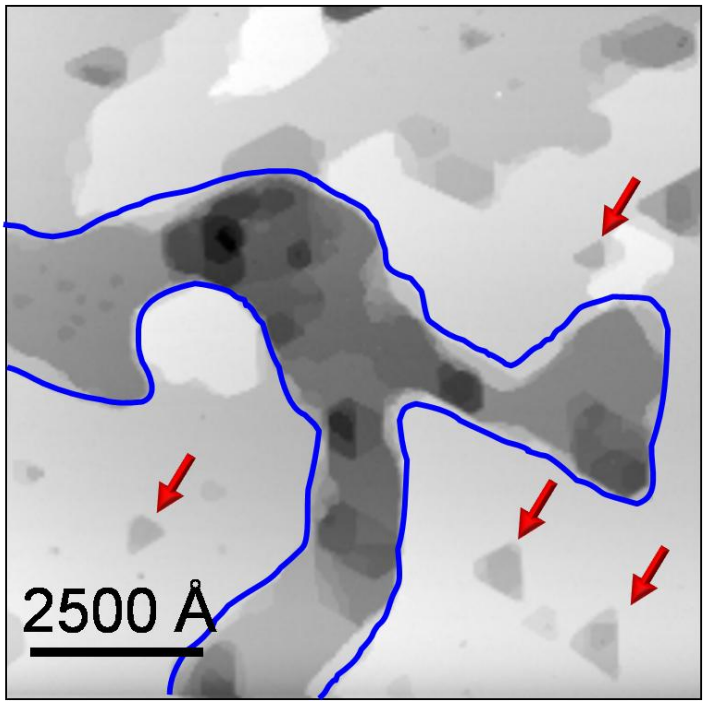

Figure 4.1

Large scale RTSTM topography (1 μm x 1 μm) showing the surface morphology of the SiC (tunneling conditions are 1.0 V and 0.1 nA). There are many triangular etched pits (red arrows) on the surface after annealing. The angle of the pits follows closely the preferred directions of the hexagonal SiC reconstruction. In the center of the image is a large trench (blue outline), which is common when annealing the Si-face of the SiC. There are many smaller triangular pits in the trench as compared to the outside the trench.

4.2 Graphene Step Edge Growth

When graphene forms on the surface of SiC(0001), the morphology of the sample changes greatly from the ordered step array seen in hydrogen-processed SiC samples[191,192] Figure 4.1 shows an STM topograph (1 μm x 1 μm) of the SiC(0001) surface after UHV graphitization. This image shows that the surface is decomposing as the silicon of the first few SiC layers desorbs from the sample. The surface now has many triangular pits indicated by red arrows in Fig. 4.1. This type of decomposition is common for the Si-face-SiC(0001) graphitization.[191,193] The triangular pits are all shaped with edges that follow the SiC reconstruction's hexagonal directions, with edges that are either 60º or 120º apart. Another interesting feature of the STM topography is a large trench found in the middle of the image, highlighted by the blue

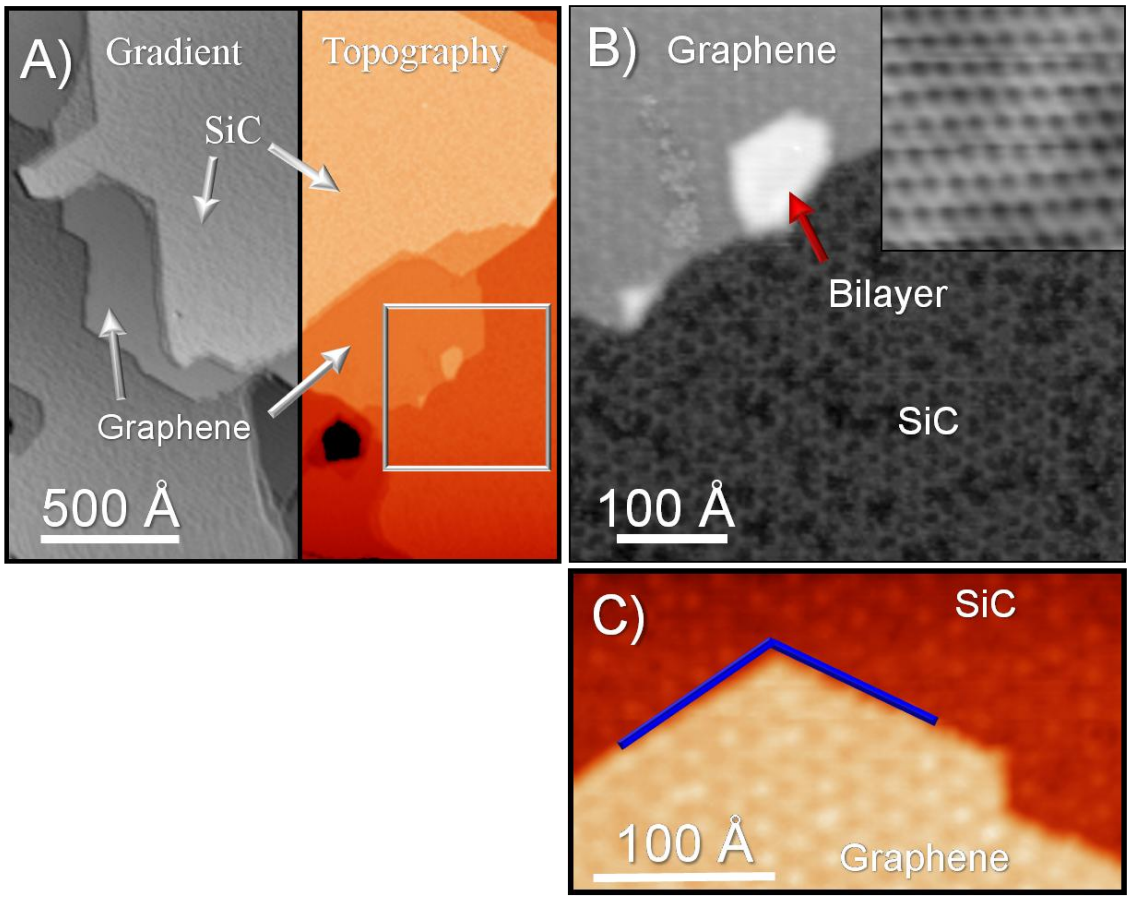

Figure 4.2

RTSTM topographies reveal that some graphene grows from SiC step edges. (A) 0.25 μm x 0.25 μm RTSTM topography shows that areas covered by graphene are smoother as compared to the regions of exposed SiC (tunneling conditions are 1.0 V and 0.1 nA). Using the gradient-enhancement (left side of A) reveals more information on the texture of the surface that is absent from the raw topography data (right side of A). (B) Magnified RTSTM image of the area in (A) highlighted by the white box (tunneling conditions are 0.5 V 0.1 nA). Three different regions are clearly resolved in this image: SiC reconstruction, single-layer graphene, and bilayer graphene. (Inset of B) High resolution image of the single-layer graphene region of (B) clearly resolving the honeycomb lattice. (C) 300 Å x 150 Å RTSTM image of another single-layer graphene to SiC reconstruction step, (tunneling conditions are 2.0 V 0.1 nA). As shown by the blue lines, separated by 120º, the graphene edges follow the directions of the SiC reconstruction.

outline in Fig. 4.1. Inside of this trench there are more etched pits (smaller in size) than above the trench. This suggests that decomposition of the surface, as gauged by the formation of the triangular pits, is enhanced in the trenched region.

A closer look at the sample reveals that only a small percentage of the surface is graphitized, as seen in Fig. 4.2A. The left half of Fig. 4.2A shows a gradient enhanced topography in the scan direction (X direction), while the right side is the colorized raw data. We use the gradient enhancement to help find graphitic regions since the gradient highlights the local texture of the surface more than the raw data.[194] The areas that are visibly smoother are graphene, and the areas that appear corrugated are the SiC reconstruction. Figure 4.2B (a magnified image of the white box in Fig. 4.2A) shows the differences between areas on the surface that are single-layer graphene, bilayer graphene, and the SiC reconstruction. The inset of Fig. 4.2B shows a higher resolution image of the single-layer graphene, clearly resolving the honeycomb lattice structure. Analysis of the regions of Fig 4.2B reveal the single-layer graphene has a corrugation (span of gray scale) ≈ 1 Å over a 100 Å x 100 Å area compared to the SiC reconstruction corrugation ≈ 3.6 Å over a 400 Å x 400 Å area, more than 3 times larger.

Figures 4.2 A & B show that the growth of single-layer and bilayer epitaxial graphene is mediated by step edges. This result is not surprising since the step edge density of the surface is quite large, as evidenced by Fig 4.1. It is interesting to note the step heights between the graphene thicknesses are different than bulk graphite (3.35 Å). The step height from the SiC up to the graphene is typically 2.5 Å ± 0.5 Å, while the step height between single-layer graphene and bilayer graphene is 3.0 Å ± 0.25 Å. Figure 4.2C shows a different region of graphene separated by a step down to the SiC reconstruction. The two blue lines (120º apart) indicate that the graphene step edges follow the protrusions of the SiC reconstruction. The directions of the protrusions are aligned to the hexagonal lattice vectors of the SiC lattice vectors.

4.3 Graphene Island Growth

At particular places on the sample there appear very small (~10 nm wide) islands of graphene. One particular island is shown in Fig. 4.3A. The island locations are found

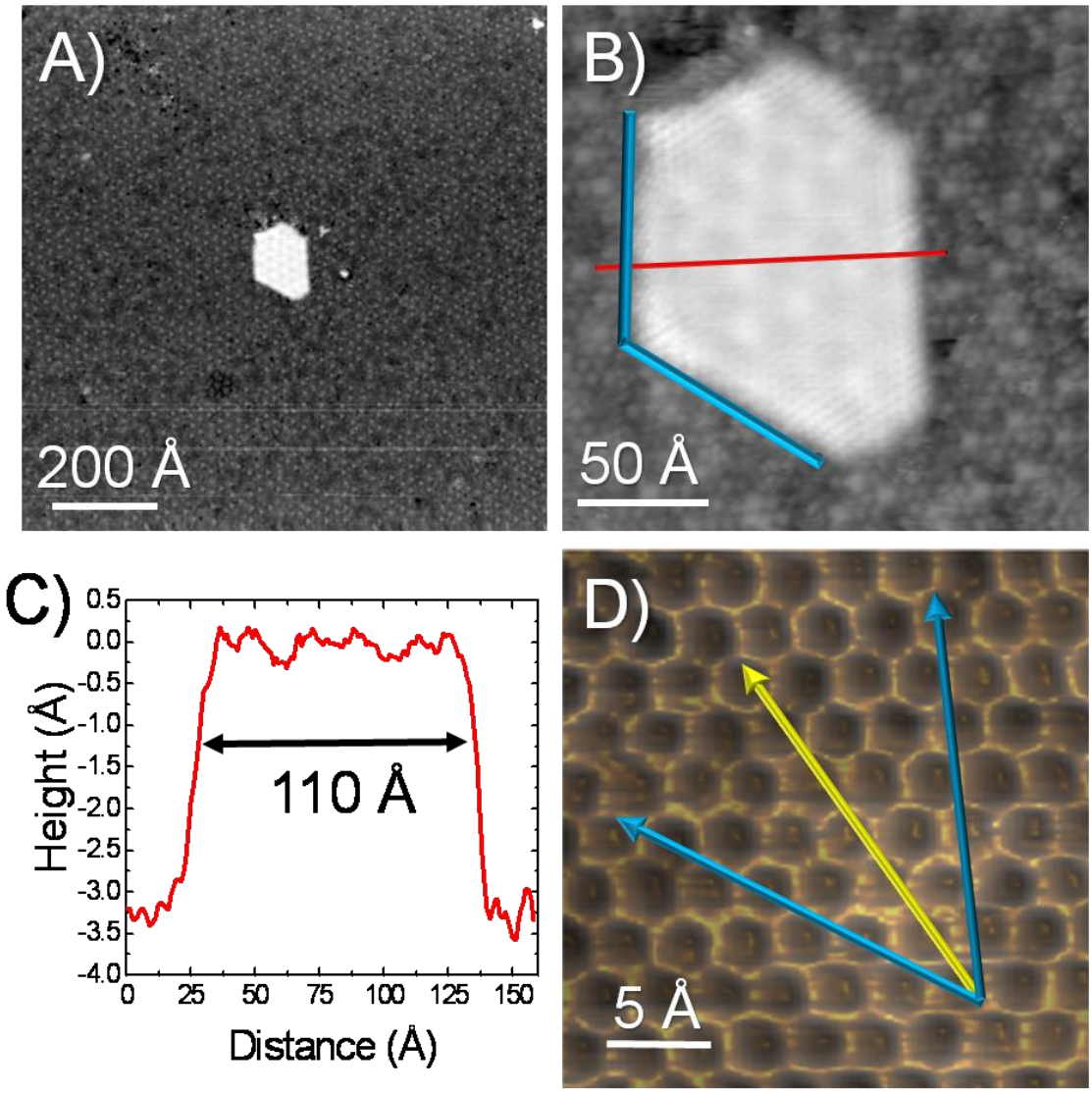

Figure 4.3

RTSTM topographies reveal that graphene forms small nanoscale islands, and that armchair edges are preferred. (A) 1000 Å x 1000 Å RTSTM topography showing a small graphene island (white protrusion) surrounded by SiC reconstruction (tunneling conditions are 0.5 V and 0.1 nA). (B) Higher resolution RTSTM image (200 Å x 200 Å) of the same graphene island (tunneling conditions are 0.5 V and 0.1 nA). This particular island has 6 sides all separated by 120º as shown by the blue lines, again the same directions of the SiC reconstruction. (C) A line profile shows that the island of (B) is about 110 Å wide at the center. (D) Atomic-resolved RTSTM image (25 Å x 25 Å) showing the lattice structure of the island (tunneling conditions are 0.3 V and 0.1 nA). Overlaid on this image are the two lowest energy edge configurations: zigzag (yellow line) or armchair (blue lines). Armchair and zigzag edges are separated by 30º. Since the island has edges 120º apart, the island is solely made up of either zigzag or armchair edges. As one can see the blue lines accurately show the directions of the island edges, meaning the island is entirely made up of armchair edges.

by examining the gradient enhanced topography, similar to what was described above for graphene terraces. Finding the graphene island is quite challenging without a gradient-enhanced topography, since there might only be one island in a 0.5 μm x 0.5 μm area. The infrequency of graphene island formation is again due to the high density of steps on the surface. More graphene islands would form if the step density was reduced via optimizing the graphene growth parameters.[190] It is clear from Fig. 4.3B, the graphene island follows closely the directions of the SiC reconstruction, similar to the graphene terraces near step edges. This is evidenced by overlaying on this image two lines, 120º apart, that show the lattice directions of the SiC lattice vectors. Figure 4.3C shows a line scan across a graphene island. This island is roughly 110 Å wide and has a step height of ≈ 3 Å, the upper limit for graphene/SiC step edges.

Atomic resolution STM images of graphene islands can be used to determine the termination of graphene step edges. This is most easily seen in lines drawn on the lattice structure of Fig. 4.3D, the blue lines correspond to armchair edges of the graphene, while the yellow line corresponds to a zigzag edge. The lines have to be drawn in the middle of the island since there is scattering at the edges (explained more below).[195] Combining the fact that a zigzag edge and an armchair edge are 30º apart and all the edges of our graphene islands are 120º or 60º apart, a graphene island must be entirely surrounded by zigzag or armchair step edges. If one of the edges of the island can be accurately determined, then the entire island will be successfully characterized. By comparing the lines of Fig. 4.3D and the island edges of Fig. 4.3B, one can see that the blue (armchair) lines accurately describe the island. Therefore this graphene island is solely made up of armchair edges.

It is interesting to note that we have found other islands on the surface and they are also comprised of armchair edges. This finding is surprising since one would expect zigzag edges to be preferred, due to this type of edge having fewer broken bonds (0.41 bonds/Å) as compared to armchair edges (0.47 bonds/Å). Recent calculations show that

stability of the edge is determined by the sublattice symmetry of the broken bonds instead of the density.[196] Density function theory (DFT) calculations have concluded that clean graphene armchair edges have a formation energy roughly 1 eV less than zigzag edges.[196] The larger formation energy for zigzag edges arises from high density of states (edge states) near the boundary, compared with absent edge states for an armchair termination.[196] It was also proposed that zigzag edges might even be unstable at room temperature.[196] This work shown in this section highlights the first experimental evidence that epitaxial graphene islands and terraces grow with preferred armchair step edges.

4.4 Spectroscopic Characteristics of Ultrathin Epitaxial Graphene

We have performed STS measurements on the graphene islands and compared the spectra to STS of graphene terraces. The results are summarized in Fig. 4.4. Figure 4.4A shows a large scale gradient-enhanced STM topograph (0.25 μm x 0.25 μm area) with both a single-layer graphene terrace (red arrow) and a graphene island (black square). Figure 4.4B is a magnified STM image of the graphene terrace (red arrow of Fig. 4.4A) showing the graphene lattice structure. The superstructure with period of ≈ 20 Å superimposed on the graphene lattice will be discussed latter in this chapter. Figure 4.4C shows an STM image of an island (black box of Fig. 4.4A) similar in size to the one discussed in Fig. 4.3. This graphene island forms an equilateral triangle (≈ 100 Å on each side with a step height of ≈ 2 Å). The island is again solely made up of armchair edges, 60º apart. The determination of the edge configuration was conducted with the same procedure outlined above for atomic resolution STM images of this island (not shown). Figure 4.4C shows that near the island edges there is significant scattering (blue arrows), which is evidence that graphene is terminated abruptly at this step edge.[160,197] The scattering periodicity masks the atomic configuration of the graphene island edge

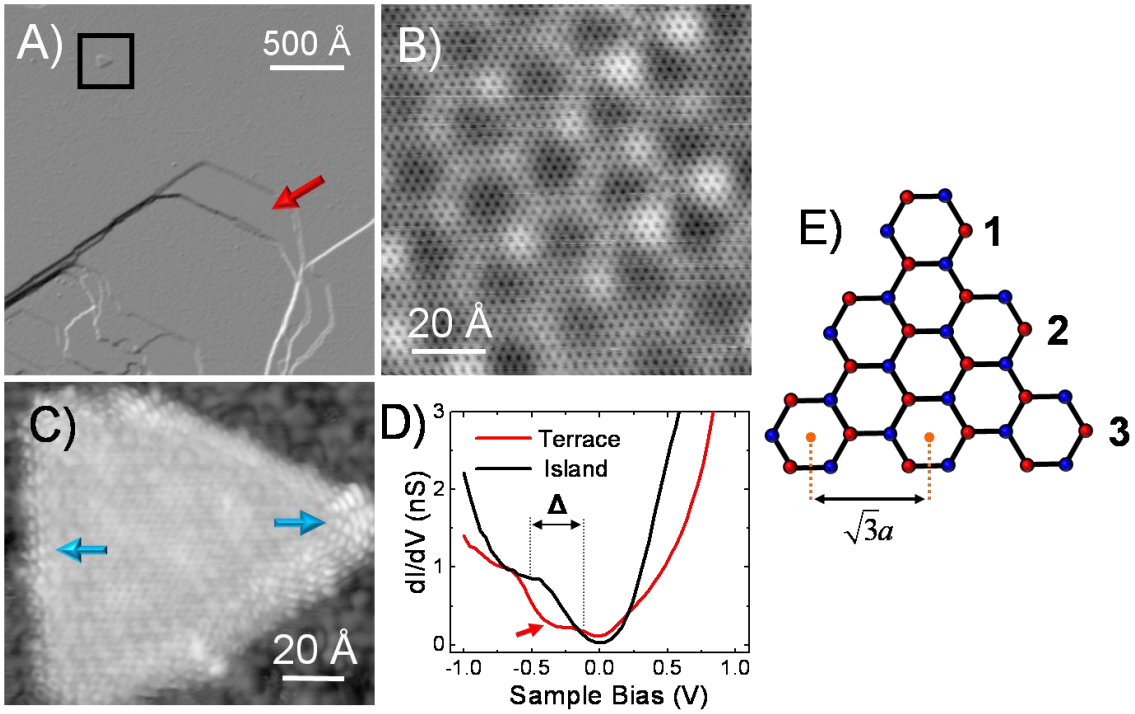

Figure 4.4

RTSTS shows differences between the graphene island and graphene terraces. (A) 0.25 μm x 0.25 μm gradient enhanced RTSTM topography (tunneling conditions are 1.0 V and 0.1 nA) showing a graphene island (black square) and a graphene terrace (red arrow). (B) Atomic resolution (100 Å x 100 Å) RTSTM clearly shows the graphene lattice structure of the terrace seen in A (tunneling conditions are 0.3 V and 0.1 nA). (C) RTSTM topography (100 Å x 87 Å) of the triangular graphene island in A (tunneling conditions are 0.3 V and 0.1 nA). From atomic resolved STM images (not shown), this triangular island is solely made up of armchair edges. (D) Spatially-averaged RTSTS taken from the graphene island of C (black curve) and the graphene terrace of B (red curve). The conditions for the RTSTS are 0.3 V and 0.1 nA. From the plot, it is clear that the LDOS of the graphene island is different than on the graphene terraces. The local minimum observed on the terrace STS (indicated by the red arrow) is believed to be the location of the Dirac point. If there were quantum confinement effects at play in the graphene island, an energy gap over the range of Δ would be present. No such gap feature is seen in the dI/dV over this range. (E) A schematic for a graphene island made up of only armchair edges with three unit cells per side. A procedure for counting the number of carbon atoms in a large island is discussed in the text.

(discussed in more detail in chapter 7). This is the reason why the edge configuration has to be determined from atomic resolution STM images away from the edge.[195]

Figure 4.4D shows spatially-averaged STS taken from the regions of Fig. 4.4C & D. RTSTS taken over the graphene terrace (Fig. 4.4D, red curve) is typical for single-

layer graphene regions. Suppression of the dI/dV near -300 mV, indicated with the red arrow, is believed to be the location of the Dirac point. The shift of the Fermi energy (zero sample bias) with respect to the Dirac point by ≈ 300 meV is understood as charge transfer from the SiC substrate to the graphene.[146,173] A similar suppression in the dI/dV of graphene terraces has been seen by other groups.[198,199] Spatially- averaged RTSTS taken over the graphene island (Fig. 4.4D, black curve) appears very different to the spectrum from the graphene terrace. The STS spectrum taken from the island shows a reduction in dI/dV at the Fermi level as compared to STS the terrace. This result is indicative of the terrace being more metallic than the island. A possible explanation for the difference in spectra might be quantum confinement effects from the small size of the graphene island.

It has been shown both theoretically [200,201] and experimentally[202] that small islands of graphene show evidence of a band gap at the Dirac point due to quantum confinement. Estimates for the band gap of an armchair triangle island with ~10,000 carbon atoms is roughly 0.4 eV, centered at the Dirac point.[203] The number of carbon atoms of an armchair triangle island (N_C) is determined by counting the number of unit cells on one side of a triangle (N) and using the formula, $N_C = 3N(N+1)$. Figure 4.4E shows a graphene armchair island with 3 unit cells per side (36 carbon atoms total) where each unit cell is separated by $\sqrt{3}a$. For the armchair island of Fig. 4.4C with a side length of ≈ 100 Å, I estimate ≈ 23 unit cells per side with the entire island totaling ≈ 1700 carbon atoms. Therefore, we can infer that the band gap of the island (Fig. 4.4C) should be greater than 0.4 eV, assuming the band gap would scale inversely with size of the island. We will use the value of 0.4 eV as the lower bound for the energy gap. In the dI/dV curves over the island, (Fig. 4.4D) Δ shows the range of 0.4 eV centered at the Dirac point ≈ -300mV. Clearly, no evidence of an energy gap is seen in the dI/dV over this range. It even appears that the density of states is higher on the graphene island than

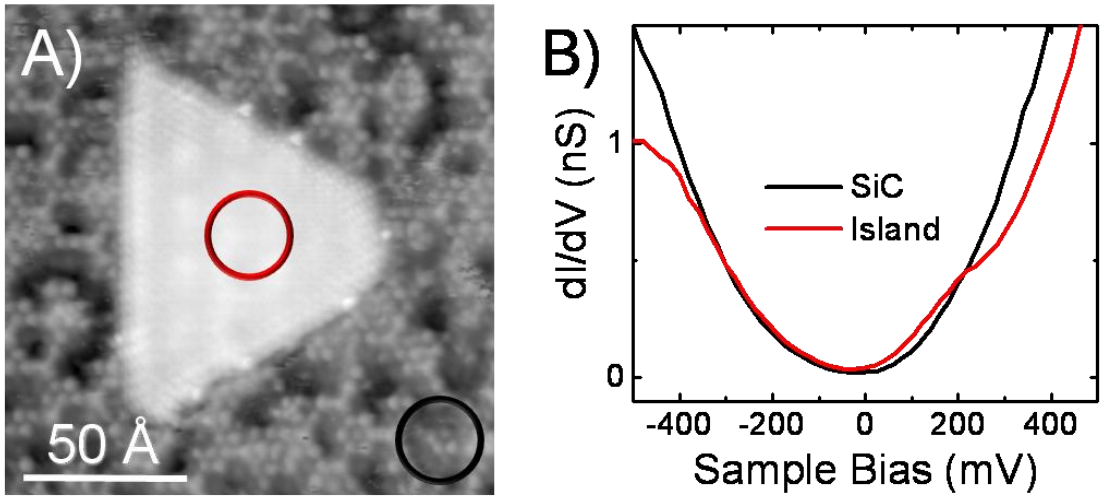

Figure 4.5

Differences in RTSTS between a graphene island and SiC reconstruction. (A) 150 Å x 150 Å RTSTM topography (tunneling conditions are 0.3 V and 0.1 nA) showing another triangular graphene island. This graphene island is again made up armchair edges. (B) Spatially-averaged RTSTS from the center of the graphene island in A (red curve) and SiC reconstruction from the bottom right area of A (black curve). The two spectra are strikingly similar (deviating at high bias). A possible interpretation of the similarities is proposed in the text. The conditions for the RTSTS are 0.3 V and 0.1 nA.

on the graphene terrace over the range of Δ (Fig. 4.4D). This concludes that the graphene island in Fig. 4.4C does not display the quantum confinement characteristics of an isolated graphene island. To understand the nature of the STS on the graphene island (compared to the terrace), the interactions of the graphene island and the SiC substrate need to be considered. Indeed, the tunneling to the SiC interface may dominate the differential conductance measurements, as evidenced in voltage dependent imaging discussed in Chapter 6.

We have performed STS comparing graphene islands and the surrounding SiC reconstruction. Figure 4.5A shows a graphene island that is triangular, roughly 100 Å on a side with a step height of 2 Å. The island, again, is solely made up of armchair edges. A spatially-averaged STS spectrum was taken near the center of the island (red circle) and compared with a spatially-averaged STS spectrum from the SiC reconstruction (black circle) as shown in Fig. 4.5B. As seen from the plot, there are only small differences

between the dI/dV of the SiC reconstruction and the graphene island, deviating only at higher voltages. It is clear from the data, that the density of states of the graphene island more closely resembles the SiC rather the larger graphene terrace. A possible interpretation is that the graphene islands are strongly bound to the SiC substrate, while the graphene terrace is more isolated.

Photoemission spectroscopy studies of the early stages of epitaxial graphene growth show that the SiC reconstruction displays graphitic sp^2-bonding (σ bands), but with no π bands, a signature of graphene.[204,205] This result has been verified by many theoretical studies, which show that the p_z orbitals of the first graphene layer are covalently bonded to the SiC substrate.[206-208] Experiment and theory conclude that even though the first graphene layer might show the graphene lattice structure, it will not display the low energy characteristics of graphene, such as a linear dispersion. In my opinion, this explains the spectroscopic data of the graphene islands from the previous sections. Hydrogen adsorption studies suggest that the edges of epitaxial graphene are strongly bonded to the SiC substrate (elaborated on in Chapter 5). The strongly bound nature of the edges might affect the graphene island more than the graphene terrace, just based on the distance between step edges. This suggests that the graphene islands might not have the necessary area to produce the graphene-like low energy characteristics, where a larger terrace might display such properties.

Even though there are no graphene-like states at low energy for the SiC reconstruction and the graphene island, photoemission studies conclude that surface states are present on the surface at low energy.[205] The surface states, arising from unpassivated dangling bonds, contribute to the low energy density of states where normally there would be an energy band gap.[209] From the plots in Figure 4.5B, it is apparent that the SiC reconstruction and the graphene island have density of states near the Fermi energy that arise from these surface states. Similar surface states are also seen in other semiconductor surface reconstructions.[209] Characterization of the SiC

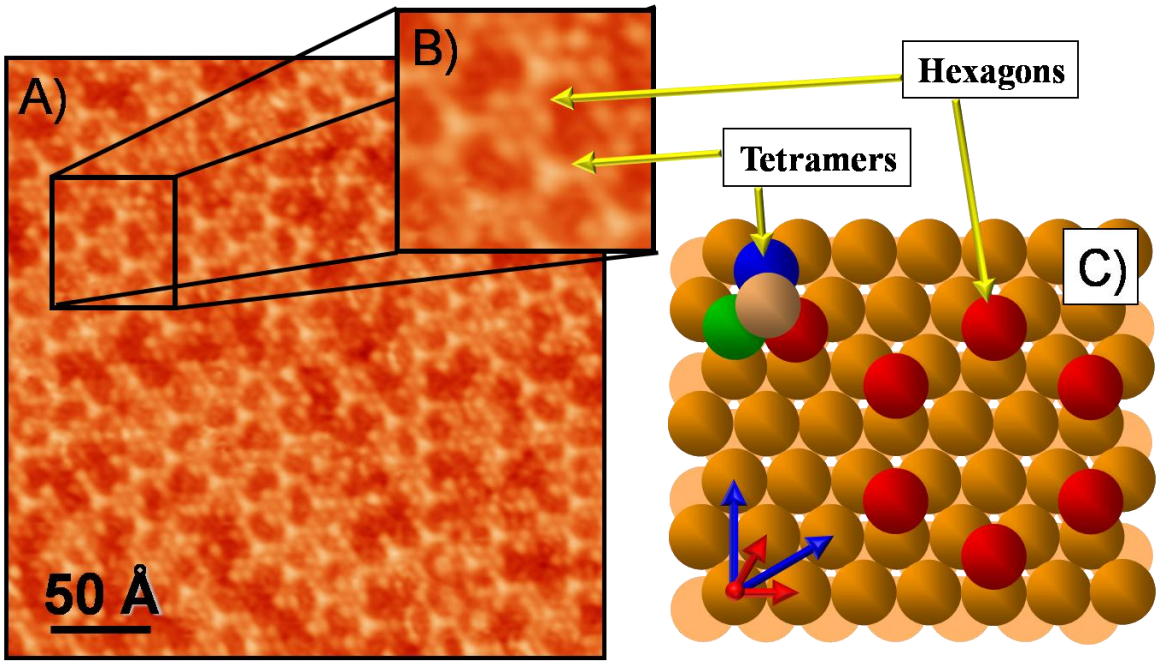

Figure 4.6

RTSTM reveals the morphology of the SiC reconstruction. (A) 300 Å x 300 Å RTSTM image showing the quasi-ordered SiC-6√3 reconstruction (tunneling conditions are 0.5 V and 0.1 nA). (B) Higher resolution RTSTM topography of the boxed region in A. Seen in this image are the two predominate features of the SiC reconstruction, tetramers and hexagon. (C) Schematic geometry of possible Si adatom features consisting of one tetramer and hexagon. The gold atoms represent the Si atoms in the SiC(0001)-1x1 substrate. The tetramers fall on the SiC(0001)-1 x 1 lattice, while the hexagons fall on the SiC(0001)-√3 x √3 lattice.

reconstruction, offering insight into the nature of the dangling bonds, will be discussed in the next section.

4.5 SiC Reconstruction

SiC(0001) forms a couple of stable surface reconstructions before reaching the graphitization temperature. A starting SiC(0001)-1x 1 will form a √3 x √3 R30º reconstruction at around 1000 ºC.[89,93] When the starting 1 x 1 surface is deposited with a few layers of silicon, a 3 x 3 reconstruction is observed after annealing to 800 ºC.[210] Further annealing causes the 3 x 3 to turn into the √3 x √3 R30º.[211] Additional annealing of surface gives rise to a complicated reconstruction with a periodicity of 6√3 x 6√3 R30º

(6√3 hereafter) as well as graphene growth.[89,93] The actual 6√3 structure and composition has been extensively characterized by both experimental[89,93,189,199,205,212-214] and theoretical studies.[206-208,214] In this section, I will discuss the structure of the 6√3 surface, which will offer insight to the origin of the dangling bonds near and underneath the graphene.

Figure 4.6A shows an empty state image with a 400 Å x 400 Å field of view of the 6√3 reconstruction. The magnified region (Fig. 4.6B) shows two predominant features, labeled tetramers and hexagons. Shown in Fig. 4.6C is a possible atomic configuration for these two types of features. In this ball model, the gold atoms show bulk-terminated SiC(0001). However, for clarity only Si atoms are displayed in the model (it is understood that each silicon would be paired with a carbon atom).[185] The 6H-SiC(0001) bulk forms a hexagonal lattice in-plane and the vertical axis is stacked in an ABCACB configuration.[185]

Tetramers appear as pyramidal structures that have three adatoms in registry with the SiC-1 x 1 lattice (red arrows in Fig. 4.6C indicate 1 x 1 lattice vectors), while the fourth adatom rests on top. The tetramers form a quasi-ordered superstructure with periodicity of 6 x 6 with respect to silicon carbide lattice vectors. The tetramers actually give rise to small ripples in the graphene, which is the corrugation measured in the graphene of Fig. 4.2. Similar tetramer type features are known to exist on the Si-rich SiC(0001)-3 x 3reconstruction.[210,213] The STM work of Starke et al. proposed that the 3 x 3 is comprised of tetramer-type features.[210] We feel that the features seen in the 6√3 reconstruction are related to the features of the 3 x 3. Therefore, we assume that the tetramer features of Fig. 4.6 are comprised of silicon. This result is in contradiction to many groups who suspect that at the very high annealing temperatures, silicon adatoms would not remain on the top surface.[189,205] For comparison, the annealing temperature for the 3 x 3 reconstruction is ≈ 800 ºC, while the annealing temperature for this sample was ≈ 1200 ºC. However, further experimental evidence for the 6√3 having Si adatoms has

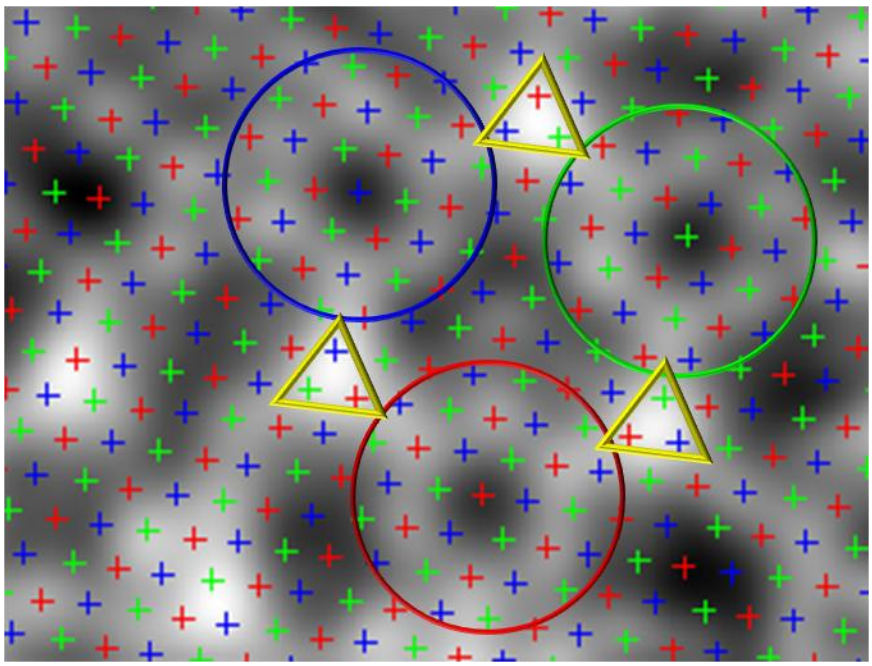

Figure 4.7

High resolution LTSTM image showing the registry of the hexagons of the SiC reconstruction with the different √3 x √3 sublattices (tunneling conditions are 1.0 V and 0.1 nA). Three hexagons are observed to lie on the three different SiC(0001)-√3 x √3 sublattices, denoted by the three different colors. Tetramer features (yellow triangles) are what allow hexagons to switch to different √3 x √3 sublattices. Equal occupation of all three √3 x √3 sublattices helps explain the complicated 6√3 patterns in diffraction studies.

been proposed by our group and others, details will be discussed in the following chapter.[186]

As shown in the structural model of Fig. 4.6C, the hexagons fall on the SiC-√3 x √3R30 lattice with the center adatom missing (blue arrows in Fig. 4.6C indicate √3 x √3R30 lattice vectors). The hexagons closely resemble corner-hole type features of the Si(111)-7 x 7. In both cases the STM images of the hexagons and corner holes resemble adatoms forming a ring with the central adatom missing.[68] The similarity of the hexagons to the silicon-rich corner holes is another piece of evidence that the adatom features on the SiC-6√3 substrate could be comprised of silicon atoms. Figure 4.7, a high resolution image of three hexagons, shows how the hexagons help give rise to the substrate 6√3 periodicity. Overlaid on the image of Fig. 4.7 are the three SiC-√3 x √3R30° sublattices (red, blue, and green crosses), which together occupy all of the SiC

1x1 lattice sites. Color-coded circles show the registry of adjacent hexagonal rings with the underlying sublattices. The reconstruction is not perfectly ordered, but areas such as these where adjacent hexagons fall on different sublattices are typically seen in these samples. This reconstruction structure, comprised of equivalent structures on each of the three SiC-$\sqrt{3} \times \sqrt{3}R30^{o}$ sublattices, explains many features of the $6\sqrt{3}$ pattern observed in LEED measurements.[92]

4.6 Conclusion

In this chapter, I discussed that the prevalent growth mechanism of graphene on SiC is one mediated by SiC bulk step edges. I also showed, under these growth conditions (annealing temperature and time), a small amounts of graphene islands form on the surface with roughly the same size ($\approx$ 100 Å). Different growth graphene parameters will result in different island formation characteristics. It was found that all the edges of the graphene islands and even the graphene terraces prefer an armchair edge configuration. Recent calculations prove that armchair edges require less energy to form as compared to zigzag edges.[196] STS was performed on graphene terraces, graphene islands, and the SiC reconstruction. Comparing the spectra over all three areas revealed a large difference in the STS between the graphene terrace and the island. A slight difference is seen between the island and the SiC reconstruction. The origin of these differences is proposed to arise from the bonding nature of the graphene edges to the SiC. The STS taken over the SiC reconstruction and graphene islands revealed dangling bond states in the SiC band gap, common for semiconductor surface reconstructions. The surface structure, giving rise to the dangling bonds, was proposed from a detailed STM study of the SiC reconstruction. It was found that the reconstruction consists of two different types of adatom features, tetramers and hexagons. Both types of features resemble Si-rich reconstructions on different surfaces, which offers insight into their composition.

CHAPTER 5

ATOMIC HYDROGEN ADSORPTION

Hydrogen has been used extensively in scientific research for many different purposes, including interface state passivation for electronic devices and energy storage for fuel cells. In this chapter, these two processes will be investigated for the case of epitaxial graphene via atomic microscopy. In particular, discussion will focus on the role that hydrogen plays in passivating the dangling bonds of the 6H-SiC(0001)-6√3 reconstruction, which gives insight into the chemical composition. In addition, hydrogen adsorption on single-layer epitaxial graphene and its electronic effect on graphene will also be addressed.

5.1 Hydrogen Passivation

In the modern computer industry, metal–oxide–semiconductor field-effect transistor (MOSFET) devices based on silicon are preferred over other materials, such as GaAs and other III-V semiconductors. The main reason rests in the fact that silicon grows a native gate oxide (SiO_2) with a low interfacial defect density.[215] However, unbonded Si defects do exist at the silicon-oxide boundary, yielding unsatisfied dangling bonds (otherwise known as charge traps) with large localized density of states.[216] A large amount of charge traps can be detrimental to the performance of any MOSFET device.[217] Due to its small size, atomic hydrogen can diffuse through metallic and oxide layers of a MOSFET device to satisfy the dangling bonds at the Si/SiO_2 interface.[218-220] Passivation of these charge traps has been shown to increase drain current flow in a MOSFET device by up to 400%.[221]

It is clear that atomic hydrogen plays a vital role (sometimes good or bad) in the processing of MOSFET devices.[222] A large scientific effort has focused understanding the advantages and disadvantages of having excess hydrogen at the interface of a

MOSFET.[223] Despite satisfying dangling Si-bonds, excess hydrogen at the Si-SiO_2 interface can also decrease the performance of the device in many ways, one in particular is from hot electron degradation.[127] Recently, it was found that deuterium (heavy hydrogen) solves many problems that exist when using hydrogen to passivate the Si-dangling bonds.[215,224]

In this work, we have investigated whether the possibility exists that interface state passivation would improve the performance of epitaxial graphene devices, similar to MOSFET devices. Considering potential diffusion paths of hydrogen either through the graphene or under a graphene edge, we chose a sample with a low coverage of graphene, identical to the sample characterized in the previous chapter. As it turns out, we were unsuccessful in passivating the dangling bonds underneath the graphene. We believe that there is a strong chemical bond between the graphene and the substrate at the edges of the graphene regions. Effectively, the edges of the graphene are sealed shut from any adsorbate, including hydrogen. This type of sealing behavior has been observed for other gases (such as helium and argon) in exfoliated graphene flakes over SiO_2 wells. [225] In spite of this negative result, we were able to unearth some novel hydrogen adsorption properties about the graphene/SiC system.

Under normal conditions, hydrogen is a nonreactive, diatomic gas. To utilize hydrogen for dangling bond passivation, the hydrogen molecule has to be cracked to form atomic hydrogen. To crack the hydrogen, we installed in our UHV chamber a coiled tungsten filament (similar to one found in a modern light bulb). The filament was mounted on a high current UHV feedthrough and positioned about 3" away from the sample. Diatomic hydrogen in the vicinity of a hot filament has been shown to crack into atomic hydrogen.[226] After being cracked, the atomic hydrogen is extremely reactive so the proximity of the filament to the sample is very important.

To start the hydrogen passivation process, the sample was first annealed to an elevated temperature to prevent etching from the incident atomic hydrogen. Later in this

section I will address how sample temperature changes surface passivation. The range of sample temperatures was between 200 °C to 800 °C. When the sample is stable at the desired temperature, molecular hydrogen is backfilled into the chamber at a pressure of 5 x 10^{-6} Torr. The next step is to pass enough current through the tungsten filament to cause the temperature to reach 1400 º C, measured with an optical pyrometer. The filament is at the elevated temperature for 10 minutes, which results in a hydrogen dose of 3000 Langmuir (1 Langmuir = 10^{-6} Torr-sec). After the desired dose of hydrogen, three steps remain: the filament is turned off first, then the UHV chamber is pumped back down to base pressure, and the sample is cooled to room temperature. For consistency, room temperature-STM measurements are performed on both pre- and post-hydrogen dosed surfaces. Unfortunately, since the sample has to be removed from the microscope at each hydrogen dose cycle, it is virtually impossible to show STM images of the same region before and after a hydrogen dose.

Discussion of Chapter 4 described how the dangling bonds of the 6√3 introduce localized states in the large bulk band gap of 6H-SiC(0001), which is in agreement with ARPES measurements.[205] The incorporation of atomic hydrogen into the SiC reconstruction is clearly observed in our RTSTM measurements. Regions of 6√3 SiC that have been successfully passivated image differently than STM images of virgin 6√3 SiC (Fig. 4.6A of last chapter). The effect of hydrogen is clearly seen in Fig. 5.1A, where the once quasi-ordered 6√3 now looks amorphous and disordered. Figure 5.1B displays STS measurements taken over 6√3 regions before and after hydrogen dosing. A spectrum performed over single-layer graphene is also included for comparison. The introduction of atomic hydrogen has satisfied the dangling bonds of the 6√3, causing a removal of the localized states around the dangling bonds. This quenching allows for the reemergence of a large energy band gap, which is readily seen in Fig. 5.1B. Before the hydrogen dose, there was just a small gap in dI/dV of the 6√3, which is hard to resolved

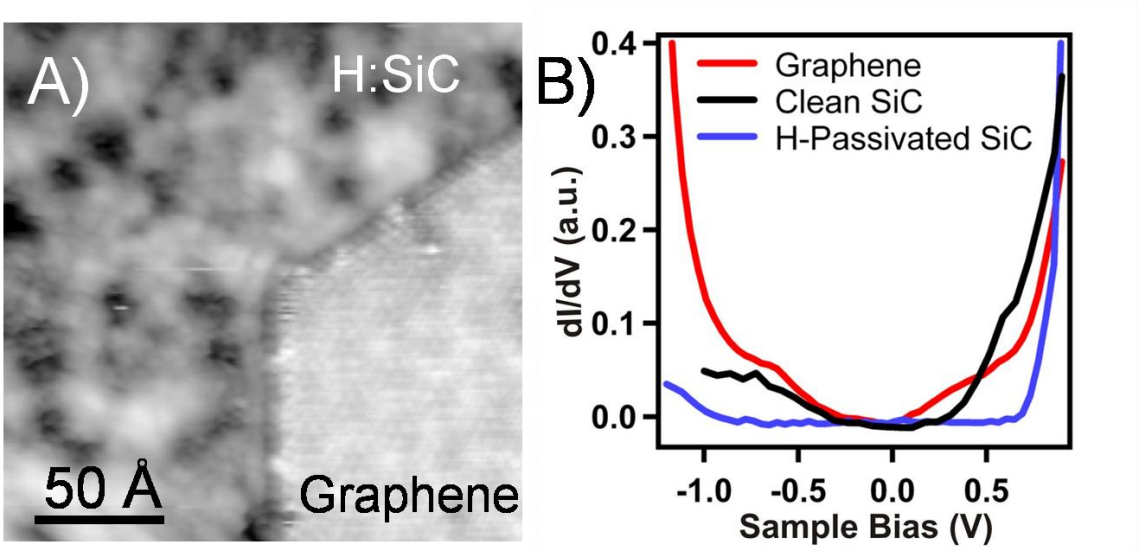

Figure 5.1

Hydrogen is used to successfully passivate the dangling bonds of the SiC reconstruction (A) RTSTM (200 Å x 200 Å) image of the surface following exposure to hydrogen (tunneling conditions are 2.0 V and 0.1 nA). This image clearly shows that the once quasi-order SiC-6√3 now looks amorphous and disordered. The SiC-6√3 underneath the graphene appears unchanged by the hydrogen exposure. (B) RTSTS measured over the H-SiC regions and graphene regions of A (spectra servo conditions are 1V and 0.1 nA). RTSTS from clean SiC before hydrogen exposure is shown for reference. The hydrogen exposure causes a large energy gap (≈ 1.5 V) to open up in the LDOS over regions of H-SiC. We believe this gap arises from the successful passivation of the SiC-6√3 dangling bonds.

at room temperature.[214] STS spectra performed on graphene terraces have more of a metallic appearance, with no signs of a band gap. The STS spectra of bare-graphene regions after the hydrogen dose (not shown) are effectively unchanged by the hydrogen dosing.

From a detailed study of the passivation characteristics vs. temperature, we have gained insight into the chemical composition of the 6√3. We have preformed hydrogen dosing measurements at four different sample temperatures to see the thermal effects on the incorporation of the atomic hydrogen into the 6√3. This series of measurements is summarized in the Figs. 5.2A-D. In all four images of Fig. 5.2, the upper terrace is a single layer of graphene and lower is the 6√3 reconstruction. In the

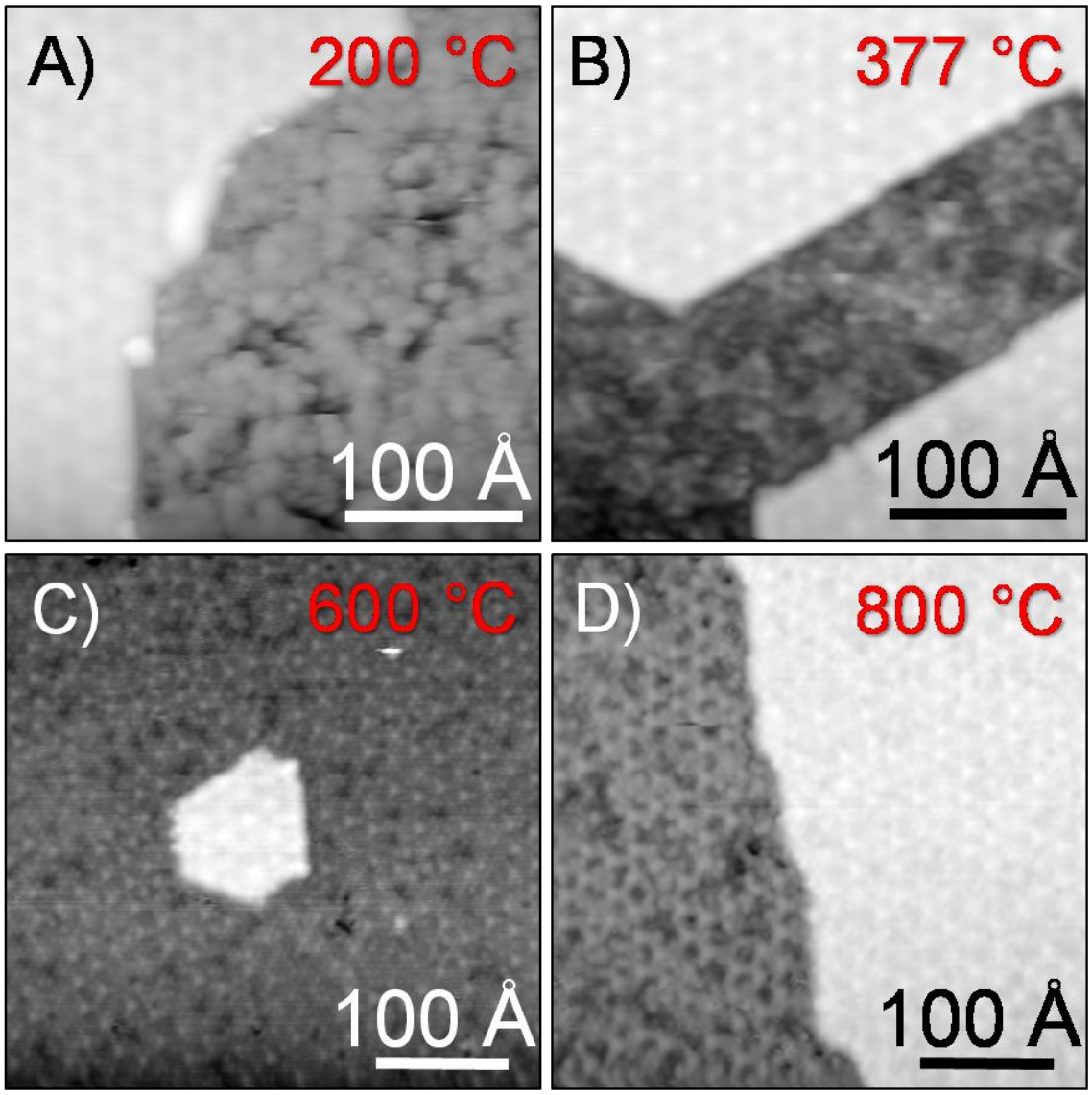

Figure 5.2

Temperature dependence of the hydrogen passivation. We performed the hydrogen exposure at four different sample temperatures: (A) 200 °C, (B) 377 °C, (C) 600 °C, and (D) 800 °C. RTSTM images (held at a fixed tunneling current of 0.1 nA) were performed with conditions: (A & B) 300 Å x 300 Å at -2.5 V and 2.0 V, respectively, (C & D) 400 Å x 400 Å at 1 V. SiC regions (lower regions in A & B) appear passivated for temperatures below 600 °C. At temperatures above 600 °C, the SiC (lower regions in C & D) appears quasi-ordered once again. This temperature dependence offers insight into the chemical composition of the SiC-6√3, and suggests that the dangling bonds originate from silicon atoms.

previous section, the passivation was conducted at a sample temperature of 377 ºC (Figs. 5.1 and 5.2B). This temperature is known to effectively passivate the Si dangling bonds of a Si(100) surface.[227] In our measurements it appears that the passivation is only successful when the sample temperature is less than ~ 400 ºC (Figs. 5.2 A & B). This is seen in the disordered and amorphous STM images of the 6√3 at sample temperatures of 200 ºC and 377 ºC (Figs. 5.2 A & B). At temperatures of 600 ºC and 800 ºC (Figs. 5.2 C & D), the 6√3 looks well ordered, similar to images of the virgin 6√3. It is clear from all four STM images of Fig. 5.2 that the interface structure below the graphene layer is unchanged. Therefore, we can conclude that the hydrogen is not penetrating under the edges or diffusing through the epitaxial graphene.

The temperature threshold of when the hydrogen no longer satisfies the 6√3 dangling bonds gives some insight into the chemical composition of the reconstruction. From previous studies by other groups, who have attempted to passivate the surfaces of Si(100) and diamond or C(100), a temperature dependence for the hydrogen adhering to the substrate was shown. For the silicon-rich surfaces [Si(100)] the passivation temperature was ≈ 400 ºC.[226,228] At temperatures larger than 400 ºC the silicon-hydrogen bond is easily broken. In stark contrast, it was found that the passivation for the carbon-rich surfaces [C(100)] was more robust, since the carbon-hydrogen bond would not break until the sample temperature was ≈ 800 ºC.[229] Figure 5.2 clearly shows that by 600 ºC in our experiment the atomic hydrogen was no longer bonding to the 6√3 reconstruction. Therefore, we can effectively rule out carbon as the origin of the 6√3 dangling bonds. Recently, X-ray reflectivity measurements performed on similar Si-face graphitized samples have suggested that the top layer of the 6√3 substrate reconstruction might be comprised of silicon atoms.[230] This study also suggests that the sequential layers supporting the top layer of silicon adatoms might very well be carbon rich. Our work is the first definitive evidence via local atomic scale measurements that the SiC reconstruction is comprised in part of silicon atoms.

5.2 Adsorption of Hydrogen to Single-Layer Graphene

Hydrogen, packaged in the form of fuel cells, has been proposed as a source for the world's future supply of energy.[231] This could be the long awaited eco-friendly energy source that will replace carbon-based fossil fuels, such as coal and petroleum. The industry appeal of hydrogen rests in its ability as an extremely efficient source of energy, which is related to its chemical mass (the amount of dispensable energy per mass).[232] The chemical mass of hydrogen is roughly three times larger than that of petroleum-based fuels. Therefore, the operation of an automobile powered by hydrogen will result in a reduction of the fuel mass by 66%. Moreover, hydrogen is the most abundant element on the planet and when hydrogen is burnt in an oxygen environment the byproduct is water, as opposed to harmful green house gases.[233] All these characteristics make hydrogen a viable solution to the world's energy troubles.

Problems do arise with the potential use of hydrogen as an energy source.[233] In particular, a problem arises that involves the issue of hydrogen storage, which I plan to address in this work. Even though less weight is needed to run a hydrogen car, a gaseous hydrogen source would take up a larger volume compared to a standard gasoline tank. One solution arises with the condensation of hydrogen on large surface area materials, which will greatly reduce the volume. Ironically, the material that hydrogen might replace as a fuel source, carbon, is one promising candidate to store hydrogen for fuel cells. Recently, there has been a large scientific effort in the research of hydrogen storage in carbon-based materials.[234] Most studies have focused on the adsorption of hydrogen to either graphite nanofibers[235] or carbon nanotubes bundles.[236,237] Where the adsorption process of hydrogen to carbon nanotubes is mostly likely a chemisorption process, instead of a physisorption.[238] Increased hydrogen absorption can be observed in these carbon systems through the doping of alkali metals such as lithium.[239]

Calculations suggest that the curvature of carbon nanotubes heightens the adsorption characteristics of hydrogen over a planar surface such as graphene.[240,241]

However, to study the chemisorption process of hydrogen to carbon nanotubes, graphene offers a useful test bed for useful calculations and experiments. The effect of hydrogen bonding to single-layer graphene has been studied theoretically (due to the recent press that graphene has received), but experimental investigations such as STM studies have been lacking. Hydrogen and deuterium adsorption studies characterized with STM have been performed on bulk graphite, and insight can be gathered from these experiments.[242-244] In this work, we offer a preliminary study of the properties of hydrogen chemisorption to single-layer graphene with atomic-resolved STM.

We have observed in our STM images that after hydrogen dosing a very low coverage of hydrogen adheres to single-layer graphene regions. These are the same dosing parameters that essentially saturate the SiC reconstruction with hydrogen. From our STM images it is clear that the hydrogen adsorbed to the graphene causes a change in the electronic structure of the graphene. Figures 5.3 A & B shows two images of the same area taken at two different bias voltages. Figure 5.3A, taken at -1.5 V, illustrates where the hydrogen is absorbed, highlighted by the red circles. However, when the bias is lowered to -1 V (shown in Fig. 5.3B), there are regions of the image with different contrast. The yellow outline shows the boundary between light and dark regions. The dark regions are close to the adsorbed hydrogen and the light regions are far away. This bias dependence offers insight into the effect hydrogen has on the single-layer graphene.

The electronic perturbation of hydrogen on single-layer graphene has been investigated by many theoretical studies. It has been suggested that chemisorbed hydrogen will change the bonding configuration of the graphene from a sp^2-bonding configuration to a diamond-like sp^3-bonding character. This would result in the absence of the low energy π-electron states, and the opening of a substantial energy bandgap.[245] Additional properties of hydrogen adsorption to graphene rest on the specific bonding configuration of the hydrogen to the carbon atoms.

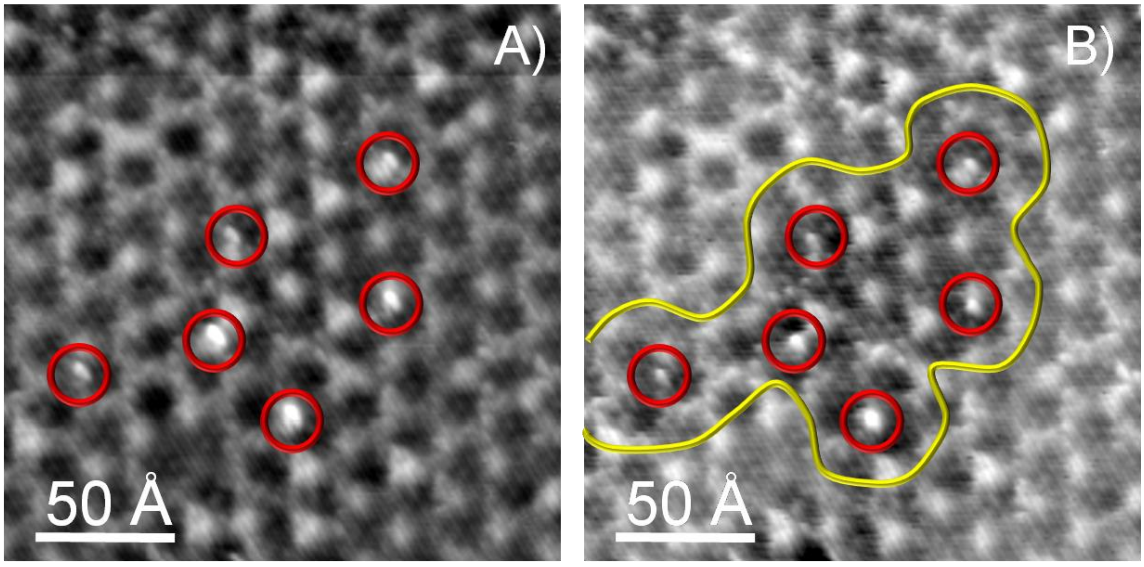

Figure 5.3

Hydrogen adsorption to single-layer graphene (A) RTSTM image (200 Å x 200 Å) of six different hydrogen pairs highlighted with red circles (tunneling conditions are -1.5 V and 0.1 nA). The bright contrast of the hydrogen might arise from either a structural height difference or a charging of the hydrogen. (B) The same area imaged at different tunneling conditions (-1.0 V and 0.1 nA) reveals a dramatic LDOS change in the area around adsorbed hydrogen dimers (highlighted with a yellow outline). This indicates that the hydrogen changes the electronic structure of the single-layer graphene.

As it turns out, hydrogen prefers to chemisorb to graphene (and graphite) in the form of molecular hydrogen dimers.[245] Although energetically unfavorable, many theoretical studies have suggested that atomic hydrogen bonded to graphene could result in spontaneous ferromagnetism, which arises from the breaking of the sublattice symmetry of graphene.[246,247] Similar magnetism (arising from vacancies instead of hydrogen adsorption) has been observed experimentally in proton-irritated graphite.[248] However, to achieve the lowest energy state, hydrogen dimers adhere to the graphene on different carbon sublattices (preserving the sublattice symmetry).[245] This is shown systematically in Fig. 5.4A, where there are only two configurations, either hydrogen bonded across a honeycomb ring (type i) or bonded to nearest neighbors (type ii). To determine the bonding configuration of the hydrogen dimer, atomic resolution STM images are required. Figure 5.4B is an STM image showing the two separate lobes of

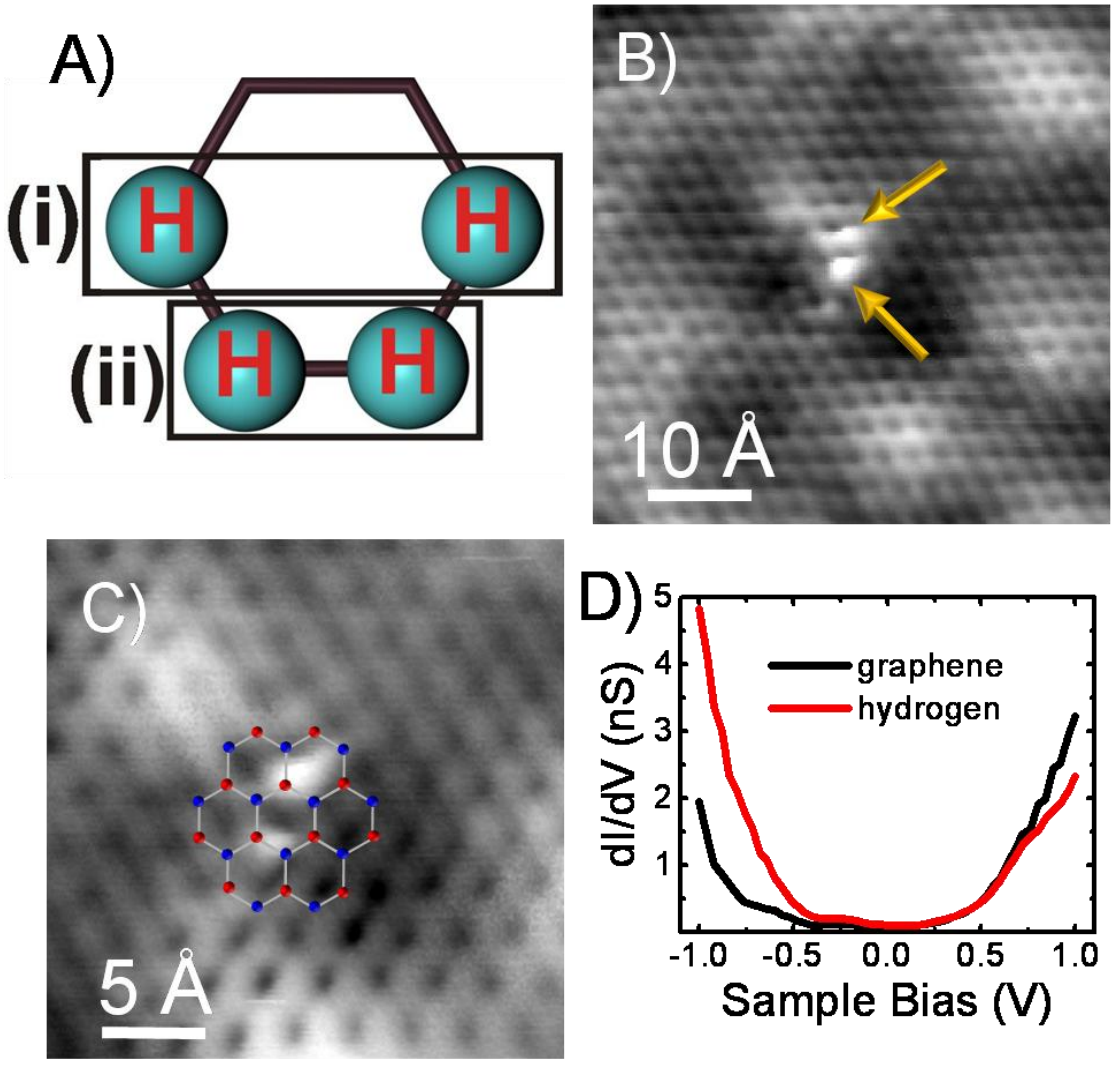

Figure 5.4

Hydrogen dimer formation on graphene. (A) Schematic drawing of the two most favorable adsorption sites for hydrogen dimers on graphene. The hydrogen dimers can form across a graphene honeycomb (i) or nearest neighbor sites (ii). (B) RTSTM (50 Å x 50 Å) image showing a hydrogen dimer (tunneling conditions are 1 V and 0.1 nA), yellow arrows indicate the two distinct lobes of the hydrogen dimer. (C) High resolution RTSTM image (25 Å x 25 Å) indicate that this hydrogen dimer is of the type I variety. The graphene lattice is included to help determine the bonding configuration (tunneling conditions are 0.5 V and 0.1 nA). (D) Single-STS spectrum performed on the top hydrogen atom of the dimer in C and compared with spectrum performed on bare graphene roughly 1 nm away from the dimer (spectra conditions are 0.5 V and 0.1 nA). It is clear from the plot that the dI/dV over the hydrogen atom has a larger LDOS as compared to the bare-graphene at higher negative energy, which is consistent with the contrast change of the STM images of Fig. 5.3.

the hydrogen dimers, highlighted by the yellow arrows. A higher resolution STM image of the hydrogen dimer (Fig. 5.4C) can actually reveal the bonding configuration. From a careful analysis, it is concluded that this hydrogen dimer is type i, where the bonding configuration is across a graphene unit cell. A ideal graphene lattice is drawn over the hydrogen dimer for clarity, but this might be misleading since there is considerable lattice deformation when the hydrogen chemisorbs to the graphene.[245] This relates to the hydrogen changing the graphene sp^2-bond to a sp^3-bond, as mentioned above.

To give more information about the electronic structure of the hydrogen bonding, we have performed STS spectra on the hydrogen dimer and compared the results to spectra taken over the bare graphene. This is illustrated in Fig. 5.4 D, where the red curve was a single spectrum performed on the top hydrogen of the dimer in Fig. 5.4 C and the black curve was a single spectrum taken over bare graphene roughly 1 nm away from the hydrogen dimer. It is clear from the plot that at large negative bias the LDOS over the hydrogen is enhanced compared to over the bare graphene. This result is in contrast to the theoretically-predicted band gap from the sp^3-bonding of the hydrogen. This dI/dV plot is more suggestive that the hydrogen dimer is absorbing charge from the surrounding environment, making the hydrogen an acceptor. This would help explain why the hydrogen dimer appears bright only at high negative bias along with a charge density reduction around the adsorption site.

5.3 Conclusion

In this chapter, I have discussed the passivated of the bare SiC reconstruction with atomic hydrogen. The passivation causes a quenching of the localized states from the reconstruction's dangling bonds. The quenching of the localized states results in the emergence of a large gap in the STS spectra, roughly 1.5 eV wide. I showed that the temperature at which the sample was held during hydrogen dosing was important for a successful passivation. It was found that temperatures in the excess of 600 ºC resulted in

unpassivated SiC dangling bonds, ruling out the top region of the reconstruction being comprised of carbon. Finally, I discussed hydrogen dimer formation on top of single-layer epitaxial graphene. The structural configuration of the hydrogen dimer was found to be similar to what had been proposed for hydrogen adsorption on graphite. This work highlights the first successful adsorption of hydrogen to single-layer graphene. We also showed that the hydrogen locally dopes the graphene with holes, with depressions clearly seen in filled state images around hydrogen adsorption sites.

CHAPTER 6

EPITAXIAL GRAPHENE STUDIED WITH LTSTM

Previous chapters have discussed the characteristics of single-layer epitaxial graphene and the SiC reconstruction probed with room-temperature STM. In the remaining two chapters of this thesis, I will discuss results from our investigations of epitaxial graphene with a low temperature STM operated at 4.2 K. A detailed description of the apparatus was given in Chapter 2. Moreover, Chapter 2 outlined the advantages of performing STM measurements at low temperatures. One of the main advantages is the heightened energy resolution of spectroscopic data as compared to room temperature measurements. Using this heighted energy resolution, this chapter offers an in-depth study of novel properties from single-layer epitaxial graphene, graphene/SiC interface, and bilayer epitaxial graphene. In particular, I will address the STM imaging and spectroscopic characteristics of the graphene/SiC interface and how these relate to the electronic properties of single-layer epitaxial graphene. In addition, I will discuss the morphology of epitaxial graphene bilayers on the Si-terminated SiC. Finally, I will describe a unique way to determine the interlayer coupling that arises from the stacking sequence of bilayer epitaxial graphene.

Contents of this chapter have been discussed in the following publications:

G. M. Rutter *et al.,* "Imaging the interface of epitaxial graphene with silicon carbide via scanning tunneling microscopy." *Phys. Rev. B* **76**, 235416 (2007).

G. M. Rutter *et al.,* "Structural and electronic properties of bilayer epitaxial graphene." *Journal of Vacuum Science & Technology A* **26**, 938 (2008).

6.1 Imaging Characteristics of Single-layer Epitaxial Graphene

What seems to be a unique feature of epitaxial graphene, we have found that simple STM topographic images display a wealth of structural and electronic information pertaining to both the single-layer epitaxial graphene and the interface. In particular, the first layer of epitaxial graphene appears to become "transparent" in our STM images when the applied bias is far from the Fermi level, this result has been verified by other groups.[189,194,198,199] The imaging behavior is evidenced in the STM topography of Fig. 6.1A. In the topography there appear many adatom-type features that might be misconstrued as being on top of the epitaxial graphene surface. Imaged alongside the adatom features is the graphene honeycomb structure, which is shown explicitly in Fig. 6.1B.

Under close inspection it is found that the adatom features resemble the components of the SiC reconstruction, introduced in Chapter 4. It appears that both components of the SiC reconstruction, tetramers (Fig. 6.1C) and hexagons (Fig. 6.1D), are present in the image. Atomic configuration of the tetramer in Fig. 6.1C is highlighted by three red spheres (bottom orbitals) and one blue sphere (top orbital). Typically, orbital features are found surrounding tetramers that fall on one of the SiC $\sqrt{3}$ sublattices (yellow spheres). Atomic configuration of the hexagon in Fig. 6.2 D is highlighted by 6 yellow spheres, which indicates the hexagon also falls on a SiC $\sqrt{3}$ sublattice. From the above observations we can conclude that these features do arise from orbitals of the reconstructed SiC substrate, which remarkably contribute strongly to the local density of states even above the graphene layer, roughly 2.5 Å away.

It is interesting to note that STM topographic measurements performed on exfoliated graphene over a SiO_2 substrate do not display any similar interfacial features.[249,250] This lack of interface transmission arises directly from the insulating and amorphous nature of the SiO_2 (band gap of roughly 9 eV), which does not allow for the tunneling of electrons in the typical voltage range of STM operation. However,

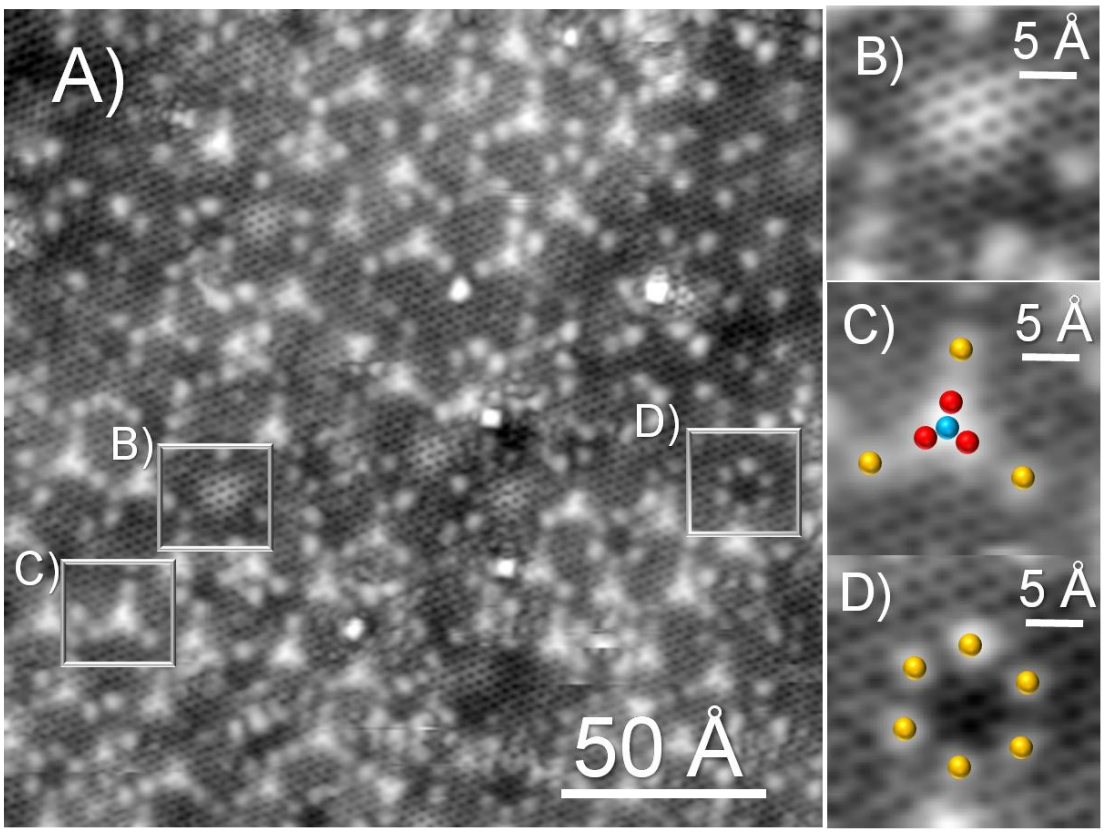

Figure 6.1

(A) LTSTM topographic image (200 Å x 200 Å) of the first layer of epitaxial graphene (tunneling conditions are 400 mV and 50 pA). The image shows a combination of SiC interface features along with the graphene lattice due to the transparency of the graphene. Parts B-D show magnified views of the image of A. (B) The honeycomb graphene lattice structure is clearly imaged surrounded by SiC interface features. The interface features can be put into one of two categories either tetramers or hexagons. (C) Tetramer feature is highlighted by three red spheres (bottoms orbitals) and one blue sphere (top orbital). Typically, orbitals that surround tetramers fall on the SiC $\sqrt{3}$ sublattice (yellow spheres). (D) Hexagon feature is highlighted by six yellow spheres to indicate that it also falls on a SiC $\sqrt{3}$ sublattice. Both of these features were introduced in Chapter 4 as part of the SiC substrate reconstruction.

interfacial SiO_2 disorder in these exfoliated graphene samples does result in one of the major limitations of the carrier mobility.[113] It seems that STM will not be able to investigate why the disorder plays such a critical role in exfoliated graphene devices. On the other hand, even though the SiC surface at low temperatures should have a very similar insulating behavior, we still observe the dangling bonds localized around the interfacial reconstruction. This offers us a unique opportunity to investigate the

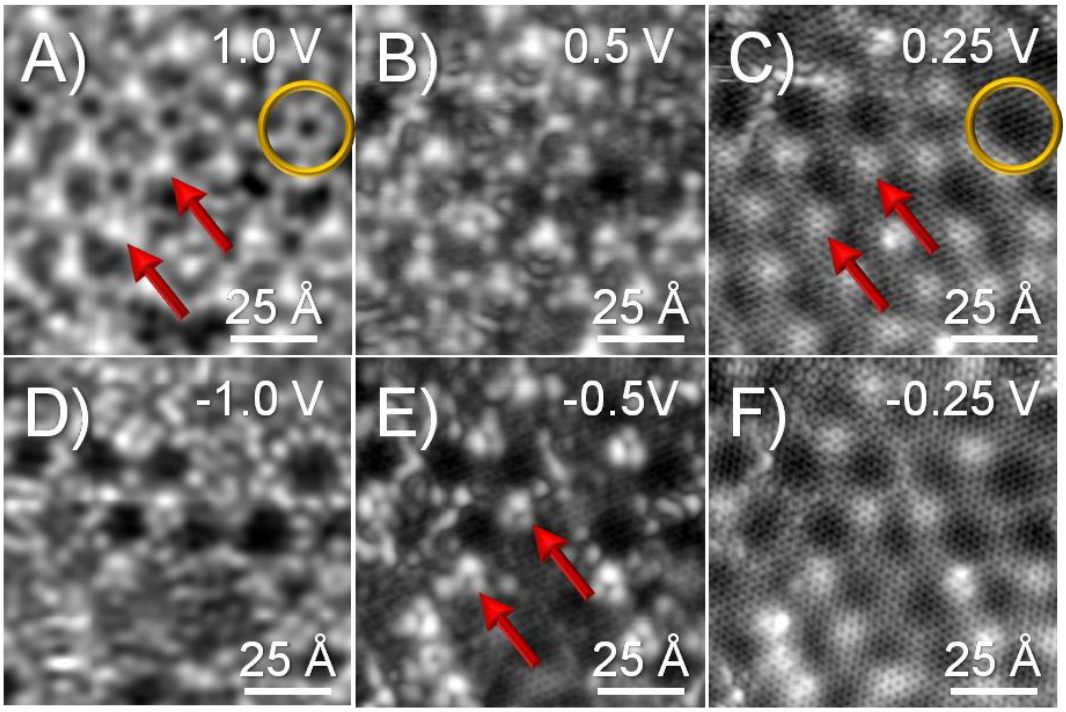

Figure 6.2

Bias-dependent LTSTM topographic images show the progression from imaging the SiC interface structure at high bias to imaging the graphene overlayer at low bias. The tunneling current is fixed at 100 pA, and the bias voltages are (A) 1.0 V, (B) 0.5 V, (C) 0.25 V, (D) -1.0 V, (E) -0.5 V, and (F) -0.25 V. Red arrows indicate that different features (tetramers in A and trimers in E) are imaged at the same surface location, dependent on bias voltage. In addition, we have found that the interfacial reconstruction influences the morphology of the graphene. Tetramers locations (red arrows) correspond to protrusions in the graphene, while hexagons locations (yellow circle) correspond to depressions in the graphene.

interfacial structure underneath graphene using atomic microscopy at low temperature. In what follows, I will offer further discussion about the transparency of the single-layer epitaxial graphene using the techniques of bias-dependent STM topographic imaging and density-functional theory (DFT) calculations.

A series of bias-dependent STM images offers some insight into how the interfacial region contributes to the morphology of the epitaxial graphene. STM images of the first graphene layer obtained at different tunneling biases (Fig. 6.2) show that the transparency of the first layer is dependent on the energy of the tunneling electrons. Interfacial features dominate the STM images for both the unoccupied states (Fig. 6.2A)

and occupied states (Fig. 6.2D). The presence of the interface in these images is so pronounced that the graphene does not appear in the field of view. From the empty-state image at +1 V (Fig. 6.2A), we can identify the two predominant features of the SiC reconstruction: tetramers (a couple indicated with red arrows) and hexagons (one indicated with a yellow circle). At high voltage the tetramers appear as one circular object, but at lower tunneling bias the three bottom orbitals of the tetramer become visible (Figs. 6.1 and 6.2B). Filled state imaging (Fig. 6.2 E) at tetramer locations reveals a different feature with only three lobes, we refer to these features as trimers (red arrows in Fig. 6.2E). From a careful analysis of the location of these lobes, it is found that they also fall on the SiC $\sqrt{3}$ lattice. The configuration of the trimers is essentially the antibonding orbitals of the tetramers. We feel that the tetramers are more characteristic of the actual atomic structure at these locations.

From the bias dependence of the STM images, it is apparent that the tetramers and hexagons play a key role in the surface morphology of the graphene. Figures 6.2 A & C show that there is a direct correspondence between the tetramer features and maxima in the graphene dominated images. Highlighted by the red arrows of Figs. 6.2 A & C, we find that at locations of a tetramer in the interface reconstruction, there will be a protrusion in the graphene. Therefore, we propose that the tetramers cause a structural rippling by acting as tent posts to support the flexible graphene layer. Between the tetramers locations, the hexagons of the interface reconstruction (yellow circle of Figs. 6.2 A & C) yield depressions in graphene layer. The combination of the tetramers and hexagons equates to a structural modulation of a 6 x 6 periodicity (referenced to the SiC lattice vectors) in the epitaxial graphene that has an experimental corrugation of ≈ 1 Å. This indicates that the 6 x 6 periodicity observed in the graphene layers grown on SiC is most likely due to a SiC interfacial reconstruction, and not a single Moiré effect as previously suggested.[93,251] It is interesting to note that the rippling of the 6 x 6

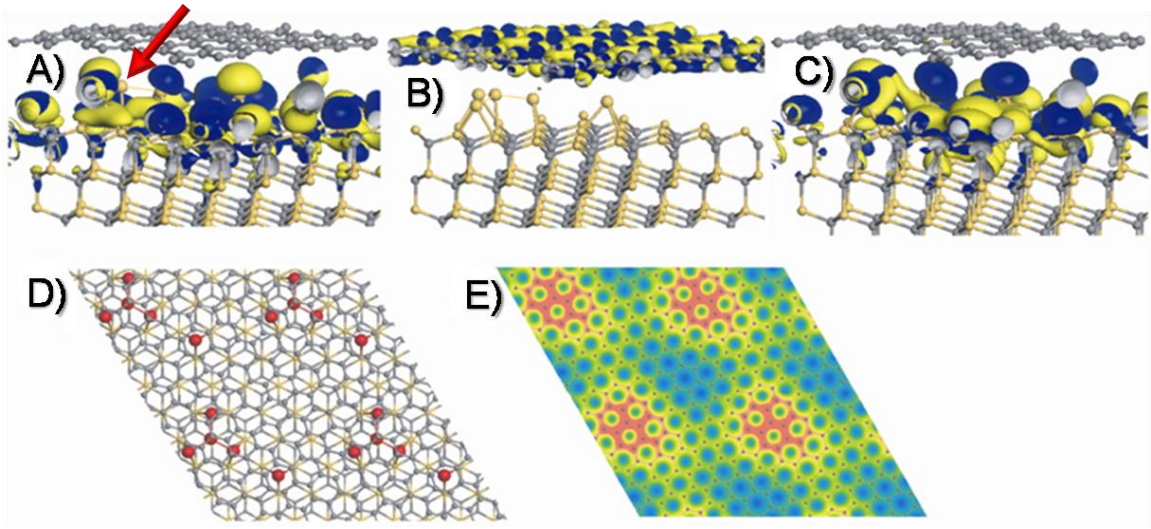

Figure 6.3

Iso-wave-function contours for a 5 x 5 SiC periodic cell with a Si tetramer and neighboring Si adatom underneath a graphene layer. The states are summed over energy windows of (A) roughly -0.8 to -0.1 eV below E_F, (B) within ≈ 0.1 eV of E_F, and (C) about 0.1-0.8 eV above E_F. The color scheme denotes the phase of the orbital. (D) Top-down view of the 5 x 5 cell (repeated for ease of viewing) with a tetramer and neighboring adatom at the interface displayed in red. (E) Slice of the total charge density above the graphene layer with carbon atomic sites indicated. Here, red indicates regions of highest charge density, and blue corresponds to lowest charge density.

periodicity (≈ 1 Å) is considerably smaller than the ripples observed in the STM images of exfoliated graphene on SiO_2, which has a corrugation of around 5 Å.[249,250]

For added support of effective imaging the interfacial structure below single-layer graphene, we have performed a first-principles density-functional theory (DFT) calculation of this system. Our DFT calculation has incorporated an atomic configuration of a single-layer of graphene above a simplified interfacial region on top of a bulk-terminated SiC. Essentially, the interfacial region consists of one Si tetramer and one Si additional atom, where the additional Si atom is one of the yellow atoms neighboring the tetramer in Fig. 6.1C. Full details of the DFT calculation can found in the reference: G. M. Rutter et al. *Phys. Rev. B* **76**, 235416 (2007).

Results from the DFT calculation have given insight into the nature of STM imaging of the first epitaxial graphene layer. Figure 6.3 shows a series of iso-wave-

function contours for three different energies (A) below, (B) near, and (C) above E_F. Iso-wave-function amplitude contours can be thought of as molecular orbitals describing the local density of states. SiC interface orbitals dominate the contours for energies above and below E_F, in agreement with the experimental findings (Figs. 6.2, A & D). In contrast, graphene states dominate the contours for energies within 0.1 eV of E_F, which accounts for the trend toward imaging the graphene lattice at low bias (Figs. 6.2, C & F). A large isocontour value was chosen to highlight the difference between the graphene states at E_F and the apparent gap in the SiC substrate density of states. A smaller isocontour value shows finite graphene density away from E_F. Interestingly, this orbital analysis also displays the difference observed in the appearance of the tetramers for filled versus empty states. Specifically, the on-top site of the tetramer has no orbital contribution over the displayed energy range for the filled states (red arrow in Fig. 6.3A), but is apparent in the empty states (Fig. 6.3C) leading to the appearance of trimers rather than tetramers in the STM images (Figs. 6.2, A & E).

These calculations also give insight into the 6 x 6 corrugation observed in the graphene STM images. Figure 6.3D shows a top view of the atomic positions for the calculated interface, while Fig. 6.3E shows the corresponding total charge density for a slice parallel to the interface positioned just above the graphene layer. We observe qualitatively good agreement between the charge density image and the graphene STM images (Figs. 6.2, C & F). The larger charge density in the vicinity of the Si tetramers arises from the buckling of the graphene lattice over the Si adatoms. This suggests that the 6 x 6 corrugation observed in the STM images is largely due to the graphene lattice draping over features of the interface reconstruction. In fact, the experimental corrugation amplitude of ≈ 1 Å is close to the geometric calculated displacement ≈ 0.6 Å. This is not surprising, since it is a common feature of the graphene lattice to deform and cover the surface, this will discussed more in Chapter 7.

6.2 Spectroscopic Characteristics of Single-Layer and Bare-SiC

To gain further insight into the electronic properties of this material, we have performed STS measurements over regions of the surface with both high and low interface state transmission. These measurements investigate further the role of the interface and the properties of single-layer epitaxial graphene at low temperature. We have found that the interface state features contribute a tremendous amount of information to the spectroscopy data. Figure 6.4 shows an area over single-layer graphene in which we performed an open loop dI/dV map. Figure 6.4A is the simultaneous STM topography at 0.3 V, while Fig. 6.4B is a dI/dV map taken at -0.3 V. From Fig. 6.4A it is clear that this area has a relatively disordered interface, since there are no signs of any hexagons and tetramers. In the dI/dV map (Fig. 6.4B) there are many trimer type features, pointed out by the yellow arrows. The green and blue curves, shown in Fig. 6.4C, are spatially-averaged spectra taken from the corresponding circles in the dI/dV image. These spectra show pronounced peaks that are large compared to the average differential conductance of the entire area, shown as the black plot of Fig. 6.4C. The empty-state contribution to the dI/dV signal appears similar between the averaged spectra taken over the interface states and over the whole region. The interface state peaks in the dI/dV spectra have been verified by another group.[198] The peak energy of the localized state is close to the voltage onset where imaging occurs in the STM topography. The energy of the peak should give insight into the electronic structure of the interface state, such as chemical composition and bonding arrangement, but the required theoretical calculations are not yet available.

Interestingly, high-resolution dI/dV measurements averaged over the entire image (Fig. 6.4D) show a reduction in the dI/dV signal within ± 50 mV about the Fermi energy. This feature, which has been observed by others,[198] is referred to as a pseudo-energy gap in the dI/dV spectrum. The term pseudo energy gap arises from having a reduced but nonzero dI/dV signal, where a zero differential conductance signal would be

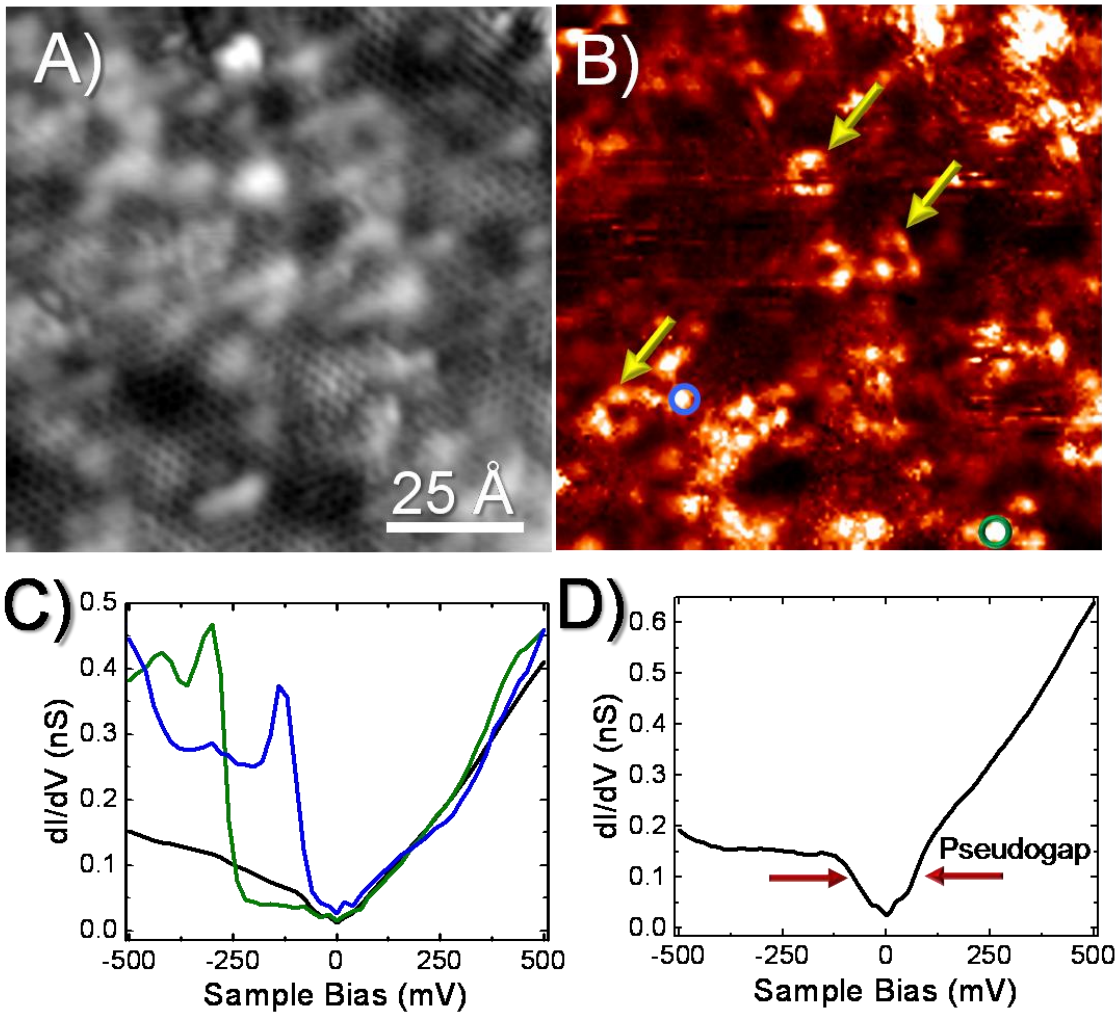

Figure 6.4

LTSTS spectra taken over interface states show large resonance peaks in the dI/dV. (A) 100 Å x 100 Å STM topography displaying the graphene lattice imaged alongside the interface states (tunneling conditions are 300 mV and 30 pA). (B) dI/dV map at -300 mV performed in the area of A. There are many trimer features in the dI/dV map pointed out by the yellow arrows. These trimer features arise from the empty state imaging of the tetramers, even though the tetramers are not imaged in A. (C) Spatially-averaged STS spectra taken from the dI/dV map in B. STS spectra from trimer regions (blue and green circles of B) have large peaks in the dI/dV. The peaks are very large compared to the signal from an averaged dI/dV over the entire region of B, shown as the black curve. (D) High-resolution spatially-averaged dI/dV over the area of A (tunneling conditions are 300 mV and 60 pA). It is clear from the plot that there is a reduction in signal over the range of ± 50 meV. This reduction in the LDOS of graphene is commonly referred to as a pseudogap, and arises from excitation of a characteristic phonon mode in graphene.

expected for a true energy gap. Outside of the pseudogap there is a step in the differential conductance signal. Such steps in the dI/dV are typically attributed to additional inelastic tunneling channels, such as molecule vibrational[252] or atomic spin excitations.[253] Similarly to these inelastic tunneling events, the step up observed here has been proposed as an increase in the final states of the tunneling electrons due to the excitation of a characteristic phonon mode of the graphene.[254] We have found that the observation of the phonon coupling is highly dependent on the tip geometry and tunneling impedance conditions. Future spectroscopic studies are needed to investigate this tip dependence further.

In addition to spectroscopic measurements from buried interface states, we have also investigated the bare-SiC reconstruction and compared the results from the room temperature measurements discussed in the Chapter 4. The sample studied in the previous sections was made with a relatively large coverage of single-layer graphene, about 90% of a monolayer. In the remaining 10% area, we have found small patches of exposed SiC reconstruction next to single-layer epitaxial graphene. Figure 6.5A shows an STM topography of one area where a strip of SiC is exposed and sandwiched on either side by single-layer graphene. Figure 6.5B shows spatially-averaged STS spectra taken over the two areas of single-layer graphene (red & black curves) and compared with STS spectra performed over the SiC (blue curve). The STS spectra taken from the SiC consistently shows a ≈ 300 mV gap centered at the Fermi energy. However, it is clear that this spectra does not show localized peaks that were observed buried at the graphene/SiC interface (discussed more below). The dI/dV spectra taken from the left and right graphene regions are essentially identical, showing a linear spectral behavior. These spectra do not show the pseudo energy gap, because the tip geometry is different from the data in Fig. 6.4.

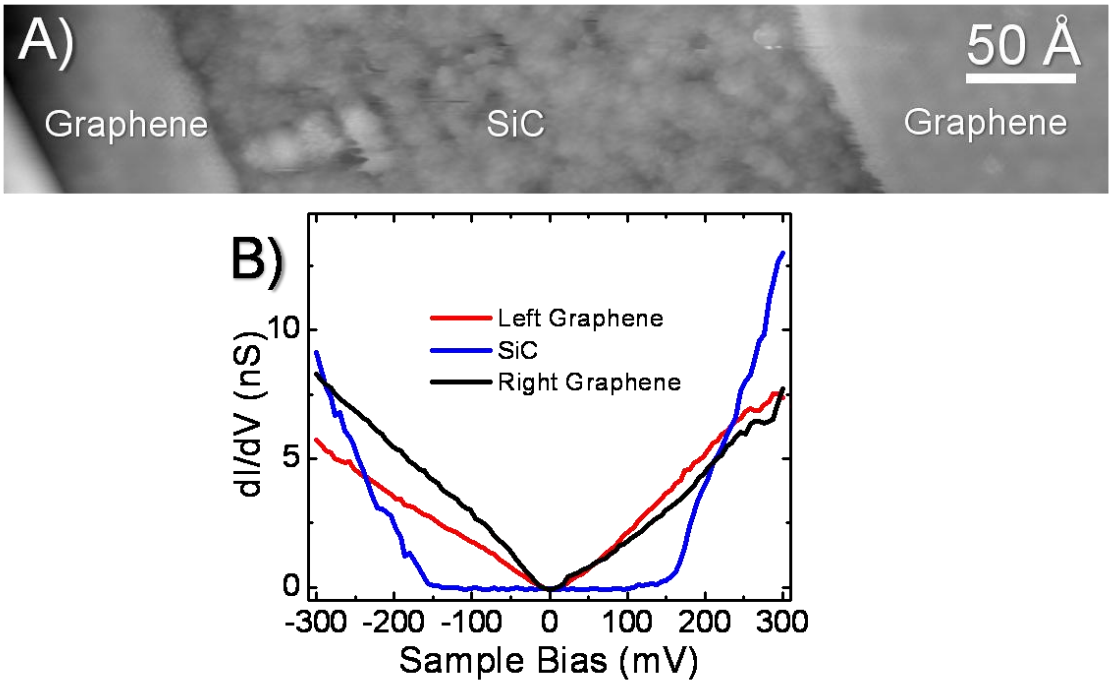

Figure 6.5

LTSTS of regions of SiC show a gap centered on the Fermi energy. (A) 500 Å x 200 Å STM topography displaying a patch of exposed SiC reconstruction surrounded on either side by graphene (tunneling conditions are 0.6 V and 0.1 nA). (B) Spatially-averaged dI/dV spectra taken on the regions of SiC (blue curve) and the left and right graphene regions, (red and black curve, respectively).

The imaging and spectroscopic data performed at low temperature over the SiC reconstruction are in direct contrast to room temperature measurements over similar regions (Chapter 4 & 5). In particular, the low temperature imaging of the SiC reconstruction looks more disordered than topographic images performed at room temperature over bare SiC (e.g. Fig. 4.6A). The low temperature STM and STS measurements do resemble similar effects seen on hydrogen passivated SiC discussed in last chapter. However, it is hard to determine whether the lower sample temperature has induced these changes in the SiC or there are other factors. This concludes our discussion on the properties of single-layer graphene and the SiC. The rest of this chapter will discuss characteristics of bilayer epitaxial graphene, starting first with the structural morphology of epitaxial graphene bilayer.

6.3 Morphology of Graphene Bilayers

Previous chapters have addressed the growth of single-layer graphene and its registry to the underlying SiC. This section will discuss the structural properties of the second layer of graphene with respect to the first layer. An example of how graphene transitions from single-layer and bilayer epitaxial graphene is illustrated in Fig. 6.6. Figure 6.6A is an STM topograph showing a surface step separating the two different graphene layers. Figure 6.6B shows a gradient-enhanced STM image magnified from the white box in Fig. 6.6A. It is clear from this image that the graphene lattice is continuous over the step edge, though partially obscured in places by interface states from the underlying SiC (white arrows of Fig. 6.6B). Typically, the second layer (right side of Fig. 6.6B) shows little sign of the interface states in the topographic images. This is due to the second graphene layer being offset from the first by over 3 Å, which equates to a decrease of the interface state contribution in the tunnel current by three orders of magnitude.

The continuity of epitaxial graphene from the top of the bilayer to the single layer implies a break in the graphene layer closest to the SiC interface. We know this because in STM studies of bulk graphite, when the top graphene layer terminates at a step edge (a geometry that can be created by tearing the layer during mechanical cleavage), strong scattering with a $\sqrt{3} \times \sqrt{3}R30^{\circ}$ periodicity relative to the graphite in-plane lattice vectors is observed.[195] We note an absence of $\sqrt{3} \times \sqrt{3}R30^{\circ}$ patterns at epitaxial graphene step edges separating single-layer and bilayer (Fig. 6.6B), due to the continuity of the graphene. Similar graphene continuity is observed over abnormalities in the interface layer found in the initial stages of graphene growth; this will be discussed further in the next chapter. In addition, we have found the blanketing nature of epitaxial graphene is similar over steps in the SiC substrate. It is interesting to note that a $\sqrt{3} \times \sqrt{3}R30^{\circ}$ scattering pattern is imaged between terraces of single-layer graphene and the SiC

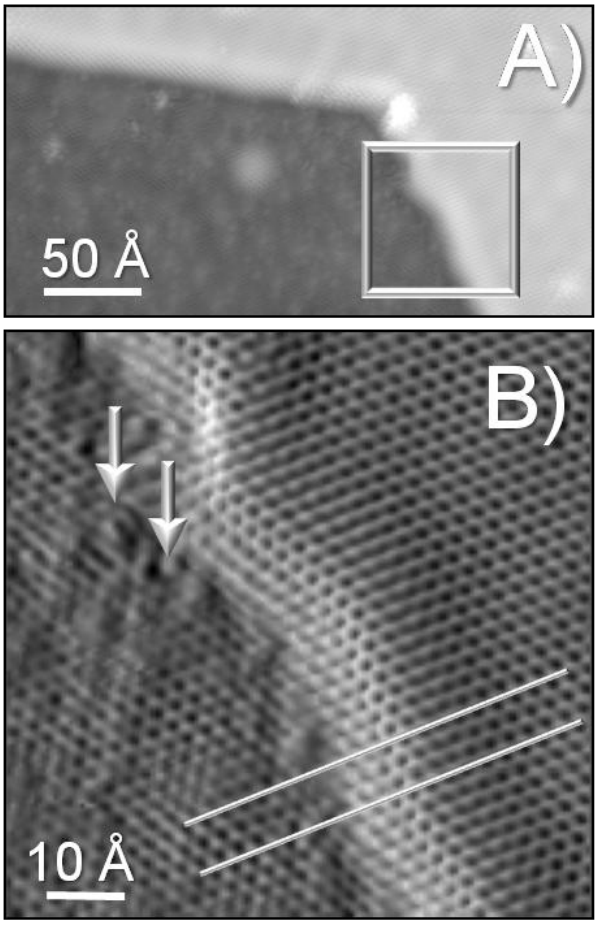

Figure 6.6

Epitaxial graphene is shown to overlay surface steps, with little apparent scattering of electron states. (A) 300 Å x 158 Å LTSTM topography at a tunneling bias and current of 0.3 V and 0.1 nA, respectively. This 3.1 Å step separates a region of single-layer and bilayer epitaxial graphene. (B) 75 Å x 75 Å gradient-enhanced STM image that was cropped from (A) as indicated by the white box. As shown by the white lines, the top most layer of graphene is essentially unperturbed by the step edge. Similar behavior is seen when epitaxial graphene overlays substrate SiC steps. The bumps that appear on the bottom terrace (white arrows) are actually the transmission of the interface states through the single-layer graphene, discussed earlier in this chapter.

reconstruction, see e.g. Fig. 4.4C. The result of a continuous top layer of graphene has some serious implications for device applications based on epitaxial graphene. If the SiC is graphitized with multiple layers of graphene, there is a high probability that the top layer will be continuous across the entire sample. The fabrication goal would be grow

continuous graphene on the wafer length scale, which has made epitaxial graphene appealing for mainstream integration of graphene in nanoelectronics.

6.4 Bias-Dependent Imaging of Bilayer Graphene

The ability to accurately determine the graphene thickness has allowed for the study of many structural and electronic properties that are dependent on the layer in question. In the case of bilayer graphene, we have developed a novel way to accurately determine the interlayer coupling between the layers, a very important quantity. Using a series of bias-dependent STM images, we have been able to identify the stacking of epitaxial graphene bilayers as Bernal, found commonly in bulk graphite. Bias-dependent imaging is sensitive to spatial variations in the energy dependence of the local density of states for the two sublattices in graphene. Figures 6.7A-C shows three STM images from a bilayer terrace, the sample bias is clearly marked on the image. At a sample bias of 0.1 V the graphene lattice appears triangular (Fig. 6.7A), indicating that only one of the two graphene sublattices is imaged. Similar images have been observed in STM studies of bulk graphite[255] and multilayer graphene surfaces.[181,194,198,249,250] An ideal graphene lattice, composed of the **A** (black circles) and **B** (red circles) sublattices, is displayed on the image to help illustrate the atomic positions. As the sample bias is increased to 0.3 V (Fig. 6.7B), STM images begin to show the second carbon sublattice at a lower intensity. At an even higher tunneling bias of 0.4 V (Fig. 6.7C), the images show a honeycomb structure similar to that observed for single-layer graphene, where both sublattices are imaged at almost the same intensity.[194,198,214,249,250]

This bias-dependent imaging occurs when the sublattices of graphene (equivalent for a single layer) become distinguishable due to the stacking of the two graphene layers, this concept was introduced in Chapter 3. In Bernal stacking, one sublattice of atoms in the top layer (**A** sublattice) is positioned directly over atoms in the bottom layer. However, atoms in the other top-layer sublattice (**B** sublattice) lie over hollow sites in the

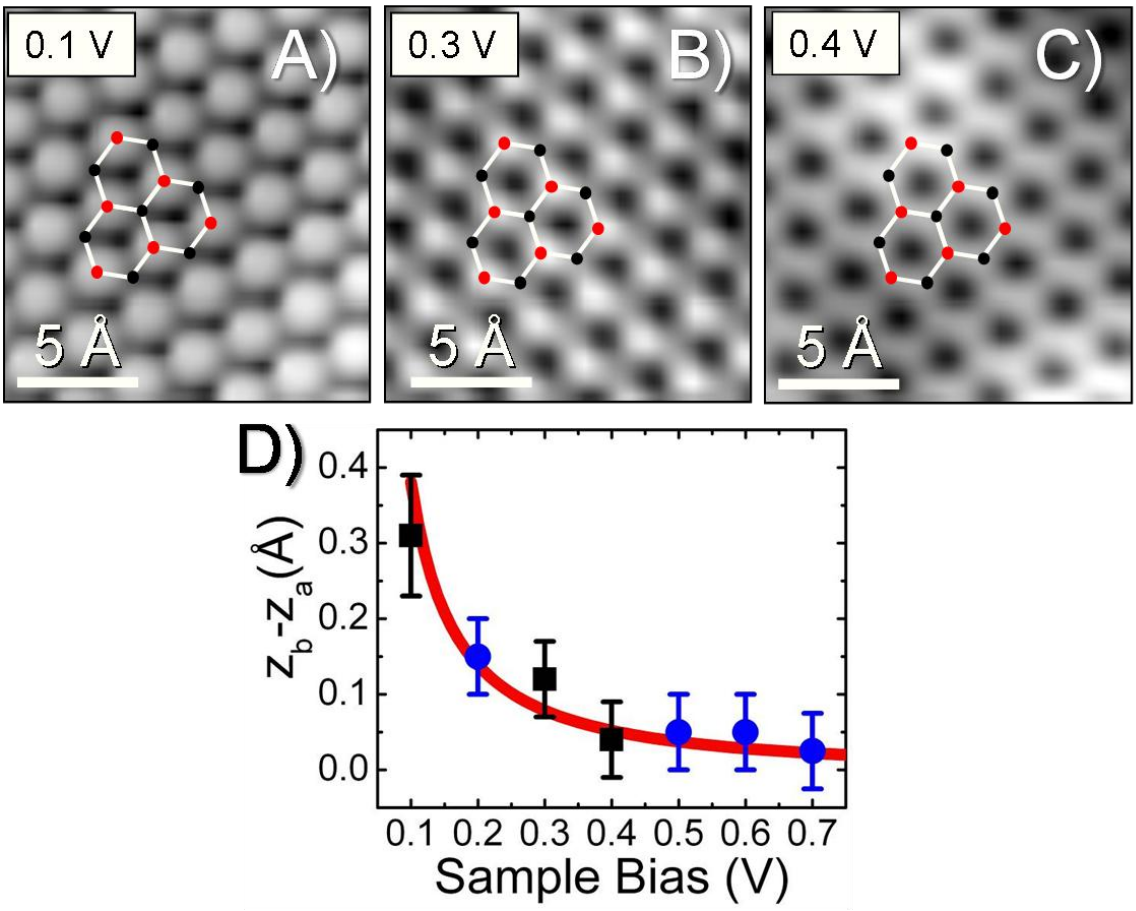

Figure 6.7

STM-measured apparent height differences between graphene basis atoms show Bernal stacking in bilayer epitaxial graphene. (A-C) 15 Å x 15 Å STM topographs of the same area at a constant current of 0.1 nA and tunneling bias of (A) 0.1 V, (B) 0.3 V and (C) 0.4 V. A schematic of a graphene lattice, showing approximate atomic positions, is overlaid on each image. Atoms on the **B** sublattice are shown in red and atoms on the **A** sublattice are shown in black. (D) Plot of the apparent height difference between atoms on the **B** and **A** sublattices. Experimental heights (black squares) were averaged from multiple line scans across several unit cells of the image A-C. Additional data at other biases (blue circles) are measured from another area of the sample with a different probe tip. These relative heights are plotted alongside the data from A-C for consistency and reproducibility. The data is compared with the calculated height difference (red line), obtained using independently measured parameters (see text).

bottom layer, making the two sublattices inequivalent. This configuration results in a reduction in the low-energy density of states for the **A** sublattice as compared to the **B** sublattice, which suppresses the **A** sublattice imaging at low tunneling energies.[163,164] At energies larger than the interlayer hopping energy, the two sublattices have essentially

identical density of states. Since the STM tunneling current can be approximated as an integral over the density of states from zero volts (Fermi energy) to the applied bias voltage (e.g. Eq. 2.3), the transition can be seen in the experimental data. The STM images show qualitative agreement with the theory: At low bias the **A** sublattice density of states is suppressed, yielding images of only the **B** sublattice (Fig. 6.7A). At higher bias, both sublattices image equivalently in the topography (Fig. 6.7C).

A more quantitative analysis can be made by measuring the apparent height difference between atoms on the **A** and **B** sublattices (seen in Figs. 6.7A-C) and comparing to estimates based on the theoretical local density of states.[164] The apparent height difference corresponds to the actual change in the tip/sample separation between the two carbon atoms, or $z_B - z_A$. To achieve this quantity, we combine a simple tunneling model[62,70] and the sublattice densities of states for ideal bilayer graphene (Eqs. 3.53 & 3.54). In Chapter 2, I introduced the approximation for the STM tunneling current with respect to the tip/sample separation. Here I rewrite that approximation for the sublattice-dependent tunneling current:

$$I_i \approx I_i^o \exp(-2\kappa z_i) \tag{6.1}$$

where $i = A, B$ and I_i^o is the initial tunneling current on sublattice i. The expression I_i^o can be written for each sublattice as:

$$I_i^o \propto \int_{E_F}^{eV_s} \rho_i(E) dE\,, \tag{6.2}$$

where $\rho_i(E)$ is the density of states on sublattice i. In Chapter 3, the local density of states for bilayer graphene was explicitly defined for the two energy regions: $|E| < \tau_\perp$ and $|E| > \tau_\perp$ (Eqs. 3.53 & 3.54), where $\tau_\perp$ is the interlayer hopping energy. By incorporating the two expressions of Eq. 6.1 such that

$$I_B = I_A \tag{6.3}$$

(due to constant current imaging), we can derive an expression for the difference in the apparent height on the two sublattices:

$$z_B - z_A = \frac{1}{2\kappa} \ln \int_{E_F}^{eV_s} \rho_B(E)dE \Big/ \int_{E_F}^{eV_s} \rho_A(E)dE \quad . \tag{6.4}$$

Figure 6.7D shows as black squares the measured values of $z_B - z_A$ from the topography in Figs. 6.7A-C. Also included in the plot are relative heights at biases not shown in Figs. 6.7A-C (blue circles). These data are taken on another area of the sample with a different probe tip, which verifies the consistency and reproducibility of the analysis. The solid red line in Fig. 6.7D corresponds to Eq. 6.4 with 2κ = 2 Å^{-1}, E_F = 0.3 eV, $\tau_\perp$ = 0.4 eV, and $\rho_i(E)$ from Eqs. 3.53 & 3.54. Although the data is not extensive, the agreement between experiment and theory is remarkable, using parameters that have been determined independently. In particular, the value for the Fermi energy is precisely what is expected for epitaxial graphene via electronic transport,[52] ARPES,[146] and STS measurements.[181] In addition, the interlayer coupling is exactly the same as the experimentally observed value for bulk graphite samples.[162] The value of the decay constant κ has also been shown to be constant (≈ 1 Å^{-1}) over the energies in Fig. 6.7.[254] Remarkably, using this simple model we find good agreement with experiment, which implies that the stacking order of bilayer epitaxial graphene is Bernal and that the interlayer coupling energy is very similar to graphite. However, we would like to point out that the specific imaging transition can be tip dependent, but it is usually observed within the energy range shown in Fig. 6.7.

6.5 Conclusion

In this chapter, I have talked about many different properties of single-layer epitaxial graphene, graphene/SiC interface, and bilayer epitaxial graphene. To characterize these properties, we utilized STM and STS measurements performed at 4.2 K. I showed that the first monolayer of graphene becomes transparent to tunneling electrons at energies ± 1V. This transparency allows for a unique study of the role the interface plays in the graphene's electronic properties and morphology. Bias-dependent STM images of single-layer epitaxial graphene have shown that structural ripples in the graphene originate from the corrugations in the SiC reconstruction. A first principles DFT calculation verifies the energy dependence of the graphene transparency and offers an explanation to the observed corrugation of the experimental STM images. Spectroscopy measurements indicate that there are large localized states at the graphene/SiC interface. Such states arise from dangling Si bonds, and will most likely be detrimental to the operation of any epitaxial graphene device. Areas of exposed SiC show no signs of such large localized states in the spectroscopy, but we do observe a band gap roughly on the order of 300 mV. Further test are need to investigate the origin of the energy gap seen on the exposed SiC.

In addition to STM studies of single-layer epitaxial graphene, I also showed many different properties of bilayer epitaxial graphene. In particular, I have observed the continuity of graphene over thickness changes and SiC step edges. This indicates that the top layer across an entire multilayer graphene sample is made from the same sheet of graphene. Next, I discussed how bias-dependent STM imaging can confirm the stacking of bilayer graphene as Bernal, the most common form of bulk graphite. Finally, using a simple tunneling model and the density of states for ideal bilayer graphene, I was able to fully describe the images of bilayer epitaxial graphene and extract the interlayer coupling between the graphene layers.

CHAPTER 7

SCATTERING AND INTERFERENCE IN EPITAXIAL GRAPHENE

It is well known that defects play an influential role in the macroscopic transport characteristics of graphene. Specifically, graphene samples with a large quantity defects, especially charged impurities at the surface and interface, will have poor device performance.[113,137] On the other hand, the absence of defects quenches the half-integer quantum Hall effect, which is the hallmark of graphene.[256] In what follows, I discuss the first microscopic study of scattering in graphene that relates the presence of atomic-scale defects to macroscopic transport phenomena. It is important to note that for monolayer epitaxial graphene, the interface contribution to the STM topography can complicate the scattering studies. Therefore, I have mainly focused our investigations on bilayer epitaxial graphene, but I will discuss single-layer scattering later in the chapter.

To start this chapter, we offer an introduction to the different types of disorder found on the epitaxial graphene surface. Next, we discuss how certain defects in graphene can give rise to the two types of elastic scattering, intra- and intervalley scattering, which was introduced in Chapter 3. Using Fourier transform-STS techniques, we are able to measure the energy vs. wave vector dispersion of graphene on the atomic-scale. Finally, I offer discussion on how the scattering observed in our measurements relates to macroscopic transport characteristics.

Contents of this chapter have been discussed in the following publication:

G. M. Rutter *et al.*, "Scattering and interference in epitaxial graphene." *Science* **317**, 219 (2007)

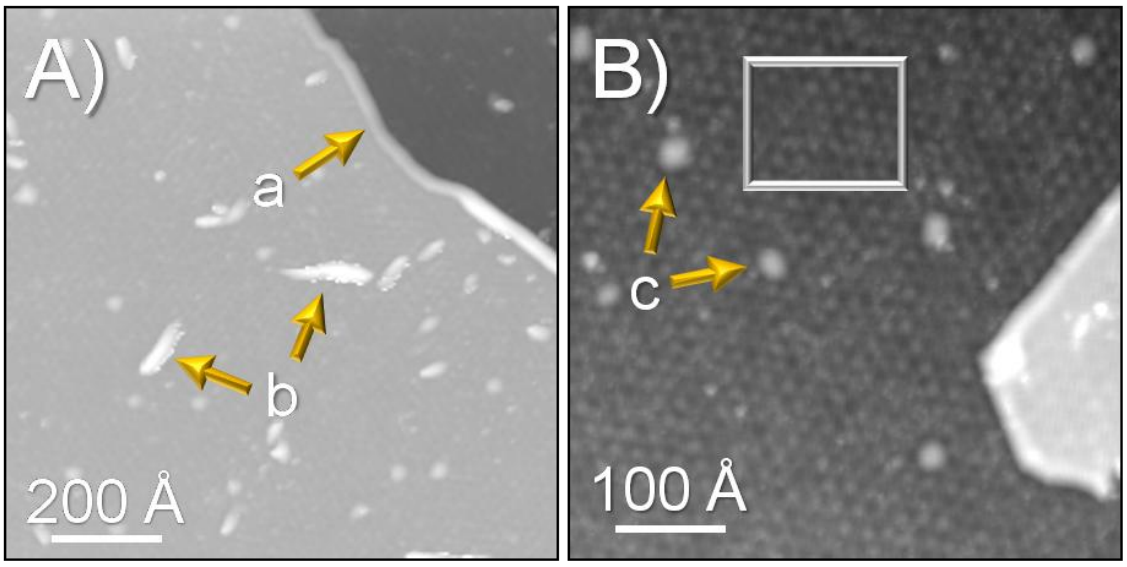

Figure 7.1

Survey STM images display the different forms of extended features underneath bilayer epitaxial graphene on SiC. (A) 1000 Å x 1000 Å STM topograph at tunneling conditions 0.4 V and 0.1 nA. Yellow arrows are drawn to indicate surface steps (labeled **a**) and tubular mounds (labeled **b**). The tubular mounds may be the initial formation of carbon nanotubes. (B) 500 Å x 500 Å STM topograph at a tunneling conditions 0.3 V and 0.1 nA. Indicated in this image are round mounds of possibly accumulated interface adatoms (labeled **c**) and the SiC interface reconstruction (height modulations seen in the white box).

7.1 Types of Defects in Epitaxial Graphene

Survey STM topographs reveal different structures that are large compared to the graphene lattice and occur commonly on this surface, as seen in Fig. 7.1. These structures that originate from the SiC substrate are: atomic steps (labeled **a** in Fig. 7.1A), tubular mounds (perhaps an early stage of carbon nanotube growth; labeled **b** in Fig. 7.1A), round mounds (labeled **c** in Fig. 7.1B) and the superstructure modulation (seen as a small regular height modulation in the white box of Fig. 7.1B). The superstructure modulation has a period of ≈ 2 nm caused by a reconstruction of the SiC interface beneath the graphene. Interestingly, the **b** and **c** type mounds are rarely found on samples studied by room temperature STM after in-situ graphene growth, as seen in Chapter 4. We believe that they are a consequence of atmospheric exposure, and subsequent UHV annealing. Despite their large size, all the structures of Fig. 7.1 cause little scattering of

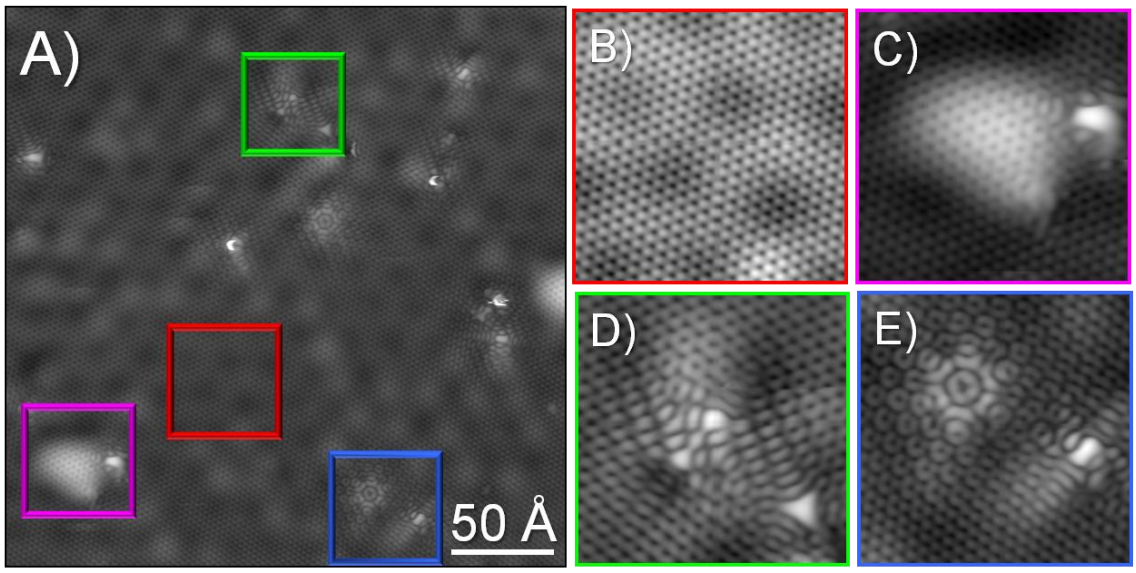

Figure 7.2

STM topographic images of defects in the bilayer epitaxial graphene sample. (A) 250 Å x 250 Å STM topograph showing a variety atomic-scale defects (tunneling conditions are 300 mV and 100 pA). Parts B-E are higher magnification images from the color-coded boxed regions in A. (B & C) Type I defects arise from the SiC substrate roughness such as (B) the SiC interface reconstruction or (C) subsurface irregularities. The graphene blankets type I defects seemly unaware of their existence. (D & E) Type II defects are atomic-scale defects located in or under the graphene lattice. STM images show complex scattering patterns around type II defects. The symmetry of the scattering pattern gives insight into the atomic structure of the defect.

charge carriers in the graphene. Strong scatterers of the electronic states are easily discernable in STM images from the appearance of a $\sqrt{3} \times \sqrt{3}R30^{\circ}$ pattern with respect to the graphene lattice (discussed more below) whereas no such patterns are observed in the vicinity of the aforementioned structures.

STM topographic images (Figs. 7.2, A - E) show different types of disorder for bilayer epitaxial graphene on SiC(0001) at the atomic scale. At this length scale, the bilayer graphene is imaged as a triangular lattice (Fig. 7.2B), characteristic of imaging only one of the two graphene sublattices. Figure 7.2A reveals two categories of defects, which we call type I and II. Type I defects, such as the SiC reconstruction and interfacial disorder (Figs. 7.2, B & C, respectively), have an unperturbed graphene overlayer that is continuous across them, akin to a blanket. As discussed in the previous section, these

defects are due to irregularities in the interface layer between graphene and the SiC. In contrast, type II defects are atomic defects within or underneath the graphene lattice itself (Figs. 7.2, D & E) and are accompanied by strong distortions in the local lattice images. These distortions are of electronic origin and are accompanied by large increases in the local density of states at the defect site.[145,257,258] Quasiparticle scattering from type II defects gives rise to spectacular patterns in the topographic images (Figs. 7.2, D & E), resulting from the symmetry of the graphene Bloch states.[259-261]

The atomic structure of defects is related to the symmetry of the scattering pattern observed in topographic images.[262] It is well known from STM studies of graphite that a vacancy (missing carbon atom) in the graphene layer will give rise a three-fold scattering pattern.[259] In addition, information can be gathered about the particular sublattice of the vacancy just by the rotation of the three-fold pattern.[260] Two-fold scattering patterns in STM images of carbon nanotubes (e.g. left defect in Fig. 7.2D) have been known to arise from graphene honeycombs with a different number of carbon atoms instead of 6.[263] These defects are often referred to as Stone-Wales or inverse Stone-Wales defects, and are of present interest for device nanoengineering of graphene.[264] In addition, we have observed a defect that seems to be unique to epitaxial graphene. This defect gives rise to the six-fold scattering pattern in Fig. 7.2E, which has been observed by another group.[265] Through a careful analysis of the atomic configuration of this defect, we have found that the scattering originates from the center of the graphene honeycomb. Therefore, we suspect that this defect is positioned in the underlying graphene layer on a **B** sublattice site. Due to the Bernal stacking of the bilayer, the scattering symmetry would originate from the center of the honeycomb of the top layer.

7.2 Scattering dI/dV maps

Detailed information on scattering from both types of defects is obtained from STS maps of the differential conductance, dI/dV (Fig. 7.3), which is determined by the

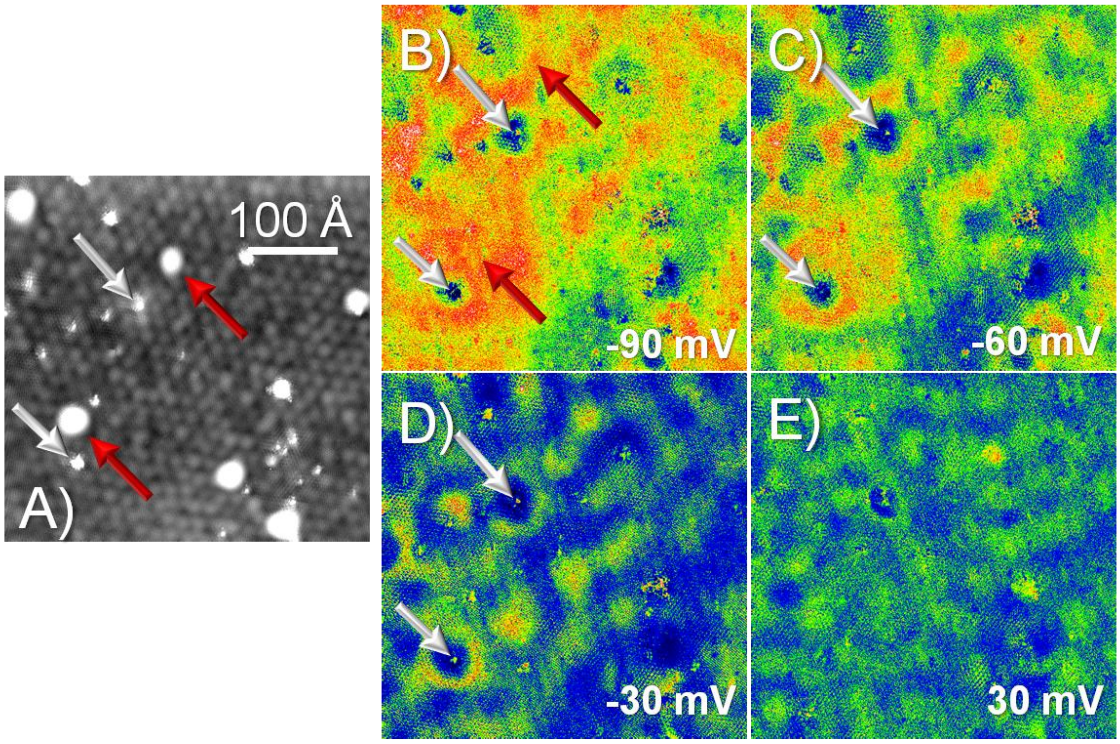

Figure 7.3

Defect scattering in bilayer epitaxial graphene. (A) 400 Å x 400 Å STM topograph and (B-E) simultaneously-acquired spectroscopic *dI/dV* maps performed in open-loop mode. Type I defects (round mounds) are labeled with red arrows and type II with white arrows. Sample biases are: (B) -90 mV, (C) -60 mV, (D) -30 mV, and (E) 30 mV. I = 500 pA, V = 100 mV, AC modulation ΔV = 1 mV_{RMS}. It is clear from the dI/dV maps that type II defects cause the largest perturbation to the local density of states of the graphene. The presence of these defects causes a standing wave pattern in the electronic states, which changes wavelength with respect to energy.

LDOS. By comparing the topographic and spectroscopic images we find that type II defects in the graphene lattice are the dominant scattering centers. Over much of the energy range studied, these atomic-scale defects have a large central density of states surrounded by a strong reduction in the LDOS that appears to pin the phase of the scattering pattern nearby. For example, the type II defects labeled by white arrows in Fig. 7.3, show a bright central spot encircled by a dark region and a bright ring (Figs. 7.3, B - E). Circular conductance maxima can be seen centered at the point defect sites. These prominent features may be a consequence of nonlinear, and potentially ambipolar, screening in this low-density system. In contrast, the dI/dV maps show that type I

defects, over which the graphene is continuous (red arrows), have dramatically less influence on the LDOS.

Over large length scales, the dI/dV maps exhibit long-wavelength fluctuations that change with sample bias voltage (Figs. 7.3, B - E). As the sample voltage increases from -100 mV to +100 mV, the dominant wavelength decreases correspondingly from 9 nm to 5 nm. Fluctuations of much shorter wavelength are also present in these dI/dV maps, but they are not apparent over such a large displayed area. Figure 7.4 shows the short wavelength modulations in dI/dV maps taken with atomic-scale spatial resolution. The interference patterns in these maps display a local $\sqrt{3} \times \sqrt{3}R30^{\circ}$ structure (Figs. 7.4, B - E) with respect to the graphene lattice, with a superimposed long-wavelength modulation.

In addition to states localized on defect sites, sharp conductance peaks, ≈ 5 meV in width, are found several nanometers from the nearest type II defect (Fig. 7.4). The peaks are clearly associated with LDOS modulation, as can be seen in the dI/dV maps (Figs. 7.4, B - E) and the spectral line profiles (Figs. 7.4, F - I). Furthermore, the data shows that these conductance peaks are spatially localized, with maximum intensity in regions of constructive interference (i.e. over broad maxima modulating the pattern in Figs. 7.4, B - E). We attribute these conductance peaks to scattering resonances, which localize quasiparticles due to constructive interference in scattering from the random arrangement of defects found within a phase coherence length, discussed in detail later in this chapter.

In support of these conclusions, Figs. 7.4F - I, display sequences of dI/dV spectra taken along the red lines shown in Figs. 7.4B - E, (note that the red lines are in regions of maximum intensity modulation for the four different energies of the dI/dV maps in parts B through E). Each of the figures shows a very prominent modulation along the vertical (distance) axis at the energy of the corresponding dI/dV map (B - E). The lower set of panels (J - M) show dI/dV spectra obtained at positions of the maxima,

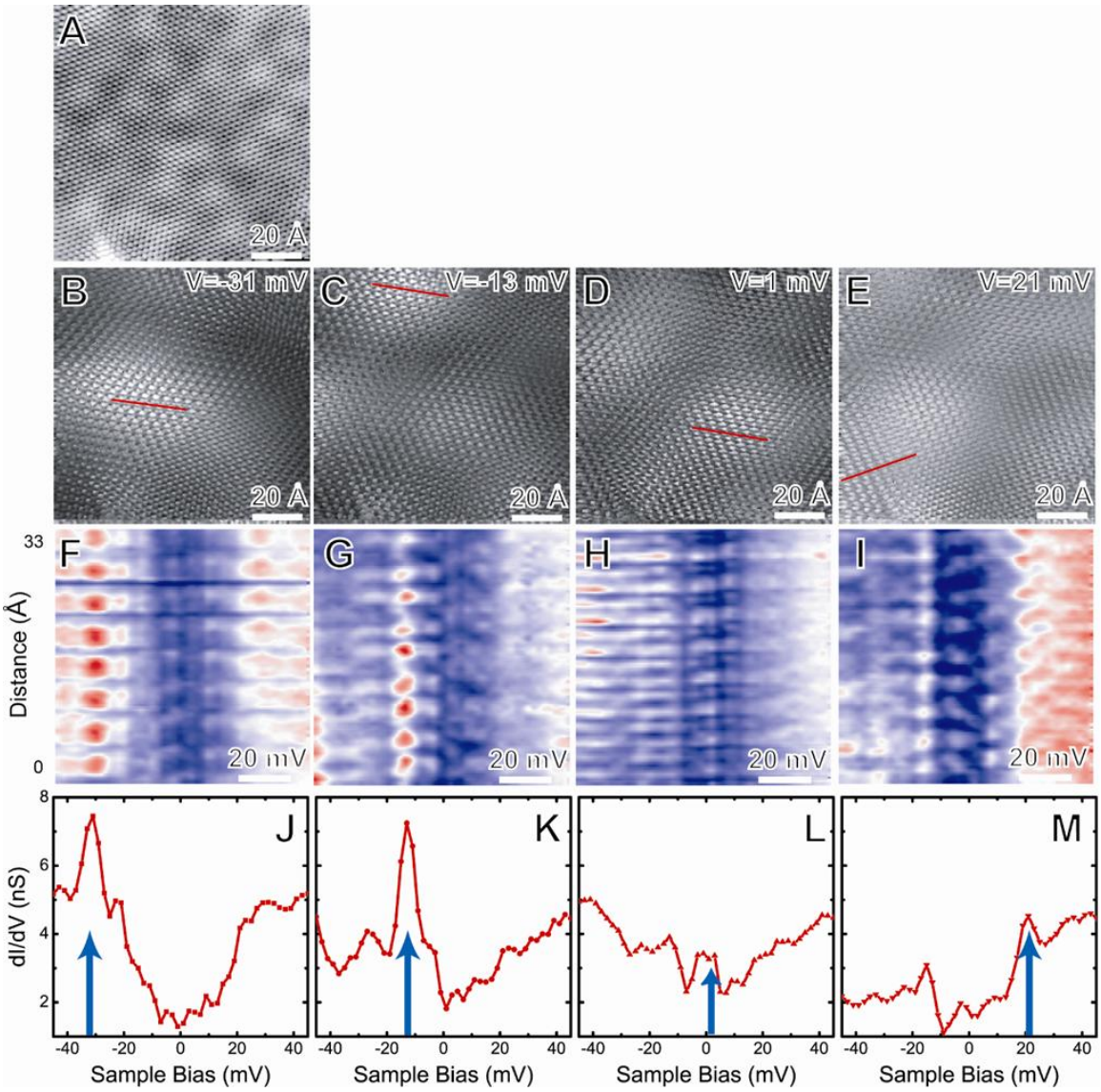

Figure 7.4

100 Å x 100 Å STM topography of bilayer epitaxial graphene (A), and simultaneous open-loop *dI/dV* maps at sample bias voltages of (B) -31mV, (C) -13 mV, (D) 1.0 mV, and (E) 21 mV. The type II scattering centers lie outside the image region (see lower left corner of A). (F-I) *dI/dV* (color scale) versus sample bias (horizontal axis) and distance (vertical axis) along corresponding red lines in (B to E). The blue-white-red color scale spans the conductance values observed in (J-M). (J-M) line-averaged dI/dV spectra obtained from regions marked by red lines in (B to E). The spectra are averages of nine curves acquired at positions of the $\sqrt{3}$x$\sqrt{3}$ interference maxima in the region of the red lines. Peaks in the *dI/dV* spectra correlate with maxima in the long-wavelength modulation of the $\sqrt{3}$x$\sqrt{3}$ interference pattern. Blue arrows indicate the bias (energy) position of the corresponding conductance images in (B to E). I = 500 pA, V = 100 mV, AC modulation ΔV = 0.7 mV_{RMS}.

in the general areas of constructive interference (i.e. near the red lines). Clearly, the energy-dependent standing-wave patterns are associated with conductance peaks of different energies. Across the series of maps and spectra, resonances decrease in intensity as new ones acquire increased spectral strength; each corresponding to a particular spatial location of constructive interference in B - E. Resonances are seen in parts F/J at -31 mV, in G/K at -13 mV, straddling the Fermi energy at ±1 mV in H/L, and at several energies above the Fermi level in parts I/M. Many more spectral peaks are observed for different spatial locations in the data set in Fig. 7.4, with equally narrow line widths.

Both the long wavelength standing-wave modulations (Fig. 7.3) and the √3 x √3R30º periodicity (Fig. 7.4) are due to quasiparticle scattering from type II defects through wavevectors determined by the electronic structure of epitaxial graphene. The two-dimensional constant energy contours in reciprocal space (Fig. 7.5A) are used to understand the scattering vectors that define the interference patterns observed in the STS maps of Figs. 7.3 and 7.4. For graphene the constant energy contours near E_F cut through the electron and hole conical sheets resulting in small circles of radius κ, centered at the wavevectors $\mathbf{K}_+$ and $\mathbf{K}_-$ that each locate 3 symmetry-equivalent corners of the 2D Brillouin zone. The scattering wavevectors $\mathbf{q}$ connect different points on the constant energy contours (Fig. 7.5A). Two dominant families of scattering vectors, labeled $\mathbf{q_1}$ and $\mathbf{q_2}$, give rise to the patterns observed in the spectroscopic conductance maps. Wavevectors $\mathbf{q_1}$ connect points on a single constant-energy circle (intravalley connect constant-energy circles at adjacent $\mathbf{K}_+$ and $\mathbf{K}_-$ points (intervalley scattering), yielding scattering wavevectors close in length to $\mathbf{K}_\pm$. $\mathbf{K}_+$ ($\mathbf{K}_-$) is related to the reciprocal lattice vectors $\mathbf{G}$ by a rotation of 30º(-30º) and a length that is shorter by

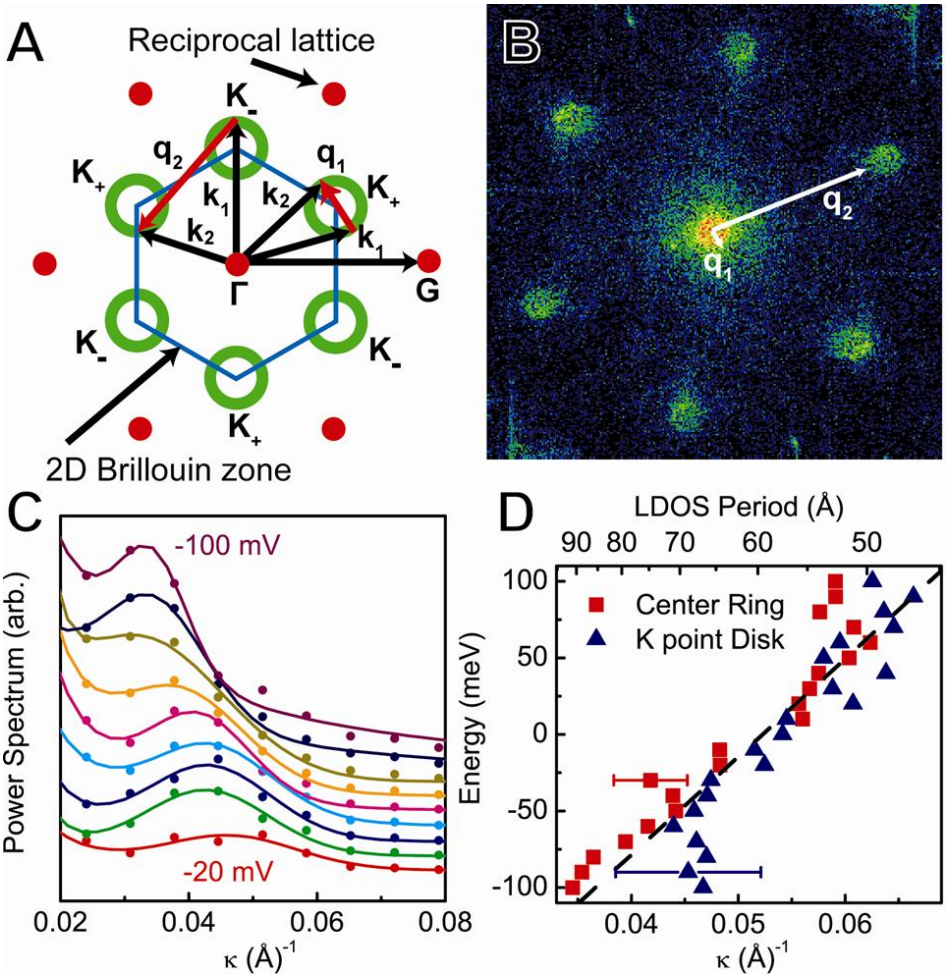

Figure 7.5

(A) Schematic of the 2D Brillouin zone (blue), constant energy contours (green) at the $\mathbf{K}_{\pm}$ points, and the two dominant classes of scattering vectors that create the interference patterns. Scattering wavevectors $\mathbf{q_1}$ (red) are seen to connect points on a single constant-energy circle, and $\mathbf{q_2}$ (red) connects points on constant-energy circles between adjacent $\mathbf{K}_{+}$ and $\mathbf{K}_{-}$ points. (B) $\mathbf{q}$-space map of scattering amplitudes, obtained from the Fourier transform power spectrum of the *dI/dV* map in Fig. 7.3D. $\mathbf{q_1}$ scattering forms the small ring at $\mathbf{q} = \mathbf{0}$, while $\mathbf{q_2}$ events create the six circular rings at $\mathbf{K}_{\pm}$ points. (C) Angular averages of the central $\mathbf{q_1}$ ring from the $\mathbf{q}$-space maps, at bias voltages from -100 mV to -20 mV shown in 10 mV increments. (D) Energy dispersion as a function of κ for bilayer graphene determined from the $\mathbf{q}$-space profiles in (C) and similar data. Values shown are derived from the radii of the central $\mathbf{q_1}$ scattering rings (red squares) and from the angled-averaged radii of the scattering rings at $\mathbf{K}_{+}$ and $\mathbf{K}_{-}$ (blue triangles). Dashed line shows a linear fit to the data with a Fermi velocity of $v_F = 9.7 \pm 0.6 \text{ x } 10^5$ m/s, and an energy intercept of -330 ± 20 meV. Similar results are found for a single monolayer of graphene (see Fig. 7.7).

$1/\sqrt{3}$ in reciprocal space. This gives rise to the $\sqrt{3}$x$\sqrt{3}$ R30º real space superstructures observed in the high resolution maps (Figs. 7.4, B to E). The vectors $\mathbf{q_2}$ will differ from the exact $\mathbf{K}_{\pm}$ wavevector due to the finite size of the Fermi circle contours. The scattering) and determine the observed long wavelength patterns. Wavevectors $\mathbf{q_2}$ combination of different lengths contributing to $\mathbf{q_2}$ leads to the modulation of the $\sqrt{3}$x$\sqrt{3}$ R30º scattering patterns in Fig. 7.4.

To quantify the observed interference patterns and deduce the local band structure, we obtain $\mathbf{q}$-space images of the scattering vectors (Figure 7.5B) from Fourier transform power spectra of the spectroscopic *dI/dV* maps.[80,81] Here, $\mathbf{q_1}$ scattering appears as a bright ring centered at $\mathbf{q}=0$. This is consistent with theoretical FTSTS predictions for bilayer graphene.[182] The ring is a consequence of the enhanced phase space for scattering near spanning vectors of the constant-energy circle. Circular rings also appear centered at the $\mathbf{K}_{+}$ and $\mathbf{K}_{-}$ points due to the distribution of $\mathbf{q_2}$ wavevectors. We determined ring radii for the central ring (Fig. 7.5C) and the $\mathbf{K}_{\pm}$ point rings using angular averages to maximize the signal-to-noise ratio. Both features change radius as a function of bias voltage due to dispersion in the graphene electronic states, and for these extremal $\mathbf{q}$ values, the scattering geometry determines $|\mathbf{q}| = 2\kappa$ or $|\mathbf{q} \pm \mathbf{K}_{\pm}| = 2\kappa$. The resulting κ-values vary linearly with energy (Fig. 7.5D) with a Fermi velocity of $v_F = 9.7 \pm 0.6 \text{ x } 10^5$ m/s. The $\kappa = 0$ energy intercept gives the Dirac energy, $E_F - E_D = 330 \pm 20$ meV.

In the previous section, we were able to determine the band dispersion for bilayer epitaxial graphene with STS on the atomic scale. Now, I would like to compare directly this STS dispersion to dispersions obtained via angle resolved photoemission spectroscopy (ARPES). Figure 7.6 shows a plot of the ARPES dispersion of bilayer

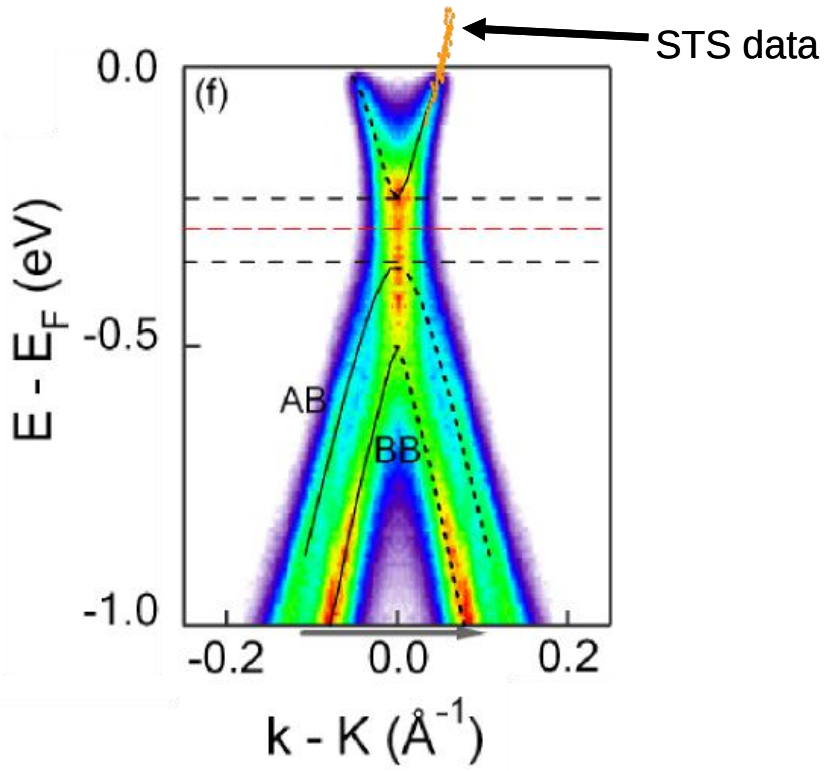

Figure 7.6

ARPES data taken from Zhou et al.[147] performed on bilayer epitaxial graphene prepared similarly to that studied in this work. The dispersion from the ARPES shows the band structure predicted in chapter 3 for bilayer graphene, with an energy gap at the Dirac point. Overlaid on the ARPES data is the STS dispersion measured in this work. The STS matches quite well to the ARPES data, where they overlap in the region of occupied states.

epitaxial graphene performed on a sample similar to that used in our study. ARPES data taken from Zhou et al.[147] shows the band structure typical for bilayer epitaxial graphene, as well as an energy gap around the Dirac point. The solid lines are the predicted band structure discussed in Chapter 3 for biased-bilayer graphene. This energy gap has been attributed to a potential difference between the two layers of bilayer epitaxial graphene, arising from the charged interface region below the first layer. Superimposed on the ARPES data, is the data from the STS dispersion analysis described in this work. Clearly, the nanometer-scale dispersion from FTSTS agrees well with the micron-scale dispersions from ARPES.

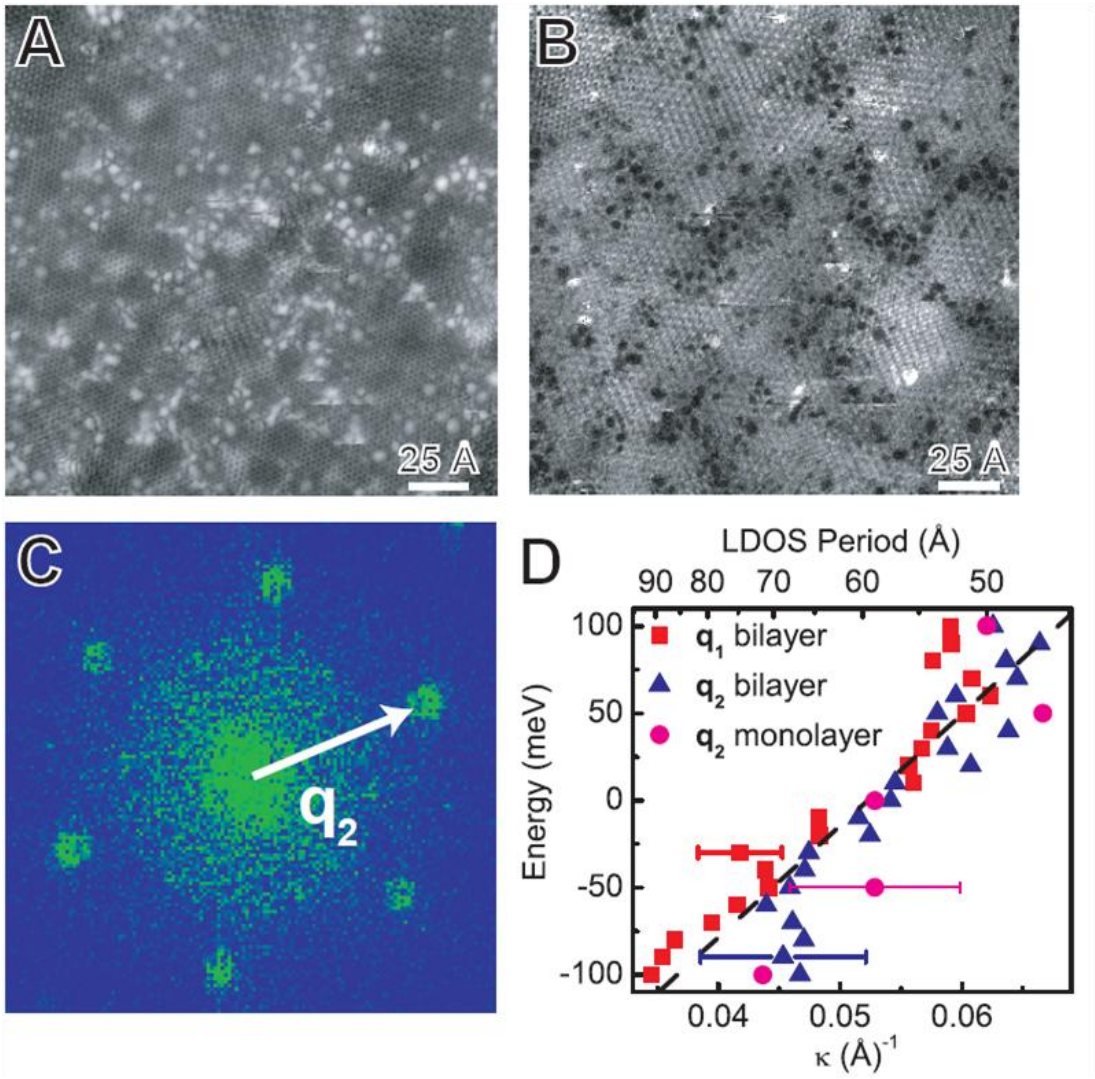

Figure 7.7

Scattering in single-layer epitaxial graphene. (A) 200 Å x 200 Å STM topographic image and (B) Simultaneously acquired *dI/dV* map at V = 50 mV. Tunneling setpoint: I = 10 pA, V= -0.3 V, AC modulation ΔV = 10 mV_{RMS}. (C) **q**-space map from the Fourier transform power spectrum of the *dI/dV* map in (B) showing intervalley $\mathbf{q}_2$ scattering at the $\mathbf{K}_{\pm}$ points. (D) Energy dispersion as a function of κ for single and bilayer layer graphene. Single layer values (magenta circles) are determined from the angle-averaged radii of the scattering rings at $\mathbf{K}_{\pm}$ points as shown in (C), and are plotted with the bilayer values (red squares and blue triangles) from Fig. 7.5D. The dashed line is a linear fit to the bilayer data.

In the region describing the charge carriers near E_F, the dispersions for monolayer and bilayer are similar. It is near the Dirac (charge neutrality) point that they are different: linear for the monolayer and quadratic for the bilayer. ARPES

measurements find $E_F - E_D$ to be slightly smaller for the bilayer than for the monolayer.[147] Interference patterns from defect scattering are also visible in a single layer of epitaxial graphene (Fig. 7.7). The Fermi level dI/dV map in Fig. 7.7B shows prominently the local $\sqrt{3}x\sqrt{3}$ R30º structure due to $\mathbf{q_2}$ intervalley scattering. The black spots in the dI/dV map are due to SiC interface states beneath the graphene layer (Fig. 7.7A). The presence of long wavelength $\mathbf{q_1}$ scattering is less certain, partly due to the interface states. Further spectroscopic measurements with larger image sizes are needed to determine whether $\mathbf{q_1}$-induced standing waves are completely absent for the monolayer. A preliminary measurement of the local dispersion for single layer graphene is thus only available from $\mathbf{q_2}$ scattering (Figs. 7.7, C - D). The monolayer dispersion follows the linear relation determined for the bilayer with apparently a slightly more negative energy intercept, consistent with photoemission data.[173]

7.3 Quasiparticle Localization and Transport

A phenomenological measure of the localization due to scattering in 2D systems can be obtained from the relative magnitude of the density of states corrugation.[82] Standing waves in two dimensions have zero LDOS at the nodes of the wavefunctions, therefore, localization in 2-dimensions yields large values for the relative LDOS corrugation, defined as $(dI/dV_{MEAN} - dI/dV_{MIN})/(dI/dV_{MEAN})$. Figure 7.8 shows histograms of the measured conductance values and the resulting corrugation amplitude as a function of energy, obtained from the data in Fig. 7.3. For energies near the Fermi-level, we find large values for the corrugation amplitude characteristic of localization in 2-dimensions.[82] Below E_F the corrugation remains relatively large, but for energies more than 30 meV above E_F, its amplitude decreases to below 40%. This is an indication of delocalization at higher energies, consistent with the diffuse features in the *dI/dV* map of Fig. 7.3D.

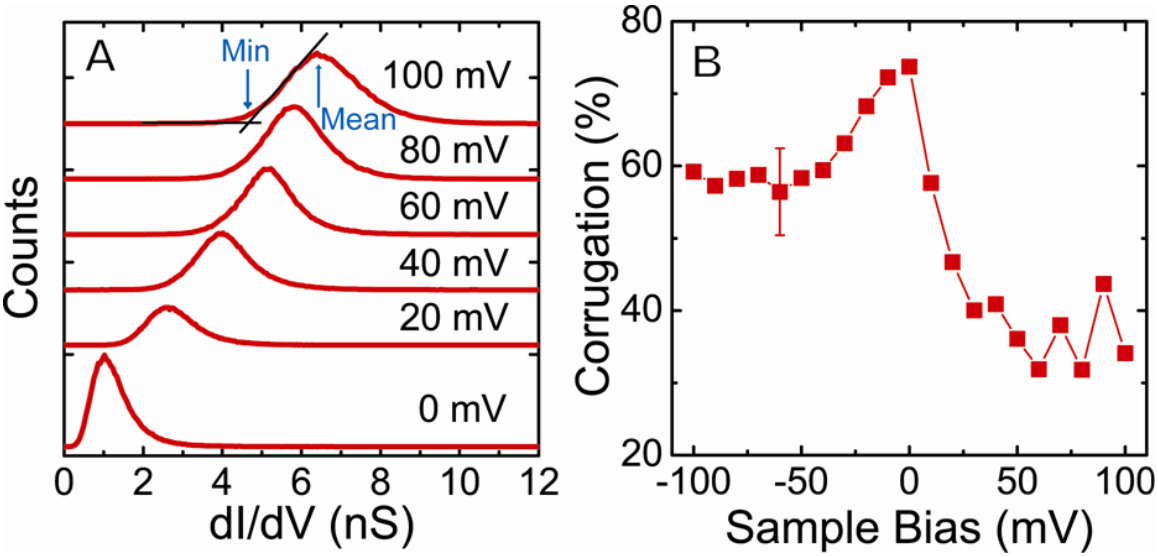

Figure 7.8

(A) Histograms of conductance values for the data set in Fig. 7.3 at selected values of the sample bias. The method for determining the minimum value of conductance is shown by the intersection of the two lines. Curves are offset for clarity. (B) Corresponding conductance corrugation $(dI/dV_{MEAN}-dI/dV_{MIN})/(dI/dV_{MEAN})$ in the *dI/dV* maps as a function of sample bias.

The identification of localized resonances that are tied to the interference maxima raises the question as to whether the observed states are related to weak localization, which is the self-interference of scattered waves along a connected path of random scatterers.[47] To answer this question, the quasiparticle lifetime has to be estimated from the energy-time uncertainty principle. Using the equation for the lifetime, $\tau_\varphi \approx \hbar/(\Delta E)$, combined with an estimated energy-width ($\Delta E \sim 5$ meV) of the *dI/dV* peaks in Fig. 7.4 implies a quasiparticle lifetime of $\tau_\varphi \approx 0.1$ ps. The well-defined standing wave patterns indicate that the defects scatter elastically, so we estimate the elastic mean free path from kinetic theory. The mean free path of a particle is defined as $l_e = (n\sigma)^{-1}$, where n is the defect density and σ is the scattering cross section.[266] In electronic transport of two dimensional electron systems, the cross section can be approximated as the particle Fermi wavelength, λ_F. For our epitaxial graphene samples $n \approx 0.01\ \mathrm{nm}^{-2}$ (≈ 25 type II defects

in a 50 nm x 50 nm area) and $\lambda_F \approx 2\pi\hbar v_F / E_F \approx 14\,\text{nm}$, which equates to an elastic mean free path of $l_e \approx 7$ nm. Using this value, we can now determine the elastic scattering time, $\tau_e \approx l_e / v_F \approx 7$ fs. In the diffusive limit, the coherence or phase-relaxation length (limited by inelastic scattering) is $l_\varphi = \sqrt{(D\tau_\varphi)} \approx 22$ nm, where $D = v_F{}^2 \tau_e / 2$ is the diffusion constant.[267] This coherence length is somewhat smaller, but of the same order, as that obtained from the analysis of weak-localization in magnetotransport on a similar sample.[47] STS peaks very close to E_F, where peaks are seen with even smaller widths (approaching the temperature resolution limit), will have still larger coherence lengths.

Direct spectroscopic indications of weak localization in the tunneling spectra are the substantially increased corrugation within ± 20 meV of E_F (Fig. 7.8), and the reduced density of states near E_F that we observe in the conductance spectra (Fig. 7.4). It is clear from the scattering analysis that the band-structure density of states has no energy gap at E_F; it increases monotonically. Therefore we believe that the persistent dip in the *dI/dV* spectra is a consequence of weak localization, for which a logarithmic suppression of the density of states at E_F is expected.[268] Still, a clear indication of weak localization requires further definitive measurements in a magnetic field to alter the phase coherence.

7.4 Conclusion

In this chapter, I discussed the role of defects on the electronic properties of single-layer and bilayer graphene. It was found that subsurface defects (type I) scatter carriers weakly as compared to the defects that originate in the graphene plane (type II). Differential conductance maps show scattering on two different length scales. The different length scales are related to the two families of allowed scattering vectors in graphene, either inter- or intra-valley scattering. We have found that the in-plane lattice defects cause both types of scattering. From the dI/dV maps we were able to extract the

Fermi velocity and Dirac-point position for epitaxial graphene, which showed agreement with ARPES measurements. Finally, we proposed a connection between weak localization and the scattering patterns.

For perfect monolayer graphene, the lattice A-B site symmetry and the $\mathbf{K}_{\pm}$ valley symmetry give rise to wavefunctions with distinct values of pseudospin and chirality.[154-156] Both quantities are tied directly to the group velocity of the quasiparticle wavefunction. Their near-conservation in the presence of weak potentials is equivalent to a suppression of backscattering. Our measurements of both $\mathbf{q}_1$ and $\mathbf{q}_2$ scattering processes show very directly that in-plane atomic defects are a dominant source of both intravalley (pseudospin-flip) and intervalley (chirality-reversal) backscattering. This may explain the observation of weak localization observed in similar samples.[47] We note that the related phenomenon of weak anti-localization was confirmed in epitaxial graphene grown by a different method on carbon-terminated $SiC(000\bar{1})$ substrates,[179] indicating a very low density of in-plane atomic scattering centers in those samples. Thus transport properties in epitaxial graphene are critically influenced by microscopic properties of the sample, determined (at least) by the substrate and growth conditions. For carbon-based electronics, this work highlights the need for further microscopic studies that are correlated closely with macroscopic transport measurements.

CHAPTER 8

CLOSING REMARKS

Two-dimensional electron systems have been of interest to scientists for many years. From high-electron mobility transistors to novel topological quasiparticles of the fractional quantum Hall effect, the field continues to be rich in scientific possibilities and technological pay-offs. To date, most high-mobility 2D electron systems have been created at an interface between materials, making them inaccessible to the electron spectroscopies of surface science. Here I have investigated graphene, a new 2D electron system that is available for such surface electron spectroscopies. Our measurements have used cryogenic (LT) and room temperature (RT) scanning tunneling microscopy (STM) and spectroscopy (STS) to elucidate the electronic properties of epitaxial graphene grown on silicon carbide, resolving heterogeneities at the level of single atoms. In particular, this work focused on the growth mechanisms, as well as the structural and electronic characteristics of graphene films on SiC(0001) substrates.

Utilizing a RT-STM, I was able to investigate different growth mechanisms of epitaxial graphene on SiC. As a result, I determined that the prevalent type of graphene formation is terrace growth that protrudes from SiC bulk step edges. A smaller percentage of graphene forms in small nanoislands on the surface. Different features in the spectroscopy are shown to occur between the graphene terraces, graphene nanoislands, and the SiC reconstruction, which are indicative of the particular growth regime. The STS spectrum from the SiC reconstruction showed dangling bond states in the bulk band gap of SiC. Investigation of the dangling bonds states was successful by characterizing the SiC reconstruction adatoms in chemical composition and structure. As a result of this study, we were able to effectively passivate the dangling bonds with atomic hydrogen, which offers insight into their chemical composition. Finally, hydrogen was found to adhere to single-layer graphene, and it was shown that the

hydrogen changes the local electronic structure of the graphene in the vicinity of the absorption site. The adsorption of hydrogen to graphene is a viable candidate for hydrogen storage in the field of renewable energy.

Understanding the interface properties is important for future epitaxial graphene applications, since the interface's role is still unclear in the electronic transport. Using low temperature STM topographic images, I was able to investigate the interface structure below a single layer of epitaxial graphene. Such imaging is possible because graphene appears transparent at energies of ±1 eV above or below the Fermi energy. A theoretical analysis of calculations based on density-functional theory showed how this transparency arises from the electronic structure of a graphene layer on a SiC substrate. In addition, I showed that the interface structures were made up of adatoms of the bare SiC reconstruction. We feel it is possible to passivate these dangling bond states underneath the graphene similarly to the passivated bare SiC. This would potentially decouple the graphene from the substrate, but further experiments are needed to see this effect.

LT-STM imaging also made it possible to characterize the stacking of multilayer epitaxial graphene on SiC(0001). I showed that a bias dependence occurs when both sublattices of graphene (identical for single layer) become distinguishable due to stacking of two or more layers. We were able to verify that the images of these structures are consistent with those for Bernal (ABAB) stacking, as found in the most common form of graphite. A quantitative analysis can be made by measuring the apparent height difference between atoms on the two sublattices and comparing to theoretical estimates. These findings provide a unique determination of the graphene stacking sequence, an important characteristic due to its influence on the electronic properties.

Finally, I further investigated key electronic characteristics of epitaxial graphene via STS conductance maps. Conductance maps are, essentially, high spatial resolution energy-resolved pictures of the local density of states. We were able to determine that

atomic-scale lattice defects scatter electrons very strongly, which is not the case for interface subsurface defects. In the quasiparticle interference patterns, we observed modulations on two different length scales, reflecting both intravalley and intervalley scattering. Although such scattering should be suppressed because of the symmetries of the Dirac quasiparticles, I showed that wave functions can mix when the scattering source is due to atomic-scale lattice defects. Moreover, such scattering allows for a determination of the allowed scattering wave vectors. When plotting a curve of the energy versus wave vectors, I was able to calculate Fermi velocity and the zero energy reference, values consistent with previous research on similar samples.

This research provides further information about the electronic and structural properties of epitaxial graphene and suggests that its transport properties are critically influenced by the microscopic properties of the sample, determined by the substrate and growth conditions. The results of our studies can be used to further investigate the potential of graphene devices for microelectronic applications. For the future of carbon-based electronics, there is a need for continuing microscopic studies that are correlated closely with macroscopic transport measurements.

REFERENCES

1. R. E. Smalley, "Discovering the fullerenes." *Reviews of Modern Physics* **69**, 723-730 (1997).

2. G. E. Moore, "Cramming More Components onto Integrated Circuits." *Electronics* **38**, 114-1 (1965).

3. E. Mollick, "Establishing Moore's law." *IEEE Annals of the History of Computing* **28**, 62-75 (2006).

4. M. T. Bohr, "Nanotechnology goals and challenges for electronic applications." *IEEE Transactions on Nanotechnology* **1**, 56-62 (2002).

5. M. Lundstrom, "Moore's law forever?" *Science* **299**, 210-211 (2003).

6. H. S. P. Wong, D. J. Frank, P. M. Solomon, C. H. J. Wann & J. J. Welser, "Nanoscale CMOS." *Proceedings of the IEEE* **87**, 537-570 (1999).

7. J. R. Powell, "The quantum limit to Moore's law." *Proceedings of the IEEE* **96**, 1247-1248 (2008).

8. S. E. Thompson & S. Parthasarathy, "Moore's law: the future of Si microelectronics." *Materials Today* **9**, 20-25 (2006).

9. S. E. Thompson *et al.*, "In search of 'forever,' continued transistor scaling one new material at a time." *IEEE Transactions on Semiconductor Manufacturing* **18**, 26-36 (2005).

10. R. Chau *et al.*, "Benchmarking nanotechnology for high-performance and low-power logic transistor applications." *IEEE Transactions on Nanotechnology* **4**, 153-158 (2005).

11. R. K. Cavin, V. V. Zhirnov, D. J. C. Herr, A. Avila & J. Hutchby, "Research directions and challenges in nanoelectronics." *Journal of Nanoparticle Research* **8**, 841-858 (2006).

12. S. A. Wolf *et al.*, "Spintronics: A spin-based electronics vision for the future." *Science* **294**, 1488-1495 (2001).

13. P. Avouris, Z. H. Chen & V. Perebeinos, "Carbon-based electronics." *Nature Nanotechnology* **2**, 605-615 (2007).

14. Dresselhaus, M. S., Dresselhaus, G. & Eklund, P. C. *Science of Fullerenes and Carbon Nanotubes: Their Properties and Applications*. Academic, New York (1996).

15. A. K. Geim & P. Kim, "Carbon wonderland." *Scientific American* **298**, 90-97 (2008).

16. A. K. Geim & K. S. Novoselov, "The rise of graphene." *Nature Materials* **6**, 183-191 (2007).

17. M. I. Katsnelson, "Graphene: carbon in two dimensions." *Materials Today* **10**, 20-27 (2006).

18. K. S. Novoselov *et al.*, "Electric field effect in atomically thin carbon films." *Science* **306**, 666-669 (2004).

19. Saito, R., Dresselhaus, G. & Dresselhaus, M. S. *Physical Properties of Carbon Nanotubes*. Imperial College Press, London (1998).

20. C. Lee, X. D. Wei, J. W. Kysar & J. Hone, "Measurement of the elastic properties and intrinsic strength of monolayer graphene." *Science* **321**, 385-388 (2008).

21. D. D. L. Chung, "Review graphite." *Journal of Materials Science* **37**, 1475-1489 (2002).

22. H. W. Kroto, A. W. Allaf & S. P. Balm, "C60 - Buckminsterfullerene." *Chemical Reviews* **91**, 1213-1235 (1991).

23. H. W. Kroto, J. R. Heath, S. C. Obrien, R. F. Curl & R. E. Smalley, "C-60 - Buckminsterfullerene." *Nature* **318**, 162-163 (1985).

24. W. Krätchmer, L. D. Lamb, K. Fostiropoulos & D. R. Huffman, "Solid C-60 - A New Form of Carbon." *Nature* **347**, 354-358 (1990).

25. E. Osawa, "The Evolution of the Football Structure for the C-60 Molecule - A Retrospective." *Philosophical Transactions of the Royal Society A-Mathematical Physical and Engineering Sciences* **343**, 1-8 (1993).

26. M. Prato, "[60] Fullerene chemistry for materials science applications." *Journal of Materials Chemistry* **7**, 1097-1109 (1997).

27. R. H. Baughman, A. A. Zakhidov & W. A. de Heer, "Carbon nanotubes - the route toward applications." *Science* **297**, 787-792 (2002).

28. S. Iijima, "Helical Microtubules of Graphitic Carbon." *Nature* **354**, 56-58 (1991).

29. S. Iijima & T. Ichihashi, "Single-Shell Carbon Nanotubes of 1-Nm Diameter." *Nature* **363**, 603-605 (1993).

30. D. S. Bethune *et al.*, "Cobalt-Catalyzed Growth of Carbon Nanotubes with Single-Atomic-Layerwalls." *Nature* **363**, 605-607 (1993).

31. A. Thess *et al.*, "Crystalline ropes of metallic carbon nanotubes." *Science* **273**, 483-487 (1996).

32. N. Hamada, S. Sawada & A. Oshiyama, "New One-Dimensional Conductors - Graphitic Microtubules." *Physical Review Letters* **68**, 1579-1581 (1992).

33. J. W. Mintmire, B. I. Dunlap & C. T. White, "Are Fullerene Tubules Metallic." *Physical Review Letters* **68**, 631-634 (1992).

34. R. Saito, M. Fujita, G. Dresselhaus & M. S. Dresselhaus, "Electronic-Structure of Graphene Tubules Based on C-60." *Physical Review B* **46**, 1804-1811 (1992).

35. R. Saito, M. Fujita, G. Dresselhaus & M. S. Dresselhaus, "Electronic-Structure of Chiral Graphene Tubules." *Applied Physics Letters* **60**, 2204-2206 (1992).

36. T. W. Odom, J. L. Huang, P. Kim & C. M. Lieber, "Atomic structure and electronic properties of single-walled carbon nanotubes." *Nature* **391**, 62-64 (1998).

37. J. W. G. Wildöer, L. C. Venema, A. G. Rinzler, R. E. Smalley & C. Dekker, "Electronic structure of atomically resolved carbon nanotubes." *Nature* **391**, 59-62 (1998).

38. S. J. Tans *et al.*, "Individual single-wall carbon nanotubes as quantum wires." *Nature* **386**, 474-477 (1997).

39. S. Frank, P. Poncharal, Z. L. Wang & W. A. de Heer, "Carbon nanotube quantum resistors." *Science* **280**, 1744-1746 (1998).

40. W. J. Liang *et al.*, "Fabry-Perot interference in a nanotube electron waveguide." *Nature* **411**, 665-669 (2001).

41. R. Martel, T. Schmidt, H. R. Shea, T. Hertel & P. Avouris, "Single- and multi-wall carbon nanotube field-effect transistors." *Applied Physics Letters* **73**, 2447-2449 (1998).

42. S. J. Tans, A. R. M. Verschueren & C. Dekker, "Room-temperature transistor based on a single carbon nanotube." *Nature* **393**, 49-52 (1998).

43. A. Bachtold, P. Hadley, T. Nakanishi & C. Dekker, "Logic circuits with carbon nanotube transistors." *Science* **294**, 1317-1320 (2001).

44. V. Derycke, R. Martel, J. Appenzeller & P. Avouris, "Carbon nanotube inter- and intramolecular logic gates." *Nano Letters* **1**, 453-456 (2001).

45. P. G. Collins & P. Avouris, "Nanotubes for electronics." *Scientific American* **283**, 62-69 (2000).

46. P. Avouris, "Molecular electronics with carbon nanotubes." *Accounts of Chemical Research* **35**, 1026-1034 (2002).

47. C. Berger *et al.*, "Ultrathin epitaxial graphite: 2D electron gas properties and a route toward graphene-based nanoelectronics." *Journal of Physical Chemistry B* **108**, 19912-19916 (2004).

48. M. Fujita, K. Wakabayashi, K. Nakada & K. Kusakabe, "Peculiar localized state at zigzag graphite edge." *Journal of the Physical Society of Japan* **65**, 1920-1923 (1996).

49. K. Nakada, M. Fujita, G. Dresselhaus & M. S. Dresselhaus, "Edge state in graphene ribbons: Nanometer size effect and edge shape dependence." *Physical Review B* **54**, 17954-17961 (1996).

50. A. K. Geim & A. H. MacDonald, "Graphene: Exploring carbon flatland." *Physics Today* **60**, 35-41 (2007).

51. X. L. Li, X. R. Wang, L. Zhang, S. W. Lee & H. J. Dai, "Chemically derived, ultrasmooth graphene nanoribbon semiconductors." *Science* **319**, 1229-1232 (2008).

52. W. A. de Heer *et al.*, "Epitaxial graphene." *Solid State Communications* **143**, 92-100 (2007).

53. G. Binnig & H. Rohrer, "In touch with atoms." *Reviews of Modern Physics* **71**, S324-S330 (1999).

54. G. Binnig & H. Rohrer, "Scanning Tunneling Microscopy - from Birth to Adolescence." *Reviews of Modern Physics* **59**, 615-625 (1987).

55. R. J. Colton, "Nanoscale measurements and manipulation." *Journal of Vacuum Science & Technology B* **22**, 1609-1635 (2004).

56. Stroscio, J. A. & Kaiser, W. *Scanning Tunneling Microscopy*. Academic Press Inc., (1993).

57. Griffiths, D. J. *Introduction to Quantum Mechanics*. Prentice-Hall, Upper Saddle River, NJ (1995).

58. J. Bardeen, "Tunnelling from A Many-Particle Point of View." *Physical Review Letters* **6**, 57-& (1961).

59. G. Binnig & H. Rohrer, "Scanning Tunneling Microscopy." *Ibm Journal of Research and Development* **30**, 355-369 (1986).

60. N. D. Lang, "Theory of Single-Atom Imaging in the Scanning Tunneling Microscope." *Physical Review Letters* **56**, 1164-1167 (1986).

61. G. Binnig, H. Rohrer, C. Gerber & E. Weibel, "Tunneling Through A Controllable Vacuum Gap." *Applied Physics Letters* **40**, 178-180 (1982).

62. R. J. Hamers, "Atomic-Resolution Surface Spectroscopy with the Scanning Tunneling Microscope." *Annual Review of Physical Chemistry* **40**, 531-559 (1989).

63. N. D. Lang, "Spectroscopy of Single Atoms in the Scanning Tunneling Microscope." *Physical Review B* **34**, 5947-5950 (1986).

64. J. A. Stroscio, R. M. Feenstra & A. P. Fein, "Electronic-Structure of the Si(111)-2 x 1 Surface by Scanning-Tunneling Microscopy." *Physical Review Letters* **57**, 2579-2582 (1986).

65. J. A. Golovchenko, "The Tunneling Microscope - A New Look at the Atomic World." *Science* **232**, 48-53 (1986).

66. G. Binnig, H. Rohrer, C. Gerber & E. Weibel, "7 x 7 Reconstruction on Si(111) Resolved in Real Space." *Physical Review Letters* **50**, 120-123 (1983).

67. D. E. Eastman, "Geometrical and Electronic-Structure of Si(001) and Si(111) Surfaces - A Status-Report." *Journal of Vacuum Science & Technology* **17**, 492-500 (1980).

68. K. Takayanagi, Y. Tanishiro, M. Takahashi & S. Takahashi, "Structural-Analysis of Si(111)-7 x 7 by UHV-Transmission Electron-Diffraction and Microscopy." *Journal of Vacuum Science & Technology A-Vacuum Surfaces and Films* **3**, 1502-1506 (1985).

69. F. Besenbacher, "Scanning tunnelling microscopy studies of metal surfaces." *Reports on Progress in Physics* **59**, 1737-1802 (1996).

70. J. Tersoff & D. R. Hamann, "Theory of the Scanning Tunneling Microscope." *Physical Review B* **31**, 805-813 (1985).

71. G. Binnig & H. Rohrer, "Scanning Tunneling Microscopy." *Surface Science* **126**, 236-244 (1983).

72. R. M. Tromp, "Spectroscopy with the Scanning Tunneling Microscope - A Critical-Review." *Journal of Physics-Condensed Matter* **1**, 10211-10228 (1989).

73. R. S. Becker, J. A. Golovchenko, D. R. Hamann & B. S. Swartzentruber, "Real-Space Observation of Surface-States on Si(111)-7 x 7 with the Tunneling Microscope." *Physical Review Letters* **55**, 2032-2034 (1985).

74. R. M. Feenstra, J. A. Stroscio, J. Tersoff & A. P. Fein, "Atom-Selective Imaging of the GaAs(110) Surface." *Physical Review Letters* **58**, 1192-1195 (1987).

75. R. M. Feenstra, W. A. Thompson & A. P. Fein, "Real-Space Observation of Pi-Bonded Chains and Surface Disorder on Si(111)-2 x 1." *Physical Review Letters* **56**, 608-611 (1986).

76. L. Bartels, G. Meyer & K. H. Rieder, "Controlled vertical manipulation of single CO molecules with the scanning tunneling microscope: A route to chemical contrast." *Applied Physics Letters* **71**, 213-215 (1997).

77. M. F. Crommie, C. P. Lutz & D. M. Eigler, "Imaging Standing Waves in A 2-Dimensional Electron-Gas." *Nature* **363**, 524-527 (1993).

78. Y. Hasegawa & P. Avouris, "Direct Observation of Standing-Wave Formation at Surface Steps Using Scanning Tunneling Spectroscopy." *Physical Review Letters* **71**, 1071-1074 (1993).

79. R. J. Hamers, R. M. Tromp & J. E. Demuth, "Surface Electronic-Structure of Si(111)-(7 x 7) Resolved in Real Space." *Physical Review Letters* **56**, 1972-1975 (1986).

80. L. Petersen, P. Hofmann, E. W. Plummer & F. Besenbacher, "Fourier transform-STM: determining the surface Fermi contour." *Journal of Electron Spectroscopy and Related Phenomena* **109**, 97-115 (2000).

81. J. E. Hoffman *et al.*, "Imaging quasiparticle interference in $Bi_2Sr_2CaCu_2O_{8+ä}$." *Science* **297**, 1148-1151 (2002).

82. M. Morgenstern *et al.*, "Direct comparison between potential landscape and local density of states in a disordered two-dimensional electron system." *Physical Review Letters* **89**, 136806 (2002).

83. J. A. Stroscio & D. M. Eigler, "Atomic and Molecular Manipulation with the Scanning Tunneling Microscope." *Science* **254**, 1319-1326 (1991).

84. D. M. Eigler & E. K. Schweizer, "Positioning Single Atoms with A Scanning Tunneling Microscope." *Nature* **344**, 524-526 (1990).

85. Ø. Fischer *et al.*, "Scanning tunneling spectroscopy of high-temperature superconductors." *Reviews of Modern Physics* **79**, 353-419 (2007).

86. Morgenstern, M. Probing the Local Density of States of Dilute Electron Systems in Different Dimensions. Habilitation University of Hamburg (2002).

87. S. H. Pan, E. W. Hudson & J. C. Davis, "He-3 refrigerator based very low temperature scanning tunneling microscope." *Review of Scientific Instruments* **70**, 1459-1463 (1999).

88. P. N. First, J. A. Stroscio, D. T. Pierce, R. A. Dragoset & R. J. Celotta, "A System for the Study of Magnetic-Materials and Magnetic Imaging with the Scanning

Tunneling Microscope." *Journal of Vacuum Science & Technology B* **9**, 531-536 (1991).

89. P. Martensson, F. Owman & L. I. Johansson, "Morphology, atomic and electronic structure of 6H-SiC(0001) surfaces." *Physica Status Solidi B-Basic Research* **202**, 501-528 (1997).

90. J. Hass *et al.*, "Highly ordered graphene for two dimensional electronics." *Applied Physics Letters* **89**, 143106 (2006).

91. N. P. Guisinger *et al.*, "The Atomic-Scale Investigation of Graphene Formation on 6H-SiC(0001)." *Journal of Vacuum Science & Technology A* **26**, 932 (2007).

92. Tianbo Li. Characteristics of Graphite Films on Silicon-and Carbon-Terminated Faces of Silicon Carbide. Ph.D.Thesis Georgia Institute of Technology (2006).

93. I. Forbeaux, J. M. Themlin & J. M. Debever, "Heteroepitaxial graphite on 6H-SiC(0001): Interface formation through conduction-band electronic structure." *Physical Review B* **58**, 16396-16406 (1998).

94. Landau L.D. & Lifshitz E.M. *Statistical Physics*. Pergamon Press Inc., London (1958).

95. N. D. Mermin, "Crystalline Order in Two Dimensions." *Physical Review* **176**, 250-& (1968).

96. J. M. Kosterlitz & D. J. Thouless, "Ordering, Metastability and Phase-Transitions in Two-Dimensional Systems." *Journal of Physics C-Solid State Physics* **6**, 1181-1203 (1973).

97. J. C. Meyer *et al.*, "The structure of suspended graphene sheets." *Nature* **446**, 60-63 (2007).

98. K. S. Novoselov *et al.*, "Two-dimensional gas of massless Dirac fermions in graphene." *Nature* **438**, 197-200 (2005).

99. Y. B. Zhang, Y. W. Tan, H. L. Stormer & P. Kim, "Experimental observation of the quantum Hall effect and Berry's phase in graphene." *Nature* **438**, 201-204 (2005).

100. A. C. Ferrari *et al.*, "Raman spectrum of graphene and graphene layers." *Physical Review Letters* **97**, (2006).

101. D. Graf *et al.*, "Spatially resolved Raman spectroscopy of single- and few-layer graphene." *Nano Letters* **7**, 238-242 (2007).

102. Ashcroft, N. & Mermin, N. *Solid State Physics*. Brooks Cole, London (1976).

103. R. Joynt & R. E. Prange, "Conditions for the Quantum Hall-Effect." *Physical Review B* **29**, 3303-3317 (1984).

104. K. von Klitzing, G. Dorda & M. Pepper, "New Method for High-Accuracy Determination of the Fine-Structure Constant Based on Quantized Hall Resistance." *Physical Review Letters* **45**, 494-497 (1980).

105. K. von Klitzing, "The Quantized Hall-Effect." *Reviews of Modern Physics* **58**, 519-531 (1986).

106. R. B. Laughlin, "Quantized Hall Conductivity in Two Dimensions." *Physical Review B* **23**, 5632-5633 (1981).

107. T. Ando, A. B. Fowler & F. Stern, "Electronic-Properties of Two-Dimensional Systems." *Reviews of Modern Physics* **54**, 437-672 (1982).

108. R. B. Laughlin, "Nobel Lecture: Fractional quantization." *Reviews of Modern Physics* **71**, 863-874 (1999).

109. H. L. Stormer, "Nobel Lecture: The fractional quantum Hall effect." *Reviews of Modern Physics* **71**, 875-889 (1999).

110. D. C. Tsui, "Nobel Lecture: Interplay of disorder and interaction in two-dimensional electron gas in intense magnetic fields." *Reviews of Modern Physics* **71**, 891-895 (1999).

111. K. S. Novoselov *et al.*, "Unconventional quantum Hall effect and Berry's phase of 2Pi in bilayer graphene." *Nature Physics* **2**, 177-180 (2006).

112. Y. W. Tan *et al.*, "Measurement of scattering rate and minimum conductivity in graphene." *Physical Review Letters* **99**, (2007).

113. J. H. Chen, C. Jang, S. D. Xiao, M. Ishigami & M. S. Fuhrer, "Intrinsic and extrinsic performance limits of graphene devices on SiO_2." *Nature Nanotechnology* **3**, 206-209 (2008).

114. S. V. Morozov *et al.*, "Giant intrinsic carrier mobilities in graphene and its bilayer." *Physical Review Letters* **100**, (2008).

115. K. Ismail, M. Arafa, K. L. Saenger, J. O. Chu & B. S. Meyerson, "Extremely High-Electron-Mobility in Si/SiGe Modulation-Doped Heterostructures." *Applied Physics Letters* **66**, 1077-1079 (1995).

116. L. Pfeiffer, K. W. West, H. L. Stormer & K. W. Baldwin, "Electron Mobilities Exceeding 10^7 cm^2/Vs in Modulation-Doped GaAs." *Applied Physics Letters* **55**, 1888-1890 (1989).

117. K. I. Bolotin *et al.*, "Ultrahigh electron mobility in suspended graphene." *Solid State Communications* **146**, 351-355 (2008).

118. X. Du, I. Skachko, A. Barker & E. Y. Andrei, "Approaching ballistic transport in suspended graphene." *Nature Nanotechnology* **3**, 491-495 (2008).

119. K. S. Novoselov *et al.*, "Room-temperature quantum hall effect in graphene." *Science* **315**, 1379 (2007).

120. Nishi Y. *Handbook of Semiconducting Manufacturing Technology*. Marcel Dekker, Inc., New York (2000).

121. C. Berger *et al.*, "Electronic confinement and coherence in patterned epitaxial graphene." *Science* **312**, 1191-1196 (2006).

122. M. Orlita *et al.*, "Approaching the Dirac point in ultrahigh mobility multilayered epitaxial graphene." *arXiv:0808. 3661v1* (2008).

123. M. Y. Han, B. Ozyilmaz, Y. B. Zhang & P. Kim, "Energy band-gap engineering of graphene nanoribbons." *Physical Review Letters* **98**, (2007).

124. L. A. Ponomarenko *et al.*, "Chaotic Dirac billiard in graphene quantum dots." *Science* **320**, 356-358 (2008).

125. X. R. Wang *et al.*, "Room-temperature all-semiconducting sub-10-nm graphene nanoribbon field-effect transistors." *Physical Review Letters* **100**, (2008).

126. D. L. Critchlow, "MOSFET scaling - The driver of VLSI technology." *Proceedings of the IEEE* **87**, 659-667 (1999).

127. Wolf S. *Silicon Processing for the VLSI Era*. Lattice Press, Sunset Beach, CA (1990).

128. M. C. Lemme, T. J. Echtermeyer, M. Baus & H. Kurz, "A graphene field-effect device." *IEEE Electron Device Letters* **28**, 282-284 (2007).

129. B. Huard *et al.*, "Transport measurements across a tunable potential barrier in graphene." *Physical Review Letters* **98**, (2007).

130. B. Ozyilmaz *et al.*, "Electronic transport and quantum hall effect in bipolar graphene p-n-p junctions." *Physical Review Letters* **99**, (2007).

131. J. R. Williams, L. DiCarlo & C. M. Marcus, "Quantum hall effect in a gate-controlled p-n junction of graphene." *Science* **317**, 638-641 (2007).

132. A. Das *et al.*, "Monitoring dopants by Raman scattering in an electrochemically top-gated graphene transistor." *Nature Nanotechnology* **3**, 210-215 (2008).

133. T. J. Echtermeyer *et al.*, "Nonvolatile switching in graphene field-effect devices." *IEEE Electron Device Letters* **29**, 952-954 (2008).

134. X. S. Wu *et al.*, "Epitaxial-graphene/graphene-oxide junction: An essential step towards epitaxial graphene electronics." *Physical Review Letters* **101**, (2008).

135. Kedzierski J. *et al.*, "Epitaxial graphene transistors on SiC substrates." *IEEE Transactions on Electron Devices* **55**, 2078 (2008).

136. F. Schedin *et al.*, "Detection of individual gas molecules adsorbed on graphene." *Nature Materials* **6**, 652-655 (2007).

137. J. H. Chen *et al.*, "Charged-impurity scattering in graphene." *Nature Physics* **4**, 377-381 (2008).

138. J. C. Meyer, C. O. Girit, M. F. Crommie & A. Zettl, "Imaging and dynamics of light atoms and molecules on graphene." *Nature* **454**, 319-322 (2008).

139. R. R. Nair *et al.*, "Fine structure constant defines visual transparency of graphene." *Science* **320**, 1308 (2008).

140. P. R. Wallace, "The Band Theory of Graphite." *Physical Review* **71**, 622-634 (1947).

141. J. C. Slonczewski & P. R. Weiss, "Band Structure of Graphite." *Physical Review* **109**, 272-279 (1958).

142. G. S. Painter & D. E. Ellis, "Electronic Band Structure and Optical Properties of Graphite from A Variational Approach." *Physical Review B* **1**, 4747-& (1970).

143. K. S. Novoselov, "Mind the gap." *Nature Materials* **6**, 720-721 (2007).

144. J. C. Charlier, X. Blase & S. Roche, "Electronic and transport properties of nanotubes." *Reviews of Modern Physics* **79**, 677-732 (2007).

145. N. M. R. Peres, F. Guinea & A. H. C. Neto, "Electronic properties of disordered two-dimensional carbon." *Physical Review B* **73**, (2006).

146. E. Rolling *et al.*, "Synthesis and characterization of atomically thin graphite films on a silicon carbide substrate." *Journal of Physics and Chemistry of Solids* **67**, 2172-2177 (2006).

147. S. Y. Zhou *et al.*, "Substrate-induced bandgap opening in epitaxial graphene." *Nature Materials* **6**, 770-775 (2007).

148. A. Bostwick, T. Ohta, T. Seyller, K. Horn & E. Rotenberg, "Quasiparticle dynamics in graphene." *Nature Physics* **3**, 36-40 (2007).

149. E. Rotenberg *et al.*, "Origin of the energy bandgap in epitaxial graphene." *Nature Materials* **7**, 258-259 (2008).

150. S. Y. Zhou *et al.*, "Origin of the energy bandgap in epitaxial graphene - Reply." *Nature Materials* **7**, 259-260 (2008).

151. S. Reich, J. Maultzsch, C. Thomsen & P. Ordejon, "Tight-binding description of graphene." *Physical Review B* **66**, (2002).

152. T. Ando, "Exotic electronic and transport properties of graphene." *Physica E-Low-Dimensional Systems & Nanostructures* **40**, 213-227 (2007).

153. Hill J.E. "One-Dimensional Electron Systems on Graphene Edges.". Ph.D. Thesis The University of Texas at Austin (2007).

154. T. Ando, T. Nakanishi & R. Saito, "Berry's phase and absence of back scattering in carbon nanotubes." *Journal of the Physical Society of Japan* **67**, 2857-2862 (1998).

155. P. L. McEuen, M. Bockrath, D. H. Cobden, Y. G. Yoon & S. G. Louie, "Disorder, pseudospins, and backscattering in carbon nanotubes." *Physical Review Letters* **83**, 5098-5101 (1999).

156. E. McCann *et al.*, "Weak-localization magnetoresistance and valley symmetry in graphene." *Physical Review Letters* **97**, 146805 (2006).

157. A. H. Castro Neto, F. Guinea, N. M. R. Peres, K. S. Novoselov & A. K. Geim, "The electronic properties of graphene." *Reviews of Modern Physics* **in press**, (2008).

158. Y. W. Son, M. L. Cohen & S. G. Louie, "Energy gaps in graphene nanoribbons." *Physical Review Letters* **97**, (2006).

159. A. Rycerz, J. Tworzydlo & C. W. J. Beenakker, "Valley filter and valley valve in graphene." *Nature Physics* **3**, 172-175 (2007).

160. Y. Niimi *et al.*, "Scanning tunneling microscopy and spectroscopy of the electronic local density of states of graphite surfaces near monoatomic step edges." *Physical Review B* **73**, (2006).

161. E. McCann & V. I. Fal'ko, "Landau-level degeneracy and quantum hall effect in a graphite bilayer." *Physical Review Letters* **96**, 086805 (2006).

162. F. Guinea, A. H. Castro & N. M. R. Peres, "Electronic properties of stacks of graphene layers." *Solid State Communications* **143**, 116-122 (2007).

163. J. Nilsson, A. H. C. Neto, F. Guinea & N. M. R. Peres, "Electronic properties of graphene multilayers." *Physical Review Letters* **97**, 266801 (2006).

164. Z. F. Wang *et al.*, "Electronic structure of bilayer graphene: A real-space Green's function study." *Physical Review B* **75**, 085424 (2007).

165. J. M. B. Lopes dos Santos, N. M. R. Peres & A. H. Castro Neto, "Graphene bilayer with a twist: Electronic structure." *Physical Review Letters* **99**, (2007).

166. J. Hass *et al.*, "Why multilayer graphene on 4H-SiC(000-1) behaves like a single sheet of graphene." *Physical Review Letters* **100**, (2008).

167. S. Shallcross, S. Sharma & O. A. Pankratov, "Quantum interference at the twist boundary in graphene." *Physical Review Letters* **101**, (2008).

168. E. McCann, D. S. L. Abergel & V. I. Fal'ko, "Electrons in bilayer graphene." *Solid State Communications* **143**, 110-115 (2007).

169. E. A. Henriksen *et al.*, "Cyclotron resonance in bilayer graphene." *Physical Review Letters* **100**, (2008).

170. E. McCann, "Asymmetry gap in the electronic band structure of bilayer graphene." *Physical Review B* **74**, 161403(R) (2006).

171. H. Min, G. Borghi, M. Polini & A. H. MacDonald, "Pseudospin magnetism in graphene." *Physical Review B* **77**, (2008).

172. T. Ohta *et al.*, "Interlayer interaction and electronic screening in multilayer graphene investigated with angle-resolved photoemission spectroscopy." *Physical Review Letters* **98**, (2007).

173. T. Ohta, A. Bostwick, T. Seyller, K. Horn & E. Rotenberg, "Controlling the electronic structure of bilayer graphene." *Science* **313**, 951-954 (2006).

174. J. M. Pereira, F. M. Peeters & P. Vasilopoulos, "Landau levels and oscillator strength in a biased bilayer of graphene." *Physical Review B* **76**, (2007).

175. T. Ando & T. Nakanishi, "Impurity scattering in carbon nanotubes - Absence of back scattering." *Journal of the Physical Society of Japan* **67**, 1704-1713 (1998).

176. V. V. Cheianov & V. I. Fal'ko, "Friedel oscillations, impurity scattering, and temperature dependence of resistivity in graphene." *Physical Review Letters* **97**, (2006).

177. A. F. Morpurgo & F. Guinea, "Intervalley scattering, long-range disorder, and effective time-reversal symmetry breaking in graphene." *Physical Review Letters* **97**, (2006).

178. K. Nomura & A. H. MacDonald, "Quantum transport of massless Dirac fermions." *Physical Review Letters* **98**, (2007).

179. X. Wu, X. Li, Z. Song, C. Berger & W. A. de Heer, "Weak Anti-localization in Epitaxial Graphene: Evidence for Chiral Electrons." *Physical Review Letters* **98**, 136801 (2007).

180. C. Bena & S. A. Kivelson, "Quasiparticle scattering and local density of states in graphite." *Physical Review B* **72**, (2005).

181. G. M. Rutter *et al.*, "Scattering and interference in epitaxial graphene." *Science* **317**, 219-222 (2007).

182. C. Bena, "Effect of a single localized impurity on the local density of states in monolayer and bilayer graphene." *Physical Review Letters* **100**, (2008).

183. T. Pereg-Barnea & A. H. MacDonald, "Chiral quasiparticle local density of states maps in graphene." *Physical Review B* **78**, (2008).

184. A. J. van Bommel, J. E. Crombeen & A. Vantooren, "LEED and Auger-Electron Observations of SiC(0001) Surface." *Surface Science* **48**, 463-472 (1975).

185. U. Starke, J. Schardt & M. Franke, "Morphology, bond saturation and reconstruction of hexagonal SiC surfaces." *Applied Physics A-Materials Science & Processing* **65**, 587-596 (1997).

186. J. Hass, W. A. de Heer & E. H. Conrad, "The growth and morphology of epitaxial multilayer graphene." *Journal of Physics-Condensed Matter* **20**, (2008).

187. W. K. Burton, N. Cabrera & F. C. Frank, "The Growth of Crystals and the Equilibrium Structure of Their Surfaces." *Philosophical Transactions of the Royal Society of London Series A-Mathematical and Physical Sciences* **243**, 299-358 (1951).

188. J. V. Barth, G. Costantini & K. Kern, "Engineering atomic and molecular nanostructures at surfaces." *Nature* **437**, 671-679 (2005).

189. C. Riedl, U. Starke, J. Bernhardt, M. Franke & K. Heinz, "Structural properties of the graphene-SiC(0001) interface as a key for the preparation of homogeneous large-terrace graphene surfaces." *Physical Review B* **76**, (2007).

190. Z. Y. Zhang & M. G. Lagally, "Atomistic processes in the early stages of thin-film growth." *Science* **276**, 377-383 (1997).

191. G. Gu *et al.*, "Field effect in epitaxial graphene on a silicon carbide substrate." *Applied Physics Letters* **90**, 253507 (2007).

192. J. B. Hannon & R. M. Tromp, "Pit formation during graphene synthesis on SiC(0001): In situ electron microscopy." *Physical Review B* **77**, (2008).

193. V. Derycke, R. Martel, M. Radosvljevic, F. M. R. Ross & P. Avouris, "Catalyst-free growth of ordered single-walled carbon nanotube networks." *Nano Letters* **2**, 1043-1046 (2002).

194. P. Mallet *et al.*, "Electron states of mono- and bilayer graphene on SiC probed by scanning-tunneling microscopy." *Physical Review B* **76**, 041403(R) (2007).

195. P. L. Giunta & S. P. Kelty, "Direct observation of graphite layer edge states by scanning tunneling microscopy." *Journal of Chemical Physics* **114**, 1807-1812 (2001).

196. S. Okada, "Energetics of nanoscale graphene ribbons: Edge geometries and electronic structures." *Physical Review B* **77**, (2008).

197. Y. Kobayashi, K. Fukui, T. Enoki & K. Kusakabe, "Edge state on hydrogen-terminated graphite edges investigated by scanning tunneling microscopy." *Physical Review B* **73**, (2006).

198. V. W. Brar *et al.*, "Scanning tunneling spectroscopy of inhomogeneous electronic structure in monolayer and bilayer graphene on SiC." *Applied Physics Letters* **91**, (2007).

199. P. Lauffer *et al.*, "Atomic and electronic structure of few-layer graphene on SiC(0001) studied with scanning tunneling microscopy and spectroscopy." *Physical Review B* **77**, (2008).

200. J. Akola, H. P. Heiskanen & M. Manninen, "Edge-dependent selection rules in magic triangular graphene flakes." *Physical Review B* **77**, (2008).

201. M. Ezawa, "Graphene nanoribbon and graphene nanodisk." *Physica E-Low-Dimensional Systems & Nanostructures* **40**, 1421-1423 (2008).

202. K. A. Ritter & J. W. Lyding, "Characterization of nanometer-sized, mechanically exfoliated graphene on the H-passivated Si(100) surface using scanning tunneling microscopy." *Nanotechnology* **19**, (2008).

203. J. Akola, H. P. Heiskanen & M. Manninen, "Edge-dependent selection rules in magic triangular graphene flakes." *Physical Review B* **77**, (2008).

204. K. V. Emtsev *et al.*, "Initial stages of the graphite-SiC(001) interface formation studied by photoelectron spectroscopy." *Material Science Forum* **556-557**, 525 (2007).

205. K. V. Emtsev, F. Speck, T. Seyller, L. Ley & J. D. Riley, "Interaction, growth, and ordering of epitaxial graphene on SiC{0001} surfaces: A comparative photoelectron spectroscopy study." *Physical Review B* **77**, (2008).

206. A. Mattausch & O. Pankratov, "Ab initio study of graphene on SiC." *Physical Review Letters* **99**, (2007).

207. F. Varchon *et al.*, "Electronic structure of epitaxial graphene layers on SiC: Effect of the substrate." *Physical Review Letters* **99**, (2007).

208. S. Kim, J. Ihm, H. J. Choi & Y. W. Son, "Origin of anomalous electronic structures of epitaxial graphene on silicon carbide." *Physical Review Letters* **100**, (2008).

209. Mönch, W. *Semiconductor Surfaces and Interfaces*. Springer-Verlag, Berlin (1993).

210. U. Starke *et al.*, "Novel reconstruction mechanism for dangling-bond minimization: Combined method surface structure determination of SiC(111)-(3 x 3)." *Physical Review Letters* **80**, 758-761 (1998).

211. U. Starke, J. Schardt, J. Bernhardt, M. Franke & K. Heinz, "Stacking transformation from hexagonal to cubic SiC induced by surface reconstruction: A seed for heterostructure growth." *Physical Review Letters* **82**, 2107-2110 (1999).

212. W. Chen *et al.*, "Atomic structure of the 6H-SiC(0001) nanomesh." *Surface Science* **596**, 176-186 (2005).

213. W. J. Ong & E. S. Tok, "Role of Si clusters in the phase transformation and formation of (6 x 6)-ring structures on 6H-SiC(0001) as a function of temperature: An STM and XPS study." *Physical Review B* **73**, (2006).

214. G. M. Rutter *et al.*, "Imaging the interface of epitaxial graphene with silicon carbide via scanning tunneling microscopy." *Phys. Rev. B* **76**, 235416 (2007).

215. M. L. Green, E. P. Gusev, R. Degraeve & E. L. Garfunkel, "Ultrathin (< 4 nm) SiO_2 and Si-O-N gate dielectric layers for silicon microelectronics: Understanding the processing, structure, and physical and electrical limits." *Journal of Applied Physics* **90**, 2057-2121 (2001).

216. E. H. Poindexter, "MOS Interface States - Overview and Physicochemical Perspective." *Semiconductor Science and Technology* **4**, 961-969 (1989).

217. M. L. Reed & J. D. Plummer, "Chemistry of Si-SiO_2 Interface Trap Annealing." *Journal of Applied Physics* **63**, 5776-5793 (1988).

218. Y. T. Yeow, D. R. Lamb & S. D. Brotherton, "Investigation of Influence of Low-Temperature Annealing Treatments on Interface State Density at Si-SiO_2 Interface." *Journal of Physics D-Applied Physics* **8**, 1495-& (1975).

219. R. R. Razouk & B. E. Deal, "Dependence of Interface State Density on Silicon Thermal-Oxidation Process Variables." *Journal of the Electrochemical Society* **126**, 1573-1581 (1979).

220. E. Cartier, J. H. Stathis & D. A. Buchanan, "Passivation and Depassivation of Silicon Dangling Bonds at the Si/SiO_2 Interface by Atomic-Hydrogen." *Applied Physics Letters* **63**, 1510-1512 (1993).

221. Fowler, A. B. Process for the Elimination of Interface States in MIOS Structures. (3,849,2004). 1974.

222. A. G. Revesz, "Role of Hydrogen in SiO_2-Films on Silicon." *Journal of the Electrochemical Society* **126**, 122-130 (1979).

223. L. D. Thanh & P. Balk, "Elimination and Generation of $Si-SiO_2$ Interface Traps by Low-Temperature Hydrogen Annealing." *Journal of the Electrochemical Society* **135**, 1797-1801 (1988).

224. J. W. Lyding, K. Hess & I. C. Kizilyalli, "Reduction of hot electron degradation in metal oxide semiconductor transistors by deuterium processing." *Applied Physics Letters* **68**, 2526-2528 (1996).

225. J. S. Bunch *et al.*, "Impermeable atomic membranes from graphene sheets." *Nano Letters* **8**, 2458-2462 (2008).

226. M. C. Hersam, N. P. Guisinger, J. Lee, K. G. Cheng & J. W. Lyding, "Variable temperature study of the passivation of dangling bonds at Si(100)-2 x 1 reconstructed surfaces with H and D." *Applied Physics Letters* **80**, 201-203 (2002).

227. J. W. Lyding, T. C. Shen, J. S. Hubacek, J. R. Tucker & G. C. Abeln, "Nanoscale Patterning and Oxidation of H-Passivated Si(100)-2 x 1 Surfaces with An Ultrahigh-Vacuum Scanning Tunneling Microscope." *Applied Physics Letters* **64**, 2010-2012 (1994).

228. M. C. Hersam, N. P. Guisinger, J. W. Lyding, D. S. Thompson & J. S. Moore, "Atomic-level study of the robustness of the Si(100)-2 x 1 : H surface following exposure to ambient conditions." *Applied Physics Letters* **78**, 886-888 (2001).

229. K. Bobrov *et al.*, "Atomic-scale visualization and surface electronic structure of the hydrogenated diamond C(100)-(2 x 1): H surface." *Physical Review B* **68**, (2003).

230. J. Hass, J. E. Millan-Otoya, P. N. First & E. H. Conrad, "The interface structure of epitaxial graphene grown on 4H-SiC(0001)." *arXiv:0808. 1413v1* (2008).

231. T. N. Veziroglu & F. Barbir, "Hydrogen - the Wonder Fuel." *International Journal of Hydrogen Energy* **17**, 391-404 (1992).

232. L. Schlapbach & A. Zuttel, "Hydrogen-storage materials for mobile applications." *Nature* **414**, 353-358 (2001).

233. A. Midilli, M. Ay, I. Dincer & M. A. Rosen, "On hydrogen and hydrogen energy strategies I: current status and needs." *Renewable & Sustainable Energy Reviews* **9**, 255-271 (2005).

234. A. C. Dillon & M. J. Heben, "Hydrogen storage using carbon adsorbents: past, present and future." *Applied Physics A-Materials Science & Processing* **72**, 133-142 (2001).

235. A. Chambers, C. Park, R. T. K. Baker & N. M. Rodriguez, "Hydrogen storage in graphite nanofibers." *Journal of Physical Chemistry B* **102**, 4253-4256 (1998).

236. A. C. Dillon *et al.*, "Storage of hydrogen in single-walled carbon nanotubes." *Nature* **386**, 377-379 (1997).

237. H. M. Cheng, Q. H. Yang & C. Liu, "Hydrogen storage in carbon nanotubes." *Carbon* **39**, 1447-1454 (2001).

238. S. M. Lee & Y. H. Lee, "Hydrogen storage in single-walled carbon nanotubes." *Applied Physics Letters* **76**, 2877-2879 (2000).

239. P. Chen, X. Wu, J. Lin & K. L. Tan, "High H-2 uptake by alkali-doped carbon nanotubes under ambient pressure and moderate temperatures." *Science* **285**, 91-93 (1999).

240. G. Stan & M. W. Cole, "Hydrogen adsorption in nanotubes." *Journal of Low Temperature Physics* **110**, 539-544 (1998).

241. Y. Okamoto & Y. Miyamoto, "Ab initio investigation of physisorption of molecular hydrogen on planar and curved graphenes." *Journal of Physical Chemistry B* **105**, 3470-3474 (2001).

242. A. Andree, M. Le Lay, T. Zecho & J. Kupper, "Pair formation and clustering of D on the basal plane of graphite." *Chemical Physics Letters* **425**, 99-104 (2006).

243. L. Hornekær *et al.*, "Metastable structures and recombination pathways for atomic hydrogen on the graphite (0001) surface." *Physical Review Letters* **96**, (2006).

244. L. Hornekær *et al.*, "Clustering of chemisorbed H(D) atoms on the graphite (0001) surface due to preferential sticking." *Physical Review Letters* **97**, (2006).

245. D. W. Boukhvalov, M. I. Katsnelson & A. I. Lichtenstein, "Hydrogen on graphene: Electronic structure, total energy, structural distortions and magnetism from first-principles calculations." *Physical Review B* **77**, (2008).

246. E. J. Duplock, M. Scheffler & P. J. D. Lindan, "Hallmark of perfect graphene." *Physical Review Letters* **92**, (2004).

247. O. V. Yazyev & L. Helm, "Defect-induced magnetism in graphene." *Physical Review B* **75**, (2007).

248. P. Esquinazi *et al.*, "Induced magnetic ordering by proton irradiation in graphite." *Physical Review Letters* **91**, (2003).

249. E. Stolyarova *et al.*, "High-resolution scanning tunneling microscopy imaging of mesoscopic graphene sheets on an insulating surface." *Proceedings of the National Academy of Sciences of the United States of America* **104**, 9209-9212 (2007).

250. M. Ishigami, J. H. Chen, W. G. Cullen, M. S. Fuhrer & E. D. Williams, "Atomic structure of graphene on SiO_2." *Nano Letters* **7**, 1643-1648 (2007).

251. C. S. Chang, I. S. T. Tsong, Y. C. Wang & R. F. Davis, "Scanning Tunneling Microscopy and Spectroscopy of Cubic Beta-Sic(111) Surfaces." *Surface Science* **256**, 354-360 (1991).

252. B. C. Stipe, M. A. Rezaei & W. Ho, "Single-molecule vibrational spectroscopy and microscopy." *Science* **280**, 1732-1735 (1998).

253. A. J. Heinrich, J. A. Gupta, C. P. Lutz & D. M. Eigler, "Single-atom spin-flip spectroscopy." *Science* **306**, 466-469 (2004).

254. Y. B. Zhang *et al.*, "Giant phonon-induced conductance in scanning tunnelling spectroscopy of gate-tunable graphene." *Nature Physics* **4**, 627-630 (2008).

255. D. Tomanek *et al.*, "Theory and Observation of Highly Asymmetric Atomic-Structure in Scanning-Tunneling-Microscopy Images of Graphite." *Physical Review B* **35**, 7790-7793 (1987).

256. P. M. Ostrovsky, I. V. Gornyi & A. D. Mirlin, "Theory of anomalous quantum Hall effects in graphene." *Physical Review B* **77**, (2008).

257. V. M. Pereira, F. Guinea, J. M. B. Lopes dos Santos, N. M. R. Peres & A. H. Castro Neto, "Disorder Induced Localized States in Graphene." *Physical Review Letters* **96**, 36801 (2006).

258. T. O. Wehling *et al.*, "Local electronic signatures of impurity states in graphene." *Physical Review B* **75**, (2007).

259. H. A. Mizes & J. S. Foster, "Long-Range Electronic Perturbations Caused by Defects Using Scanning Tunneling Microscopy." *Science* **244**, 559-562 (1989).

260. K. F. Kelly & N. J. Halas, "Determination of alpha and beta site defects on graphite using C60 adsorbed STM tips." *Surface Science* **416**, L1085 (1998).

261. P. Ruffieux, O. Gröning, P. Schwaller, L. Schlapbach & P. Gröning, "Hydrogen Atoms Cause Long-Range Electronic Effects on Graphite." *Physical Review Letters* **84**, 4910 (2000).

262. H. Amara, S. Latil, V. Meunier, P. Lambin & J. C. Charlier, "Scanning tunneling microscopy fingerprints of point defects in graphene: A theoretical prediction." *Physical Review B* **76**, (2007).

263. V. Meunier & P. Lambin, "Scanning tunnelling microscopy of carbon nanotubes." *Philosophical Transactions of the Royal Society of London Series A-Mathematical Physical and Engineering Sciences* **362**, 2187-2203 (2004).

264. M. T. Lusk & L. D. Carr, "Nanoengineering defect structures on graphene." *Physical Review Letters* **100**, (2008).

265. B. An, S. Fukuyama & K. Yokogawa, "Graphitization of 6H-SiC(000(1)over-bar) surface by scanning tunneling microscopy." *Japanese Journal of Applied Physics Part 1-Regular Papers Short Notes & Review Papers* **41**, 4890-4893 (2002).

266. Serway, R. *Physics for Scientists and Engineers with Modern Physics*. Saunders College Publishing, Philadelphia (1990).

267. Datta, S. *Electronic Transport in Mesoscopic Systems*. Cambridge University Press, Cambridge UK (1995).

268. Y. Imry & Z. Ovadyahu, "Density-of-States Anomalies in a Disordered Conductor: A Tunneling Study." *Physical Review Letters* **49**, 841 (1982).

VITA

GREGORY M. RUTTER

Gregory Michael Rutter was born on August 29th 1981 in Garden Prairie, IL, located 90 miles west of Chicago. After graduation from high school in 1999, Gregory was admitted into Bradley University, located in Peoria, IL. Bradley provided him with a gateway for acquiring a broad spectrum of general knowledge, as well as physics education. In 2003, Gregory received his Bachelors of Science from the Physics Department with a minor in Mathematics, graduating summa cum lade. During the last few years of his undergraduate degree, he was able to participate in research supervised by Dr. Kevin Kimberlin. This opportunity provided him the motivation to continue his physics education in graduate school. In the fall of 2003, Gregory enrolled in the School of Physics graduate program at the Georgia Institute of Technology in Atlanta, GA. After passing the Ph.D. qualifying exam in the fall of 2004, he began his thesis research on epitaxial graphene in the group of Dr. Phillip N. First.

In the summer of 2006, Gregory had the unique opportunity to participate in cutting edge research at the National Institute of Standards and Technology (NIST) in Gaithersburg, MD; under the supervision of Dr. Joseph A. Stroscio. At NIST, he was able to use a one-of-a-kind low temperature scanning tunneling microscope. Using this instrument he was able to probe the structural and electronic properties of epitaxial graphene, and unearth some novel results. As for the future, Gregory has accepted an offer for a National Research Council post-doctorate fellowship to continue his graphene research for the next two years at NIST. In his postdoc tenure, he is interested in learning how to bridge the gap in understanding between macroscopic transport properties and microscopic STM measurements.